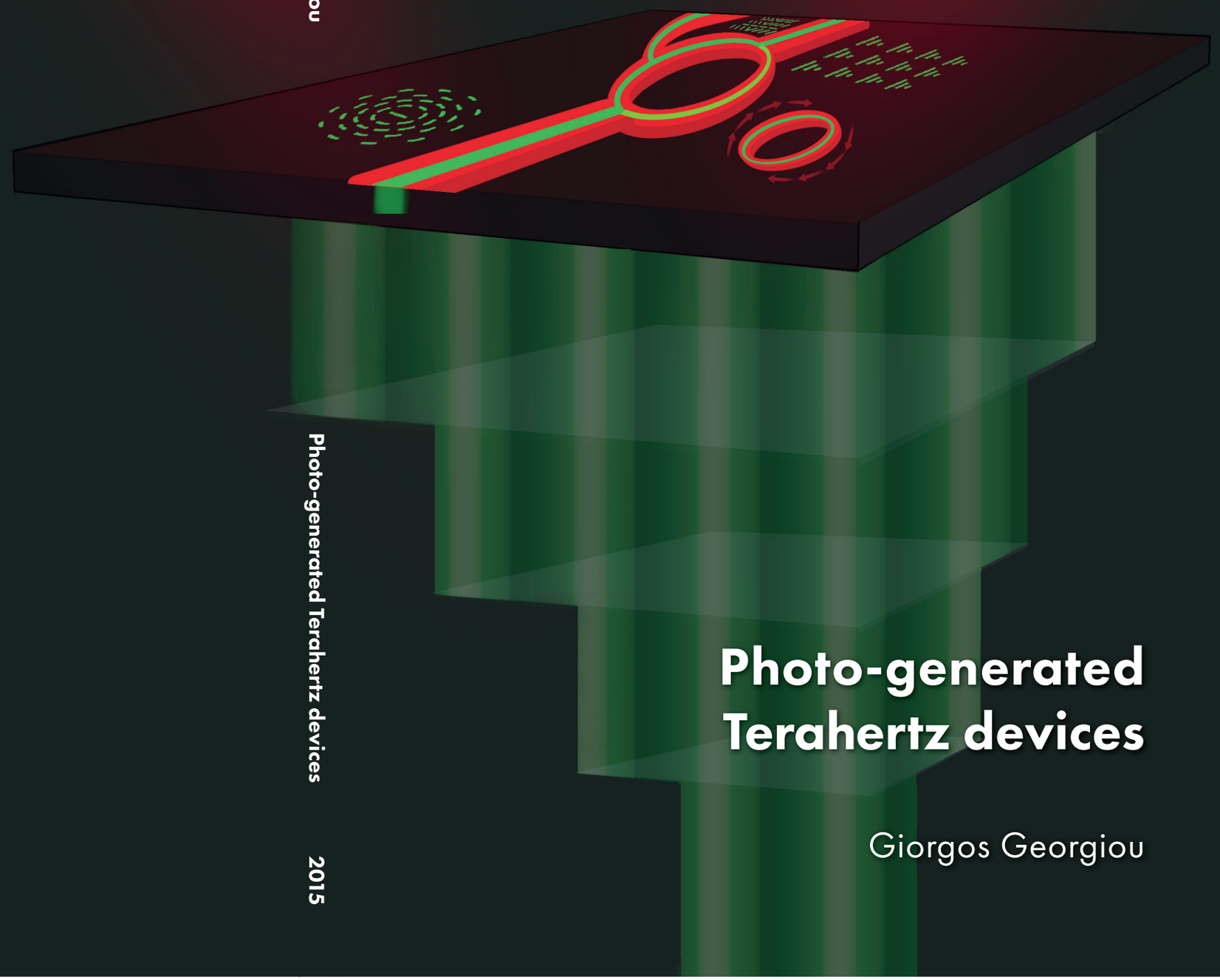

Photo-generated Terahertz devices

Giorgos Georgiou

Giorgos Georgiou

Photo-generated Terahertz devices

2015

ISBN 978-90-77209-98-1

Photo-generated Terahertz devices

Giorgos Georgiou

The cover shows an artist's impression of terahertz photo-generated devices on the surface of a semiconductor. Design by Iliana Boshoven-Gkini.

ISBN: 978-90-77209-98-1

Printed by GVO, Ede, Netherlands

The work described in this thesis is part of the research program of the "Stichting voor Fundamenteel Onderzoek der Materie (FOM)", which is financially supported by the "Nederlandse organisatie voor Wetenschappelijk Onderzoek (NWO)". This work is also funded by the "European Research Council" (ERC) through Grant No. 259727 THz-Plasmon.

This work was carried out at the Center for Nanophotonics, *FOM Institute for Atomic and Molecular Physics AMOLF*, Science Park 104, 1098 XG, Amsterdam, The Netherlands

A digital version of this thesis can be downloaded from http://www.amolf.nl
A catalogue record is available from the Eindhoven University of Technology Library.

Photo-generated terahertz devices

PROEFSCHRIFT

ter verkrijging van de graad van doctor aan de Technische Universiteit Eindhoven, op gezag van de rector magnificus, prof.dr.ir. F.P.T. Baaijens, voor een commissie aangewezen door het College voor Promoties, in het openbaar te verdedigen op dinsdag 02 februari 2016 om 14.00 uur

door

Georgios Georgiou

geboren te Nicosia, Cyprus

Dit proefschrift is goedgekeurd door de promotoren en de samenstelling van de promotiecommissie is als volgt:

voorzitter:	prof.dr. H.J.H. Clercx
1e promotor:	prof.dr. J. Gómez Rivas
2e promotor:	prof.dr. A. Fiore
leden:	prof.dr. J. Aizpurua (Universiteit of the Basque Country)
	prof.dr. P.C.M. Planken (Universiteit van Amsterdam)
	prof.dr. B. Koopmans
	prof.dr. T. Dekorsy (Universität Konstanz)
	dr. P. Zijlstra

Het onderzoek of ontwerp dat in dit proefschrift wordt beschreven is uitgevoerd in overeenstemming met de TU/e Gedragscode Wetenschapsbeoefening

Τί θα πει φως; Να κοιτάς με αθόλωτο μάτι όλα τα σκοτάδια.

Νίκος Καζαντζάκης

What is the real meaning of light? To gaze with undimmed eyes on all darkness.

Nikos Kazantzakis

Preface

The recent developments in the fields plasmonics and metamaterials have been accompanied by a variety of cornerstone results. Clocking, nano-imaging and manipulating light at the nanoscale are just few of the results arising from the interaction of light with plasmonic and metamaterial structures. These results have very promising potentials for fundamental research and applications that can lead to future devices, especially when these devices are operating at THz frequencies.

The following chapters constitute a part of the work done during a four year PhD research at the FOM Institute AMOLF in The Netherlands. In this work we have investigated theoretically and experimentally the photo-excitation of THz devices such as plasmonic and metamaterial structures, on the surface of semiconducting materials at THz frequencies. These structures range from simple dimer antennas and loaded antennas to blazed grating metasurfaces for beam steering. The advantage of the photo-generation technique presented in this thesis, is the simplicity of creating these structures, which does not require any cleanroom fabrication processes. The principle of this method is based on the active shaping of a laser beam through a spatial light modulator and the subsequent projection of this beam on the surface of a semiconductor. The projected beam, which contains an image with several structures, excites locally free carriers that render the semiconductor metallic while elsewhere the semiconductor behaves as a dielectric.

The integration of this technique with a THz time domain spectrometer (TDS) enables us to study the interaction of the projected plasmonic and metamaterial structures with THz waves in a non-invasive contact-less fashion. This is due to the unique characteristics of THz-TDS that allows the retrieval of not only the extinction (absorption and scattering) but also the extinction phase that provides useful information about the group velocity of the THz radiation travelling through the projected structures.

In addition, besides the novelty and the possibilities for applications of the technique presented in this thesis, we have made the first steps towards setting the physical foundations of photo-generated plasmonic and metamaterial structures. One of the main challenges that had to be addressed during this four year study was the dynamic nature of the system under investigation, which involved free carriers that were

locally excited in semiconductors, and a projection profile that had no fixed nor sharp boundaries. In order to address these challenges we have considered simple systems, such as dipole antennas, for which their physical properties are well understood in their fixed metallic analogues. The simple structures enabled the investigation of dynamic effects in semiconductors, such as diffusion and carrier recombination, the study of structures with graded boundaries as well as structures with graded refractive index. Although, all these effects have a great impact on the optical properties of plasmonic and metamaterial structures that deviates significantly from the conventional, they constitute a new and uncharted territory in the fields of plasmonics and metamaterials.

Giorgos Georgiou,
Amsterdam, October 2015

Contents

Preface **7**

Table of Contents **9**

1 Introduction **13**
1.1 The study of light and matter 13
1.2 Light, electricity and magnetism 14
1.3 Understanding and manipulating light 16
1.3.1 Optical properties of materials 18
1.3.2 Manipulating the optical properties of materials 18
1.4 The terahertz gap 20
1.5 Motivation and thesis outline 21
Bibliography 23

2 Terahertz spectroscopy for photonics **27**
2.1 Introduction 27
2.2 Optical-pump THz-probe spectrometer for THz photonics 31
2.2.1 Data acquisition 33
2.2.2 THz electric field 33
2.3 Data analysis 34
2.4 Sample fabrication and characterization 37
2.4.1 Optical characterization 38
2.4.2 Carrier Dynamics 39
2.5 Conclusions 41
Bibliography 42

3 Photo-generated surface plasmon polaritons at THz frequencies **47**
3.1 Introduction 48
3.2 Surface plasmon polaritons in semiconducting materials 49
3.3 Surface plasmon polaritons in doped semiconductors 51
3.4 Photo-generated surface plasmon polaritons 54
3.4.1 Optical excitation of free carriers 54
3.4.2 Photo-excited surface plasmons 55
3.4.3 Dynamics of photo-excited surface plasmons 58

3.5 Conclusions 62
Bibliography 64

4 Photo-generated THz antennas **69**
4.1 Introduction 69
4.2 Setup and sample description 70
4.3 Photo-generated THz antennas 71
4.4 Numerical simulations of photo-excited antennas 74
4.5 Conclusion 75
Bibliography 77

5 Active loaded plasmonic antennas at THz frequencies **81**
5.1 Introduction 81
5.2 Photo-excitation of active loaded antennas 83
5.3 Results 84
5.4 Conclusions 91
Bibliography 92

6 Terahertz wireless communications using photo-generated metasurfaces **97**
6.1 Broad-, broader-, broadest-band wireless communications 97
6.1.1 Terahertz wireless communications 99
6.1.2 Fundamental concepts 100
6.1.3 Terahertz transceivers with photo-generated metasurfaces . . . 101
6.2 Terahertz beaming 102
6.3 Experimental results 104
6.3.1 Photo-generated blazed gratings 104
6.3.2 THz diffraction measurements 105
6.4 Conclusions 108
Bibliography 109

Appendices **112**

A Calculation of TM modes for multilayered structures **113**

B Diffusion of free carriers in photo-excited semiconductors **115**
B.1 General solution of the diffusion equation with fixed boundaries 115
Bibliography 117

C Phase of travelling waves passing through absorbing interfaces **119**

Summary **121**

List of Publications **123**

Acknowledgements **125**

About the author **129**

1

Introduction

1.1 The study of light and matter

Since the ancient times light has been among humans a source of fear, curiosity and fascination; emotions strong yet so diverse. From the terrifying lightnings of Zeus, to the colorful rainbows of Iris and spectacular auroras of Eos, humans have respected the origin and nature of light, attributing it to the omniscience of gods. Over the centuries, humans have conquered their fear which was succeeded by an overwhelming curiosity about the origin and properties of light. Historical manuscripts from Aristophanes describe the use of light as a means for producing 'pure fire' through optical elements such as lenses and mirrors, while archeological evidence date these elements back to 6000 B.C.[1–3]. The efforts for understanding light were continued by the Greek philosophers, where first the Pythagoreans described vision as bouncing light rays from objects, but wrongly believed that the source of these rays was the human eye. One of the biggest developments in optics came during the 4th century B.C., where the philosophers Empedocles, Aristotle and Euclid set the foundations of geometric optics by describing the propagation of light rays in a straight line. A few centuries later, Claudius Ptolemy published one of the most influential manuscripts in the history of science that would later become a precursor of modern optics. Ptolemy extensively investigated the properties of light and more specifically he performed the first quantitative study on the refraction and color of light[4,5]. Although there was a vast amount of knowledge on optics since the 2nd-3rd century A.D. and despite the existing technology on making high quality optical components (i.e. lenses), the ancients did not know how to use them for scientific purposes and used them as baubles instead[6].

This changed during the European Renaissance period when ancient manuscripts dating back to the Hellenistic period (350 B.C. - 0 A.D.) were transferred from Costantinopolis to Europe and studied by the scholars. The ancient knowledge helped scholars such as De Dominis (1590) to understand the dispersion of light explaining therefore the formation of rainbows [6,7]. Moreover, due to the extensive knowledge found in the ancient manuscripts about the construction of lenses, the first optical instruments were made by Dutch scholars such as the telescope and the microscope around 1600. These optical instruments were among the earliest scientific equipment for systematically studying the interaction of light with matter, from the smallest possible scale to large and celestial scales.

For over 200 years (1600-1800) the study of light and matter resulted in a plethora of cornerstone discoveries in the field of optics. Amongst the most significant is the observation by Francesco Grimaldi (1665) that light rays can be diffracted by sharp edges or corners, an effect that was later investigated in great detail by Isaac Newton [8,9]. Ten years later, Christian Huygens in his nominal work entitled "*Traité de la Lumière*" (1678) introduced an alternative theory on the propagation of light, which successfully described many well known interactions of light with matter, such as reflection and refraction. In his theory, propagating light is described as a "wave" instead of a "ray", as it was initially described empirically in ancient manuscripts and supported theoretically by Fermat in 1662 [10,11]. The wave theory of light was to be criticized and rejected by many scholars (including I. Newton) as it was unable to describe the propagation of light in some materials, such as birefringent crystals. Huygen's theory on the wave nature of light was verified many years later (1801) by Thomas Young with his famous "*double slit*" experiment [12], while based on this theory Agustin Fresnel successfully explained light diffraction.

1.2 Light, electricity and magnetism

In the meantime, along with the experiments for understanding the nature of light, scientists and scholars were trying to set the foundations for electricity and magnetism. The first written documents reporting effects caused by electricity and magnetism date back to the 6th century B.C., where Thales of Miletus first observed that amber could lift straw and grass and also that lodestone can attract iron [13].

Perhaps the most important scientific instrument in the history of electricity and magnetism was the the compass. Although compass was invented in the ancient times by Chinese naturalists, it was not used for scientific purposes until the 13th century. The first documented use of the compass for experiments was by William Gilbert in his book "*De Magnete*" (1600), in which he writes that earth is a huge magnet and successfully explains how the compass works. In the year 1660, Otto von Guericke constructed the first machine for producing electric charges through friction and many years later (1729) Stephen Gray performed experiments on the transmission of electric charges through metallic rods (called electricity). A notable advancement in the history of electricity was the discovery of the Leyden jar by von Kleist in 1745 which was used

Box 1.1 ▶ Beyond red and blue

By the end of the 17th century it was well established among the scientific world that white light (sun–light) was composed out of the basic colors known to humans, namely colors ranging from blue to green and to red. In the year 1800 an influential experiment performed by William Herschel reported the observation of invisible light rays from the sun [14]. These rays were later named infrared light. Soon after, further experiments have showed the existence of light rays beyond the blue, named ultraviolet.

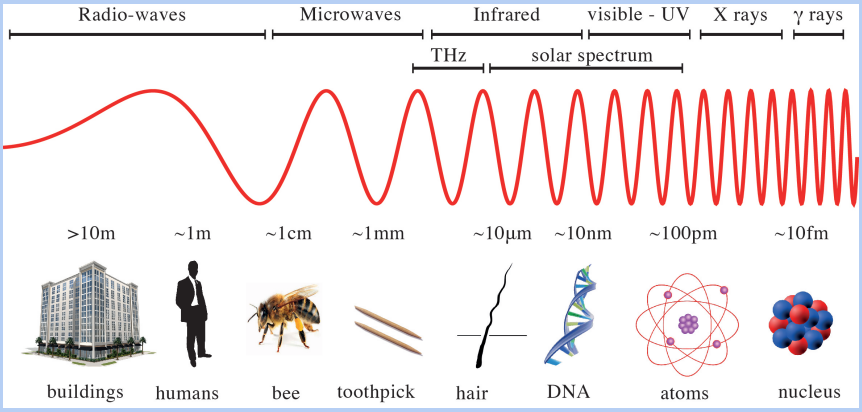

It is worthwhile to mention that visible light is a small fraction of the solar spectrum (sun–light). When Maxwell published his theory on electromagnetism (1854) scientists realized that solar spectrum was part of an even broader spectrum called "*electromagnetic spectrum*", as shown in the figure above. While testing the theory of Maxwell, Heinrich Hertz was the first to generate electromagnetic waves on purpose, beyond the solar spectrum (radio waves) [15].

for storing electric charges. Ten years later (1752), Benjamin Franklin succeeded in charging a Leyden jar by conducting electricity through a thunder and he therefore concluded that lightnings were electrical discharges that could also magnetize a metallic rod.

It was well established through experiments performed in 1734 by Du Fay that there were two types of electrical charges that could lead to attractive and repulsive forces. One of the most influential experiments in the history of electricity was conducted by Augustin de Coulomb who in the year 1784 managed to quantitatively measure the forces induced by the two types of charges. Coulomb's experiment was followed by an experiment that established for the first time a solid connection between electricity and magnetism. In 1820 Christian Oersted observed that the needle of a compass can be deflected by a wire carrying electric charges, while during the same year Arago and

Ampère discovered that a wire helix currying electricity could magnetize an iron bar.

By combining all the existing experimental knowledge, James Clerk Maxwell (1854) proposed a set of four equations that unified electricity and magnetism. With his theory, Maxwell suggested the existence of electromagnetic waves travelling at a constant speed, while he also predicted that light (optical waves) is nothing more than an electromagnetic wave. While Maxwell's theory was capable of explaining all the experimental results of electricity and magnetism, the theory was not accepted at first due to the lack of experimental evidence on the existence of the new type of waves[16]. The ingenuity and validity of Maxwell's theory was confirmed twenty years later (1887) by a young physicist named Heinrich Hertz. Hertz proved the hypothesis of Maxwell by designing a unique experiment in which electromagnetic waves generated by electric sparks could travel through free space and subsequently be detected by a metallic receiver, waves that were later named "*radio waves*" (see Box 1.1). In addition, based on the conjecture of Maxwell that light is an electromagnetic wave, Hertz proved that the waves generated by electric sparks can be reflected by metallic surfaces and diffracted in the same way light is[15].

One of the main features of Maxwell's theory is that similarly to water waves, electromagnetic waves travelling through free space can be described by their speed and wavelength λ, which is the distance between two maxima as it is illustrated in Box 1.2. The simplified schematic of the electromagnetic spectrum in Box 1.1 shows that the wavelength of electromagnetic waves can range between few kilometers (radio waves) to few femto-meters (gamma rays). As will be shown later in the thesis, the wavelength of the waves is a key characteristic that determines the interaction of electromagnetic waves with matter.

1.3 Understanding and manipulating light

Understanding the interaction of light with our surroundings is essential for explaining simple phenomena, like the green color of trees or the blue of the sky. Until the early 19th century the interaction of light with large objects, such as trees or animals, was well understood and connected with light rays reflected or absorbed by these objects. In particular when white light interacts with an object, the reflected light defines the color of the object while all the remaining colors are absorbed.

One of the greatest challenges for scientists was to explain the blue color of the sky. It was experimentally well established that the blue color was caused by small particles in the atmosphere but any theory based on the reflection of light rays by these particles could not be verified experimentally[17]. In 1871 Lord Rayleigh pointed out that the challenges in explaining this effect were due to the "*misuse of the word reflection*", since it is "*[...] associated with well known laws called after them*"[18], such as the laws of reflection and refraction. He also comments that the use of these laws are of "*no application unless the [...] body is larger than many square wavelengths*" (λ^2) and he supports his hypothesis by developing a wavelength dependant scattering theory which suggests that colors with short wavelength (blue) are scattered more efficiently

Box 1.2 ▶ Wavelength or Frequency?

In analogy with water waves, electromagnetic waves can be described by their speed and wavelength, λ. As it is demonstrated in the image below, the wavelength of a wave is the separation between two maxima.

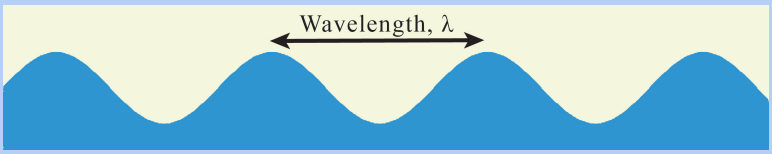

An equivalent way of describing a propagating wave is through its frequency ν and speed c, defined by the formula,

$$\nu = \frac{c}{\lambda}$$

where $c = 3 \cdot 10^8$ m/s is the speed of light in free space. Frequency is normally measured in Hertz (Hz), which is equal to an inverse of a second, i.e. 1 Hz = 1 s^{-1}. Throughout this thesis both definitions will be used.

than colors with long wavelength (red)[18]. This theory is later further supported by Maxwell's electromagnetic theory[19], while Gustav Mie developed a more general theory based on Maxwell's equations that describes also the interaction of light with larger particles, such as the water droplets in clouds[20]. Figure 1.1 shows a schematic which illustrates the effects of reflection, scattering and absorption.

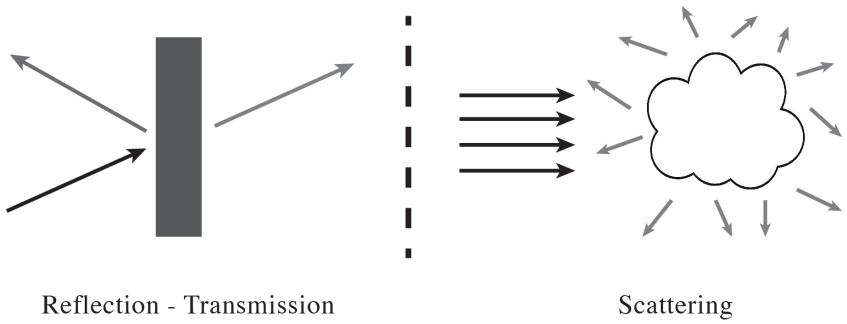

Figure 1.1: Illustration of reflection and transmission (left) and scattering (right)

As it was pointed out in Rayleigh's original paper[18], the interaction of light with matter strongly depends on the dimensions of the the scatterer (particle) compared to the wavelength of light. Therefore, it will be very informative to identify three regimes of interest, namely scattering of electromagnetic waves by particles with dimensions

much larger than the wavelength ($L >> \lambda$), much smaller ($L << \lambda$) and comparable to the wavelength ($L \sim \lambda$).

In modern optics the latter two regimes are of great importance for manipulating the properties of electromagnetic waves. Everyday examples from the two regimes include amongst others the use of nanoparticles that give certain color to paint ($L << \lambda$), or the use of telecommunication antennas to transmit and receive electromagnetic waves ($L \sim \lambda$).

1.3.1 Optical properties of materials

Besides the wavelength dependant interaction of light with matter a very important parameter that strongly affects the interaction is the type of material. In nature, the three most common types of materials are materials that can conduct electricity (metals), materials that do not conduct electricity (dielectrics) and materials that under certain conditions can conduct electricity (semiconductors).

The properties of the materials above and their interaction with electromagnetic waves can be summarized in two basic quantities that form the optical properties of the material, namely the electric permittivity $\tilde{\epsilon}$, and the magnetic permeability $\tilde{\mu}$. The electric permittivity $\tilde{\epsilon}$ describes the electric properties of the material, i.e. negative permittivities correspond to metals and positive permittivities correspond to dielectrics, while the permittivity of semiconductors can vary from positive to negative and vice versa. The magnetic permeability $\tilde{\mu}$ describes the magnetic properties of a material[21]. As will be elucidated in the next chapters, the optical properties of a scatterer do not only depend on the type of material that is made out of, but it also depends on the shape as well as the dimensions. Thus, by properly manipulating the shape and dimensions it is possible to engineer artificial materials that cannot be found in nature.

Over the last century and especially after the 2nd World War, a lot of attention was given for investigating the interaction between electromagnetic waves and metallic elements. The purpose of these studies was mainly the development of antennas that transmit and receive electromagnetic signals, for telecommunications, military applications, radio-astronomy and many others. These antennas were linear metallic elements or a combination of linear elements that are typically few centimetres to few meters long. The operation principle of these antennas is based on the half wavelength ($\lambda/2$) resonance, which implies that the interaction of these antennas with electromagnetic waves is maximized when the total length of the antenna is equal with half the wavelength of the wave ($L \sim \lambda/2$)[22].

1.3.2 Manipulating the optical properties of materials

As it was pointed out earlier, the shape of metallic structures will significantly influence the scattering of a wave. Electromagnetic waves interacting with structures of a certain shape (e.g. rings) can induce electric and magnetic phenomena in that structure, affecting the scattering of the wave. Furthermore, by combining several of

Box 1.3 ▶ Surface plasmon polaritons (SPPs)

The interaction of metallic surfaces with electromagnetic waves depends strongly on the density of free electrons in the metal. In particular at a metal–dielectric interface, under certain conditions that will be discussed in Chapter 3, the electromagnetic waves can be coupled to the free electrons and form coherent oscillations called surface plasmon polaritons. In the figure below the blue circles indicate large density of electrons, while the red circles indicate a small density of electrons. SPPs are electromagnetic waves polarized in the transverse direction that propagate along the metal–dielectric interface (x-direction).

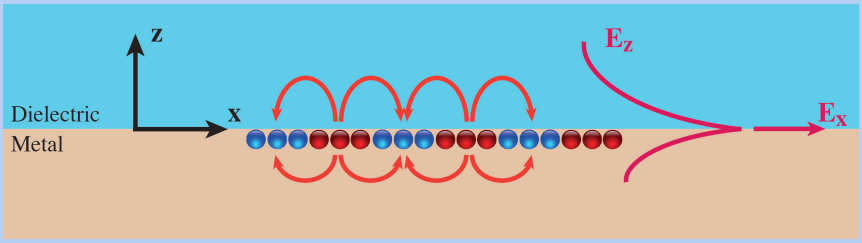

As it is indicated by the red lines that describe the electromagnetic waves along the direction perpendicular to the interface (z-direction), the electric field of SSPs E_z decays exponentially from the interface which causes the waves to be confined only at the interface. Due to their high confinement, SPPs can be used in many applications, such as light concentration in sub-wavelength volumes, perfect imaging, opto-electronics etc.

these structures together it is possible to modify the optical properties of a material, and therefore design a material which cannot be naturally found. These types of artificial materials, called "metamaterials", have received a lot of attention over the last ten years, since they provide the platform for applications such as cloaking, superlensing*, filtering and many others [23–30].

With the latest developments in the fields of nanotechnology smaller antenna and metamaterial designs could be realized. These designs have sizes typically in the range between few tens of micrometers (size of human hair) to few nanometers (size of human DNA). By reducing the dimensions of resonant structures, such as antennas, the operation wavelength is also reduced, thus providing access to the more elusive regions of the electromagnetic spectrum, namely the infrared and visible (see Box 1.1).

The studies at the infrared and visible part of the electromagnetic spectrum have been greatly influenced by the advances at radio-frequencies. Unfortunately, translating the fundamental concepts from one region of the spectrum to the other proved to be

*Imaging with very high resolution

far from easy. One of the main reasons is the excitation of surface plasmon polaritons at the interface between metals and dielectrics (see Box 1.3); effects that have not been previously observed at radio-frequencies*.

Surface plasmon polaritons (SPPs), which are among the main subjects of this thesis, can give rise to a plethora of interesting effects, such as enhanced absorption and scattering as well as the confinement of electromagnetic waves in volumes much smaller than the wavelength of the waves. Since the waves are concentrated in small volumes their intensity is greatly increased, therefore rendering structures that support SPPs to be excellent candidates for spectroscopy [32,33], non-linear optics [34] biosensing [35], solid state lighting [36] and photo-thermal cancer therapy [37,38].

1.4 The terahertz gap

A very important region of the electromagnetic spectrum from both scientific and technological point of view is the terahertz (THz, Box 1.1). For many years this part of the spectrum has been considered by many as a "spectroscopic gap", since as will be described in Chapter 2, the generation and detection of THz radiation has been challenging.

The THz part of the spectrum bridges two significant spectroscopic regions, namely the microwaves on the long wavelength side and the infrared on the short wavelength wide. Terahertz waves have wavelengths ranging from 3 mm to 30 μm that correspond to frequencies between 0.1 GHz to 10 THz (see Box. 1.1).

Over the last decades this part of the spectrum has gained an increasing popularity because many physical processes in various materials have a distinct "signature" response at these frequencies. Terahertz radiation can be therefore used for observing how various molecules rotate and vibrate as well as the formation of quasiparticles such as the Cooper pair which is responsible for the effect of superconductivity†. From the technological perspective, THz radiation is already used for medical purposes, such as the imaging of tumorous tissues, security scanning at the airports, food quality controls and many others. Furthermore, as will be discussed in Chapter 6, THz waves are a very promising candidate for the new generation of wireless communications, enabling data transmission rates of more than $0.1 - 1$ Tbps [40].

It is therefore crucial to understand and maximize the interaction of THz waves with matter, and moreover to introduce novel and versatile techniques for actively controlling this interaction. Consequently, the objective of the present thesis is to investigate the interaction of THz waves with plasmonic and metamaterial structures and in particular methods for actively tuning this interaction.

*It is worthwhile to note that at radio-frequencies it is possible to engineer SPPs on metal dielectric interfaces, called spoof plasmons [31]

†In solid state physics a Cooper pair is a quasiparticle formed in certain metals which is composed out of two electrons bound together. Cooper pairs are responsible for the effect of superconductivity in which electrons can move in a metal without any resistance [39].

1.5 Motivation and thesis outline

The design of plasmonic and metamaterial structures has been dominated so far by the use of metallic elements. Metals are excellent materials for these structures, since they are easy to fabricate, however they are not versatile. One of the main drawbacks of metallic elements is that once they are fabricated their interaction with electromagnetic waves cannot be modified significantly. The fixed response of metallic structures with electromagnetic waves is a potential obstacle for using these structures in future plasmonic and metamaterial devices and it is therefore necessary to search for alternative materials.

Semiconducting materials can be an excellent candidate for the next generation of plasmonic and metamaterial devices. Their versatile nature can be exploited for the design of tuneable devices whose interaction with THz waves can be changed in a continuous way. One of the main characteristics of semiconductors is that under certain conditions they can behave as a metal or a dielectric. The optical properties of semiconductors can be tuned through various electrical, optical and thermal methods, as will be explained in Chapter 3.

A great emphasis has been given over the last five to ten years on studying and developing active plasmonic and metamaterial devices made out of both metals and semiconductors. The interaction of these hybrid devices with THz waves is tuned by electrically changing the properties of the semiconducting material surrounding the metallic elements. Although these studies have shown remarkable results, hybrid devices are not very versatile and can only be used for limited applications such as switching.

An alternative approach for actively controlling the interaction of THz waves with plasmonic and metamaterial devices is by optically imprinting these devices on semiconductors, using a Spatial Light Modulator (SLM). The principle of this method is similar to the projection of movies on a movie theatre screen, where the projector in our experiments is the SLM. By using a SLM, plasmonic and metamaterial devices with micrometer dimensions can be projected on the surface of a semiconductor. The light projected on the semiconductor will render locations that contain elements from the image metallic, while the rest will remain dielectric. The lifetime of the projected image on the semiconductor is between a billionth and a trillionth of a second ($10^{-9} - 10^{-12}$ sec), time that is faster than the time needed by a conventional home computer to add up two numbers (i.e. a computer with 3.0 GHz CPU). Thus changing the projected devices on the semiconductor, which will therefore change the interaction with THz waves at these time scales, can be advantageous for future applications.

In this dissertation we have studied the physical and technical foundations of optically photo-generating plasmonic and metamaterial THz devices on semiconducting substrates. Using a technique that has been developed during the PhD thesis we have studied both experimentally and theoretically the interaction of these photo-generated devices with THz waves. The photo-excited charges in the illuminated regions will locally render the behaviour of the semiconductor metallic allowing the THz waves to

interact with the free charges.

For the purposes of the research presented in this thesis we have designed and assembled a THz spectrometer (THz-TDS) that includes a SLM along with a projection lens system, which is used for optically projecting plasmonic and metamaterial devices on semiconductors. The details of the spectrometer, the projection system as well as information on data acquisition and data analysis are explained in detail in Chapter 2.

The behaviour of the devices projected on the semiconductor depends on the intensity of light used for the projection and also the internal carrier dynamics of the semiconductor. The intensity of the projected light provides an indication of the amount of photo-excited free charges, i.e. how metallic is the semiconductor, while the internal dynamics of the semiconductor dictate the motion and the lifetime of the free charges. All these effects are theoretically described in Chapter 3.

In Chapter 4 we used the technique described above to photo-generate micro-meter sized plasmonic antennas. This chapter demonstrates experimentally that it is possible to optically tune the interaction of THz waves with plasmonic antennas in a continuous way. Plasmonic antennas such as the ones studied in Chapter 4 can be used to transmit or receive THz waves that can be consequently localized in very small volumes, with dimensions 100-1000 times smaller than THz wavelengths.

An extension of the results introduced in Chapter 4 is presented in Chapter 5. In this chapter we experimentally investigate the interaction of THz waves with photo-excited plasmonic antennas that are loaded with micrometer sized elements that behave like capacitors and inductors. Our results suggest a coupling of the plasmonic antenna with the capacitor- and inductor-like load, which can be tuned by changing the design and therefore the properties of the capacitor and inductor. These elements are important for the design of opto-electronic circuits.

The potential applications of the research performed for the purposes of this thesis are discussed in Chapter 6. In that chapter we discuss the potential use of the techniques described above in the field of wireless communications. More precisely we discuss the possibilities of using THz waves for ultra high speed data transmission rates for in- and out-of-house operation. Although wireless communications (WLAN*) using THz waves can successfully reach data rates of up to $0.1-1$ Tbps, one of the main drawbacks of using THz waves for WLAN is that they are highly directional, which means that for successfully achieving high data rates both receiver and transmitter have to be in a "line-of-sight" without any obstacles in between. In Chapter 6 we propose the use of metasurfaces† that can be projected on the surface of a semiconductor and actively tune the directionality of THz waves, and diverting them from any obstacles.

*Wireless Local Area Network

†A metasurface is a collection of optically thin sub-wavelength scatterets that can modify the direction of electromagnetic waves.

Bibliography

[1] B. Laufer, *Optical Lenses: I. Burning-Lenses in China and India*, T'oung Pao **16**, 169 (1915).

[2] G. Sines and Y. A. Sakellarakis, *Lenses in Antiquity*, American Journal of Archaeology **91**, 191 (1987).

[3] J. M. Enoch, *History of Mirrors Dating Back 8000 Years*, Optometry & Vision Science **83**, 775 (2006).

[4] M. Smith, *Ptolemy's Theory of Visual Perception*, volume 86 of *Transactions of the American Philosophical Society*, American Philosophical Society, 1996.

[5] S. R. Wilk, *Claudius Ptolemy's Law of Refraction*, Optics & Photonics News **15**, 14 (2004).

[6] L. Russo, *The Forgotten Revolution*, Springer-Verlag Berlin Heidelberg, 2004.

[7] The work of De Dominis *'Tractatus de Radiis Visûs et Lucis'* is cited by Isaac Newton in his book *'Opticks'* published in 1704 (see Ref.[6] p. 345).

[8] The work of Francesco Maria Grimaldi on the diffraction of light as it is discribed in *'Physico-mathesis de lumine (1665)'* is cited and explained by Florian Cajori, see Ref.[9] p. 96.

[9] F. Cajori, *A History of Physics*, Macmillan, 1929.

[10] D. Lindberg, *Theories of vision from Al-kindi to Kepler*, University of Chicago Press, 1976.

[11] M. S. Mahoney, *The mathematical career of Pierre de Fermat, 1601-1665*, Princeton University Press, 1994.

[12] T. Young, *The Bakerian Lecture: On the Theory of Light and Colours*, Philosophical Transactions of the Royal Society of London **92**, 12 (1802).

[13] H. W. Meyer and B. Dibner, *A history of electricity and magnetism*, MIT Press Cambridge, Mass., 1971.

[14] W. Herschel, *Experiments on the Refrangibility of the Invisible Rays of the Sun*, Philosophical Transactions of the Royal Society of London **90**, 284 (1800).

[15] D. Baird, R. Hughes, and A. Nordmann, editors, *Heinrich Hertz: Classical Physicist, Modern Philosopher*, volume 198 of *Boston Studies in the Philosophy and History of Science*, Springer, 1 edition, 1998.

[16] M. Born and E. Wolf, *Principles of optics: electromagnetic theory of propagation, interference and diffraction of light*, Cambridge university press, 1999.

[17] A. T. Young, *Rayleigh scattering.*, Physics Today **35**, 42 (1982).

[18] J. Strutt, *On the light from the sky, its polarization and colour*, Philosophical Magazine Series 4 **41**, 107 (1871).

[19] L. Rayleigh, *On the electromagnetic theory of light*, Philosophical Magazine Series 5 **12**, 81 (1881).

[20] G. Mie, *Beiträge zur Optik trüber Medien, speziell kolloidaler Metallösungen*, Annalen der Physik **330**, 377 (1908), "Contributions to the optics of turbid media, particularly of colloidal metal solutions", Transl. into English (1976).

[21] J. D. Jackson, *Classical electrodynamics*, Wiley, 3rd edition, 1998.

[22] C. A. Balanis, *Antenna Theory: Analysis and Design*, Wiley, 3 edition, 2005.

[23] J. B. Pendry, *Negative Refraction Makes a Perfect Lens*, Phys. Rev. Lett. **85**, 3966 (2000).

[24] S. Linden, C. Enkrich, M. Wegener, J. Zhou, T. Koschny, and C. M. Soukoulis, *Magnetic Response of Metamaterials at 100 Terahertz*, Science **306**, 1351 (2004).

[25] D. R. Smith, J. B. Pendry, and M. C. K. Wiltshire, *Metamaterials and Negative Refractive Index*, Science **305**, 788 (2004).

[26] T. J. Yen, W. J. Padilla, N. Fang, D. C. Vier, D. R. Smith, J. B. Pendry, D. N. Basov, and X. Zhang, *Terahertz Magnetic Response from Artificial Materials*, Science **303**, 1494 (2004).

[27] N. Fang, H. Lee, C. Sun, and X. Zhang, *Sub-Diffraction-Limited Optical Imaging with a Silver Superlens*, Science **308**, 534 (2005).

[28] D. Schurig, J. J. Mock, B. J. Justice, S. A. Cummer, J. B. Pendry, A. F. Starr, and D. R. Smith, *Metamaterial Electromagnetic Cloak at Microwave Frequencies*, Science **314**, 977 (2006).

[29] V. M. Shalaev, *Optical negative-index metamaterials*, Nat Photon **1**, 41 (2007).

[30] W. Cai, U. K. Chettiar, A. V. Kildishev, and V. M. Shalaev, *Optical cloaking with metamaterials*, Nat Photon **1**, 224 (2007).

[31] J. B. Pendry, L. Martín-Moreno, and F. J. Garcia-Vidal, *Mimicking Surface Plasmons with Structured Surfaces*, Science **305**, 847 (2004).

[32] M. Moskovits, *Surface-enhanced Raman spectroscopy: a brief retrospective*, Journal of Raman Spectroscopy **36**, 485 (2005).

[33] P. L. Stiles, J. A. Dieringer, N. C. Shah, and R. P. V. Duyne, *Surface-Enhanced Raman Spectroscopy*, Annual Review of Analytical Chemistry **1**, 601 (2008).

[34] M. Kauranen and A. V. Zayats, *Nonlinear plasmonics*, Nat Photon **6**, 737 (2012).

[35] K. A. Willets and R. P. V. Duyne, *Localized Surface Plasmon Resonance Spectroscopy and Sensing*, Annual Review of Physical Chemistry **58**, 267 (2007).

[36] G. Lozano, D. J. Louwers, S. R. Rodriguez, S. Murai, O. T. Jansen, M. A. Verschuuren, and J. Gómez Rivas, *Plasmonics for solid-state lighting: enhanced excitation and directional emission of highly efficient light sources*, Light Sci Appl **2**, e66 (2013).

[37] X. Huang, I. H. El-Sayed, W. Qian, and M. A. El-Sayed, *Cancer Cell Imaging and Photothermal Therapy in the Near-Infrared Region by Using Gold Nanorods*, Journal of the American Chemical Society **128**, 2115 (2006).

[38] A. Gobin, M. H. Lee, N. J. Halas, W. D. James, R. A. Drezek, and J. L. West, *Near-Infrared Resonant Nanoshells for Combined Optical Imaging and Photothermal Cancer Therapy*, Nano Letters **7**, 1929 (2007).

[39] N. Ashcroft and N. Mermin, *Solid State Physics*, Brooks/Cole, 1976.

[40] I. F. Akyildiz, J. M. Jornet, and C. Han, *Terahertz band: Next frontier for wireless communications*, Physical Communication **12**, 16 (2014).

2

Terahertz spectroscopy for photonics

Terahertz time domain spectroscopy is a powerful method for studying optically photo-excited plasmonic and metamaterial devices. In this chapter we present a brief historical introduction of far-infrared and THz spectroscopy with a particular focus on the generation and detection of THz radiation through non-linear methods, such as optical rectification and electro-optic sampling. In addition we explain in detail the projection technique used for the photo-excitation of plasmonic and metamaterial devices through a spatial light modulator (SLM), the methods for data analysis and sample characterisation.

2.1 Introduction

The great potential of photonic and opto-electronic devices operating at terahertz frequencies has boosted the quest for powerful, broadband and efficient THz sources as well as spectroscopy techniques [1]. These techniques are vital tools for studying the interaction of plasmonic and metamaterial components with THz electromagnetic waves. As it was pointed out in Chapter 1, until recently the THz gap of the electromagnetic

spectrum has remained unexplored mainly due to the challenges of generating and detecting THz radiation. Prior to the discussion of the experimental techniques used in this thesis, this chapter will present a short historical introduction of the far-infrared spectroscopy pointing out these challenges.

During the early days of far-infrared spectroscopy the main method used for studying the interaction of THz radiation with matter was the Fourier transform spectroscopy (THz-FTS), which involved an incoherent blackbody radiation source and a detector operating at cryogenic temperatures, such as Golay or bolometer detectors[2,3]. Even though this type of spectrometer has been the flagship of infrared spectroscopy since the early 50's, its use for far-infrared spectroscopy was limited due to the weak mercury arc lamp source and the relatively low sensitivity detectors[4].

With the discovery of the ruby laser in the early 60's and the observation of stimulated emission by molecular systems[5], more powerful coherent THz sources have been developed using electrically pumped water vapor molecules[6]. Furthermore, by the late 60's difference frequency mixing of two detuned ruby lasers has been used to generate tunable THz radiation in nonlinear crystals[7] and few years later a pulsed picosecond laser (Nd:glass) has been used to generate broadband THz radiation[8]. In addition to the new sources for far-infrared radiation, more sensitive solid state detectors have been realized, such as indium antimonide, germanium and silicon bolometers as well as the pyroelectric detectors that are still in use nowadays.

Far-infrared spectroscopy has received a lot of attention with the introduction of Hertzian dipoles activated by photoconductive Auston switches[9]. These switches are driven by subpicosecond laser pulses and have been used initially for microwave pulse generation[10,11]. The use of photoconductive switches was extended to the THz regime by Auston et al., where the techniques developed for microwaves were adopted for free space THz pulse generation and detection[12]. The popularity of THz spectroscopy has been increased due to the seminal work of Grischkowsky et al. in IBM labs, where high refractive index hemi-spherical elements were used for efficient outcoupling of THz radiation from the dipole emitter to free space and the consequent incoupling of the free space radiation to the dipole detector, reporting very high (10^4) signal-to-noise ratios[13–16].

The generation and detection of THz radiation using photoconductive dipoles has opened for the first time a unique window to the unexplored far-infrared regime of the electromagnetic spectrum. This is because the above techniques for generation and detection have many exceptional features such as the coherent and time gated spectroscopy with subpicosecond temporal resolution. The coherent THz generation in combination with the time gated THz detection renders far-infrared spectroscopy possible at room temperature as well as at high temperatures[17], since the detector is open for a very short time ($\sim$ 100 fs) and it is therefore immuned to the incoherent background THz radiation.

Even though the generation of THz radiation through optical rectification in electro-optic crystals was well known since the mid-60's[8,18–20], the interest of the scientific community was oriented mainly towards the photoconductive dipole antennas. Although photoconductive Hertzian dipoles can be used for broadband THz generation

and detection, the pulse width and therefore the frequency bandwidth is limited by the dynamics of the photoconductive material. The temporal response of such materials is typically in the subpicosecond time scale ($\sim$ 500 fs), which was comparable to the pulse width of Q-switched lasers used for THz generation in the early 80's. With the introduction of mode locked lasers and more specifically Ti:Sapphire laser in 1986 [21], broadband femtosecond pulses with higher peak intensities could be realized, and therefore a renewed interest on the generation and detection of THz radiation through nonlinear electro-optic crystals has emerged.

The generation and detection of coherent far-infrared radiation in electro-optic crystals was first demonstrated in $LiTaO_3$ using a focussed beam that was responsible for producing a pulsed Cherenkov cone of THz radiation, which was detected in the same crystal using a probe beam [22,23]. The THz radiation generated by the above method was confined inside the crystal due to total internal reflection, hence limiting its use for free space spectroscopy. The limitation has been overcome by an off-normal excitation of the crystal that allowed a part of the radiation to be extracted into free space and detected by a photoconductive switch [24]. Optical rectification in electro-optic crystals such as $LiNbO_3$ and $LiTaO_3$ has been used to efficiently generate THz radiation under normal incident excitation [25]. The studies for optical rectification in electro-optic crystals have been extended to organic materials that were proven to be more efficient THz emitters than their inorganic analogues [26].

Besides organic and inorganic electro-optic crystals, semiconductors can be used for THz generation through optical rectification. Semiconducting materials, such as LT-GaAs, have been used extensively in combination with Hertzian dipoles for the generation and detection of far-infrared radiation despite their bandwidth limitations due to the carrier dynamics. In the beginning of the 90's, studies in bulk InP have reported the generation of single cycle THz pulses with time width as short as 160 fs, results that came by surprise since the pulse width could not be justified by carrier acceleration in a static field [27,28]. These results were shortly after attributed to an interplay between carrier acceleration and optical rectification at the semiconductor surface [29], initiating therefore a study of THz generation through optical rectification in semiconductors [30,31].

Along with the advances for efficient THz sources similar efforts were made for better detectors. One of the most promising techniques for detection of THz radiation was the electro-optic sampling technique, which is based on the Pockel's effect. In this effect a static electric field can induce a change in the birefringence of an electro-optic crystal, technique that was initially used in the 80's for detecting electric signals in transmission lines [32,33]. This method was introduced in the mid-90's for the detection of free space THz radiation and it became immediately popular since in contrast to photoconductive switches, it has a flat spectral response for a broad range of frequencies and furthermore it overcomes significant limitations such as carrier lifetime [34–36].

Optical rectification and electro-optic sampling methods were used primarily in GaAs and ZnTe semiconductors, where a THz bandwidth of 3 THz and a signal to noise of 4000 has been initially reported [37,38]. These studies have been extended to a variety of semiconducting materials. Iit is worthwhile to mention that GaSe has been

Box 2.1 ▶ Optical rectification and Electro-optic sampling

The methods for THz generation and detection used throughout this thesis are summarised in the two figures below. For generating THz electromagnetic waves we used optical rectification, which is illustrated on the left side of the image. Optical rectification is a non-linear $\chi^{(2)}$ process in which the spectral components of a broadband femtosecond pulse are mixed in a non-linear medium, such as a ZnTe crystal, causing a DC polarisation. This beating polarisation is responsible for the emission of single cycle THz pulses with sub-picosecond time duration.

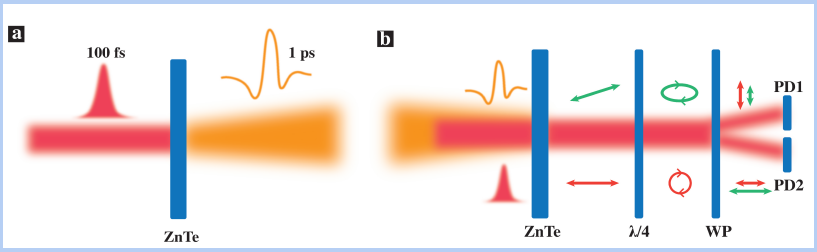

For the detection of THz electric fields we utilised the electro-optic sampling technique, shown on the right side of the figure above. For this detection method a linearly polarised femtosecond probe pulse (red beam), collinear with a linearly polarised THz pulse (orange beam) are mixed in a ZnTe crystal. In the absence of the THz pulse the polarisation of the probe pulse remains unchanged (red arrow). A quarter waveplate ($\lambda/4$) changes its polarisation from linear to circular, while a Wollaston prism separates the vertical and horizontal components of the circularly polarised probe beam. The two components are then directed in a balanced photodiode (BP1 and BP2) which detects the difference between the intensities of the vertical and horizontal polarisation components of the probe pulse. The difference in this case is equal to zero.
In the presence of the THz pulse the birefringence of the crystal is slightly modified, which results in a change in the polarisation of the probe pulse as indicated by the green arrow. The $\lambda/4$ waveplate will change the polarisation of the probe pulse from linear to elliptical and the Wollaston prism spatially separates the horizontal and vertical components of the elliptically polarised probe beam that are then directed in the balanced photodiode. The finite difference in intensities is proportional to the THz electric field.

also used for THz generation and detection resulting in bandwidths up to 41 THz, covering therefore frequencies from far- to mid-infrared [39–41].

This chapter will focus on the generation and detection methods of THz radiation through optical rectification and electro-optic sampling in ZnTe crystals respectively

(see Box 2.1). Furthermore, in this chapter we will introduce a technique in which a pump pulse is used along with the THz spectrometer for the photo-excitation of plasmonic and metamaterial devices on the surfaces of semiconductors. Subsequently, a discussion on the data acquisition and analysis will follow, with specific attention on the retrieval of the electric field amplitude and phase as well as the direct calculation from these quantities of the complex permittivity through a transfer matrix model. The above methods will be applied for a complete pump-probe characterization of a semiconducting sample, which in the case of the present thesis is a thin film of GaAs on a quartz substrate. This chapter will conclude with an overview of the methods used for THz generation and detection and the use of these techniques in the fields of photonics.

2.2 Optical-pump THz-probe spectrometer for THz photonics

The experiments for this thesis have been performed using a THz time domain spectrometer (TDS) that is combined with a pump beam for optical excitation of free carriers in semiconducting materials, commonly known as time-resolved THz-TDS. For this pump-probe technique a commercial amplified laser system has been utilised, namely the Legend Elite HE+ seeded with the Mantis Ti:Sapphire laser. The laser delivers 100 fs amplified pulses with wavelength $\lambda = 800$ nm and pulse energy 6 mJ at 1 KHz repetition rate, as shown in Fig. 2.1. These pulses are used for THz generation and detection as well as for band-to-band carrier excitation in the semiconducting sample. For the generation and detection of THz pulses we use 20% of the intensity (BS1). Out of this intensity 95% (BS2) is used for THz generation through optical rectification in a 0.5 mm ZnTe crystal, while the rest is used for electro-optical detection in a 1 mm ZnTe crystal as illustrated in Fig. 2.1. As it will be elucidated later in the chapter, by controlling the time delay between the beam that generates the THz radiation and the one used for the detection (DS2) we can reconstruct the THz electric field transients. Due to the high absorptance of THz radiation by water vapors in the atmosphere, the THz - TDS is enclosed in dry nitrogen environment shown by the black dashed lines in Fig. 2.1.

The remaining 80% of the initial beam intensity is used for photo-exciting free carriers in the semiconductor (pump beam). The pump beam after passing through the delay stage (DS2) it is directed towards a spatial light modulator (SLM).
The SLM is a key element in the setup shown in Fig. 2.1, which is a computer controlled liquid crystal device and it is used to spatially structure the pump beam. The pump beam is spatially shaped to contain several micrometer sized plasmonic and metamaterial devices. A horizontally polarized optical pulse ($\lambda = 800$ nm), indicated by the red beam in the figure, is transmitted through a polarizing beam splitter (PBS) and reflected back by the SLM. The SLM is a pixelated liquid crystal device (1920×1200 pixels), which rotates the polarization of the incident light. Light reflected from the so-called bright pixels undergoes a rotation of the polarization by

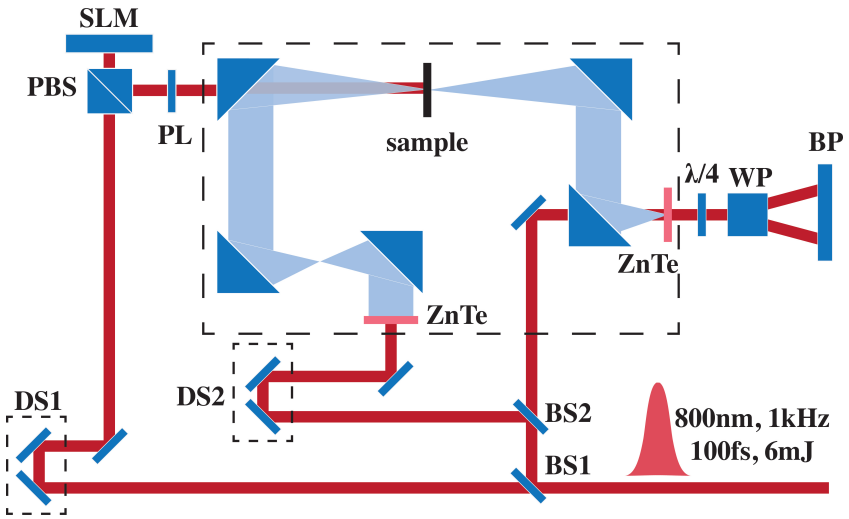

Figure 2.1: Schematic of a time-resolved THz time domain spectrometer powered by an amplified Ti:Sapphire laser. The main components used for the spectromenter are the following, DS: delay stage, BS: beam splitter, PBS: polarizing beam splitter, SLM: spatial light modulator, PL: projection lens, WP: wollaston prism and BP: balanced photodiode.

90^o, being therefore reflected by the PBS towards the sample; while light reflected from dark pixels maintains its polarization and it is transmitted through the PBS, thus not reaching the sample. The intensity of the light reflected by each pixel of the SLM and by the PBS can be varied continuously from a maximum value (bright pixel) to a minimum (dark pixel). The contrast between bright and dark states of the SLM is further improved by using additional polarizing optics (not shown in Fig. 2.1) and experimentally defined by illuminating a bulk GaAs sample and measuring the THz electric field transmitted through the sample. The obtained values for the THz electric field contrast were as high as $5 \cdot 10^4$.

A lens (PL) with a focal length of 150 mm is used to project (1:1) the structured beam onto the surface of the semiconducting sample, where electrons are photo-excited from the valence to the conduction band only at the illuminated regions. The pixel size on the surface of the sample is $8 \times 8\ \mu\text{m}^2$, being much smaller than the wavelength of THz radiation. Therefore, this technique is ideally suited for the optical photo-excitation of subwavelength plasmonic and metamaterial THz devices.

A THz probe pulse, indicated by the blue beam in Fig. 2.1, time delayed with respect to the optical pump beam excites the THz devices and propagates through the sample towards the electro-optic detector. The pump-probe time delay $\Delta\tau_{\text{p-p}}$ in our experiments is defined as the temporal separation between the optical pump pulse, which excites the free charge carriers and the THz probe pulse. With this definition a $\Delta\tau_{\text{p-p}} < 0$ indicates that the THz pulse propagates through the semiconductor before

the excitation of free carriers. On the other hand $\Delta\tau_{\mathrm{p-p}} > 0$ implies that the THz pulse propagates through the semiconductor after the free carriers have been excited by the pump pulse.
For most of the experiments in the present thesis a $\Delta\tau_{\mathrm{p-p}} = 5$ ps was chosen. As it is shown later in this chapter, this time delay is sufficiently short such that the spatial diffusion of the free carriers does not modify the dimensions of the photo-excited structures. It is also essential to mention that at this time scale we did not observe any ballistic electrons that could potentially modify the dimensions of the structures.

2.2.1 Data acquisition

The data acquisition for a typical time-resolved THz - TDS is based on the phase-demodulation technique using a lock-in amplifier. To modulate the signal reaching the balanced-photodiodes (see Fig. 2.1) we employ a mechanical chopper, which can be used in two configurations.

In the first configuration the chopper can be placed in the path of the beam that is used for THz generation and more specifically before the ZnTe crystal. By modulating the beam at half the repetition rate of the laser (i.e. 500 Hz) we can reconstruct the THz electric field as a function of time. If on the other hand the chopper is placed on the path of the beam used for the electro-optic sampling detection the THz electric field can also be reconstructed with the addition of a constant offset.

The second configuration is mainly used for data acquisition in pump-probe experiments. In these experiments the mechanical chopper is placed in the path of the pump beam, namely after the projection lens and before the sample (see Fig. 2.1). When the pump beam is modulated at half the repetition rate of the laser (i.e. 500 Hz) the detected signal will be the difference between the THz electric field transmitted through a pumped sample and the THz electric field transmitted through an unpumped sample, i.e.

$$\Delta E = E_{\mathrm{P}} - E_{\mathrm{NP}}, \tag{2.1}$$

where ΔE is the differential signal and E_{P}, E_{NP} are the THz electric fields transmitted through a pumped and an unpumped sample respectively. This detection method is more preferable than measuring the two electric fields separately using the first configuration, because lock-in amplifiers are more sensitive to small signals resulting therefore to larger signal-to-noise ratios.

2.2.2 THz electric field

By varying the time delay (DS2 in Fig. 2.1) between the beam that generates the THz radiation with respect to the beam that is used for electro-optic detection we can reconstruct the THz electric field transients. Figure 2.2(a) shows a typical THz electric field transient, with full width at half maximum (FWHM) approximately 700 fs. The spectrum of the sub-picosecond THz pulse is calculated by taking the

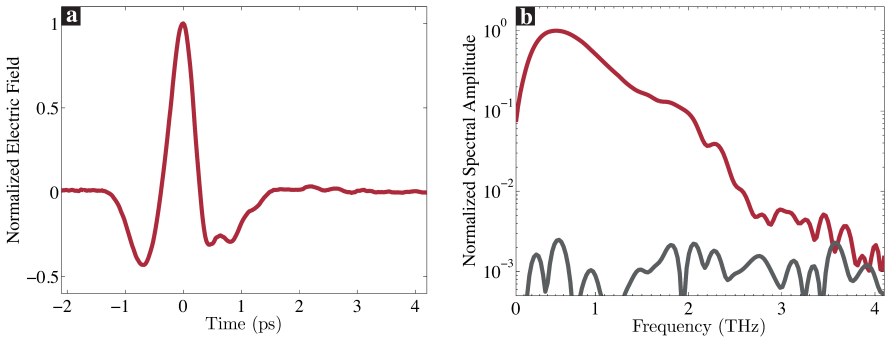

Figure 2.2: THz-TDS electric field transient (a) and THz electric field spectral amplitude (b). The grey dataset in (b) illustrates the noise level of the spectrometer, which results in signal-to-noise ratio of approximately 10^3.

Fourier transform of the THz electric field transient,

$$\tilde{E}(\nu) \equiv \mathcal{F}\{E(t)\} = \int E(t)\, e^{i2\pi\nu t}\, dt, \tag{2.2}$$

where $\tilde{E}(\nu)$ is the complex THz electric field spectrum and $E(t)$ is the THz electric field transient. The complex THz electric field spectrum contains information about both the electric field spectral amplitude and phase. Figure 2.2(b) shows the normalized electric field spectral amplitude ($|\tilde{E}(\nu)|$ red curve) and the noise level of the THz spectromenter (grey curve). The bandwidth of the spectrum spans for over an order of magnitude with a maximum of 10^3 signal-to-noise ratio at 0.5 THz. The phase of the complex electric field, $\mathrm{Arg}(\tilde{\mathrm{E}}(\nu))$, provides information about the delay of the THz pulse in a given medium.

2.3 Data analysis

In contrast to other ultrafast spectroscopy techniques, THz-TDS has the unique characteristic of generating and detecting electric field transients, instead of intensities. This feature can have significant advantages on the optical characterization of bulk samples and photonic structures, since the information retrieved from the spectrometer is both the electric field amplitude and phase as a function of frequency. These informations can be used for retrieving the optical properties of any sample directly from the measurements, such as the complex permittivity ($\tilde{\epsilon}$) and the complex permeability ($\tilde{\mu}$), without the use of the Kramers-Krönig relations that are employed in other types of spectroscopies.

To completely retrieve the complex electric and magnetic properties of a sample, two sets of measurements are required. The first is a reference measurement, in which the THz electric field is measured as it is reflected or transmitted through the sample's substrate (or free space), $E_{\mathrm{r,ref}}(t)$ and $E_{\mathrm{t,ref}}(t)$ respectively. The second is a reflection

and transmission measurement in the presence of the sample on the substrate, namely $E_{\mathrm{r}}(t)$ and $E_{\mathrm{t}}(t)$.
After normalizing the above electric fields to their references and taking the Fourier transform, the resulting complex electric field spectra will contain information about the reflected and transmitted amplitudes as well as the phases,

$$\tilde{r}(\nu) \equiv \frac{\tilde{E}_{\mathrm{r}}(\nu)}{\tilde{E}_{\mathrm{r,ref}}(\nu)} = |\tilde{r}(\nu)|\, e^{i\phi_{\mathrm{r}}(\nu)} \quad \text{and} \quad \tilde{t}(\nu) \equiv \frac{\tilde{E}_{\mathrm{t}}(\nu)}{\tilde{E}_{\mathrm{t,ref}}(\nu)} = |\tilde{t}(\nu)|\, e^{i\phi_{\mathrm{t}}(\nu)}, \tag{2.3}$$

where $\tilde{r}(\nu)$ and $\tilde{t}(\nu)$ is the complex reflection and transmission respectively.

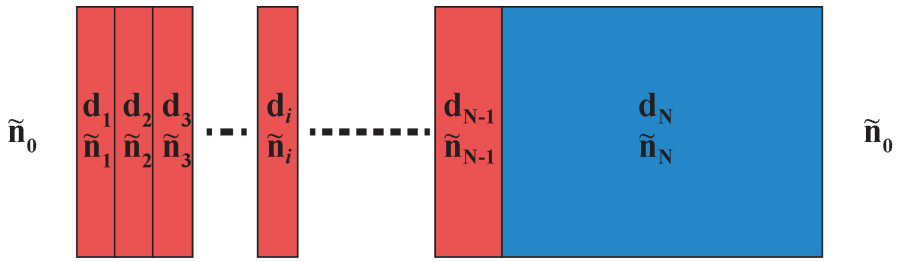

Figure 2.3: Illustration of the transfer matrix method.

In the most general case of a multilayered sample the reflected and transmitted electric fields can be described using the transfer matrix formalism [42]. Figure 2.3 shows a simplified schematic of the transfer matrix method, which consists out of N-layers with thickness d_m and complex refractive index $\tilde{n}_m = \sqrt{\tilde{\epsilon}_m \tilde{\mu}_m}$ surrounded by two semi-infinite spaces with refractive indices $\tilde{n}_0$ and $\tilde{n}_{\mathrm{N}+1}$ The electric field at each layer can be written as,

$$\tilde{E}_m(\nu) = A_m e^{-ik_m d_m} + B_m e^{ik_m d_m}, \tag{2.4}$$

where $k_m = \tilde{n}_m \frac{\omega}{c} \cos\theta_m$ is the in-plane component of the electric field wavevector, $\omega = 2\pi\nu$ is the angular frequency of the wave, θ_m is the angle of incidence and A_m, B_m are the amplitudes of the electric field at each interface. By properly matching the electric field amplitudes at the interfaces we can calculate the coefficients A_m and B_m (see Appendix A),

$$\begin{pmatrix} A_m \\ B_m \end{pmatrix} = P_m D_{m,q}^{-1} D_{m+1,q} \begin{pmatrix} A_{m+1} \\ B_{m+1} \end{pmatrix}, \tag{2.5}$$

where the index q specifies the type of the incident wave, i.e. s or p wave, while the $D_{m,q}$ and P_m are matrices given by,

$$D_{m,q=s} = \begin{pmatrix} 1 & 1 \\ \tilde{n}_m \cos\theta_m & -\tilde{n}_m \cos\theta_m \end{pmatrix}, \quad D_{m,q=p} = \begin{pmatrix} \cos\theta_m & \cos\theta_m \\ \tilde{n}_m & -\tilde{n}_m \end{pmatrix}, \tag{2.6}$$

and

$$P_m = \begin{pmatrix} e^{ik_m d_m} & 0 \\ 0 & e^{-ik_m d_m} \end{pmatrix}. \tag{2.7}$$

The D_m matrix represents the amplitude of the electric field inside any layer of the sample, while the matrix P_m is the phase accumulated by the electric field. The relation between all the electric field amplitudes are summarized in a matrix form,

$$\begin{pmatrix} A_0 \\ B_0 \end{pmatrix} = \begin{pmatrix} T_{11} & T_{12} \\ T_{21} & T_{22} \end{pmatrix} \begin{pmatrix} A_{N+1} \\ B_{N+1} \end{pmatrix}, \tag{2.8}$$

where T_{ij} is the transfer matrix given by,

$$\begin{pmatrix} T_{11} & T_{12} \\ T_{21} & T_{22} \end{pmatrix} = D_{1,q}^{-1} \left(\prod_{m=2}^{N-1} D_{m,q} P_m D_{m,q}^{-1} \right) D_{N,q}. \tag{2.9}$$

The complex reflection and transmission of the THz electric field through a multilayer sample can be calculated from the matrix components of Eq. 2.9 using the formulas,

$$\tilde{r} = \frac{T_{21}}{T_{11}} \quad \text{and} \quad \tilde{t} = \frac{1}{T_{11}}. \tag{2.10}$$

The complex electric and magnetic properties of a sample can be therefore retrieved by iterative algorithms using the data obtain from the transmission and reflection measurements (Eq. (2.3)) and the formulas obtained from the transfer matrix formalism (Eq. (2.10))[43].
While in the above description we have assumed for simplicity that the thickness of the sample is well defined, the exact value of the thickness is not required. By measuring longer electric field transients that include multiple fresnel reflections of the THz electric field inside the sample we can accurately determine the optical properties as well as the thickness of the sample using more advanced algorithms[44–46].

Although the transfer matrix method can provide the means for a complete characterization of a sample through reflection and transmission measurements of THz electric field transients, in the discussions through the entire thesis we will consider only transmission measurements using the setup shown in Fig. 2.1. The knowledge of only the transmitted electric fields will allow the extraction of either the electric permittivity ($\tilde{\epsilon}$) or the magnetic permeability ($\tilde{\mu}$), provided that one of them is well known. Since the THz devices presented in this thesis do not exhibit strong magnetic response we can assume that the magnetic permeability is constant, $\tilde{\mu} = 1$, and therefore we can solve the transfer matrix formula for retrieving the electric permittivity.

In the case of a sample that consists of a thin layer of material on a substrate (such as the one studied in this thesis), the wavelength is much longer than the thickness of the layer, $d \ll \lambda$. Therefore, the thin film approximation can be applied without any loss of generality. In this approximation the complex permittivity can be obtained from,

$$\tilde{t}(\nu) = \frac{\tilde{E}_{\mathrm{t}}(\nu)}{\tilde{E}_{\mathrm{sub}}(\nu)} \simeq \frac{1 + i\beta\sqrt{\tilde{\epsilon}}}{1 + i\beta \, \frac{(1-\sqrt{\tilde{\epsilon}})(\sqrt{\tilde{\epsilon}}-\sqrt{\tilde{\epsilon}_{\mathrm{sub}}})}{1+\sqrt{\tilde{\epsilon}_{\mathrm{sub}}}}}, \tag{2.11}$$

where $\beta = \omega d/c$, $\tilde{\epsilon}_{\text{sub}}$ is the complex permittivity of the substrate and $\tilde{\epsilon}$ is the complex permittivity of the thin film. The above equation can be solved analytically.

A very important consequence of the transfer matrix analysis is that its validity extends only for layers that are homogeneous, namely layers for which the permittivity ($\tilde{\epsilon}_m$) is spatially constant. For samples that contain layers of plasmonic and metamaterial structures the permittivity of these layers is not constant, but it spatially depends on the positions of the structures. This can lead to an invalid estimation of the optical properties of the structures since the detected THz electric field will contain information from both the structures and their surroundings. The non-homogeneous permittivity in such systems is a well known problem and it has been previously addressed in the framework of an effective medium theory for arrays of plasmonic and metamaterial structures[47]. The introduction of the effective medium theory for the characterization of such systems has accurately described the optical properties of samples that exhibit negative index of refraction.

The study of the optical properties of plasmonic and metamaterial structures in the effective medium theory framework falls outside the scope of the present thesis. Hence, in the next Chapters we will derive the optical properties of the sample under the assumption that the the permittivity of the layer containing the structures is homogeneous. Using this assumption, the resonant frequencies and linewidths of any resonant features present in the optical properties of the sample will be precise, whereas the absolute value might be over- or under-estimated.

2.4 Sample fabrication and characterization

Although the methods presented in this chapter are valid for any sample, this thesis will focus on the study of a thin film of GaAs on a substrate. As it will be elucidated in Chapter 3 GaAs is a very promising candidate for realizing plasmonic and metamaterial devices at THz frequencies, due to the high carrier mobility.

The sample was prepared in collaboration with the group of J. J. Schermer (Radboud University Nijmegen). An epitaxial growth was utilised in an Aixtron 200 low pressure metal organic chemical vapour deposition (MO-CVD) reactor and subsequent layer transfer. The epitaxial structure, composed of a 10 nm thick sacrificial AlAs layer followed by a 1 μm thick undoped GaAs layer, was grown at a temperature of 650 °C and a pressure of 20 mbar on a 2-inch diameter (001) GaAs wafer. After growth a flexible plastic support carrier was mounted on top of the GaAs epi-layer and the sample was subjected to a 20% HF solution in water for selective etching of the AlAs layer[48]. During the process the plastic carrier is used as a handle to bent away the GaAs epi-layer from the wafer ensuring optimal access of the HF solution to the 10 nm high etch front of the AlAs release layer[49]. After separation the GaAs thin-film is bonded to a 1 mm thick SiO_2 substrate using a mercapto-ester based polymer. The thickness of this bonding layer is approximately 40 μm. Finally the plastic support carrier is removed leaving the 1 μm single crystalline GaAs layer on a SiO_2 substrate.

2.4.1 Optical characterization

To experimentally determine the optical properties of the GaAs sample we perform pump-probe THz-TDS measurements. The analysis of the optically excited sample (pumped) is important for determining the amount of optically excited free carriers as well as their mobilities.

Before employing the transfer matrix method for the analysis of the pump-probe measurements (Eq. (2.10)), the optical properties of the substrate and the bonding polymer have to be experimentally determined. By measuring the transmitted field through the substrate and bonding layer respectively and by normalizing them to the free space THz electric field we can calculate the optical properties of both the materials, provided that the thickness of the two layers is precisely defined. The permittivities were to a first approximation frequency independent with values $\tilde{\epsilon}_{\mathrm{b}} = 2.6 + 0.12i$ and $\tilde{\epsilon}_{\mathrm{sub}} = 3.98 + 0.015i$ for the bonding layer and substrate, respectively. The experimentally obtained values for the substrate and bonding layer are used for determining the optical properties of the pumped GaAs.

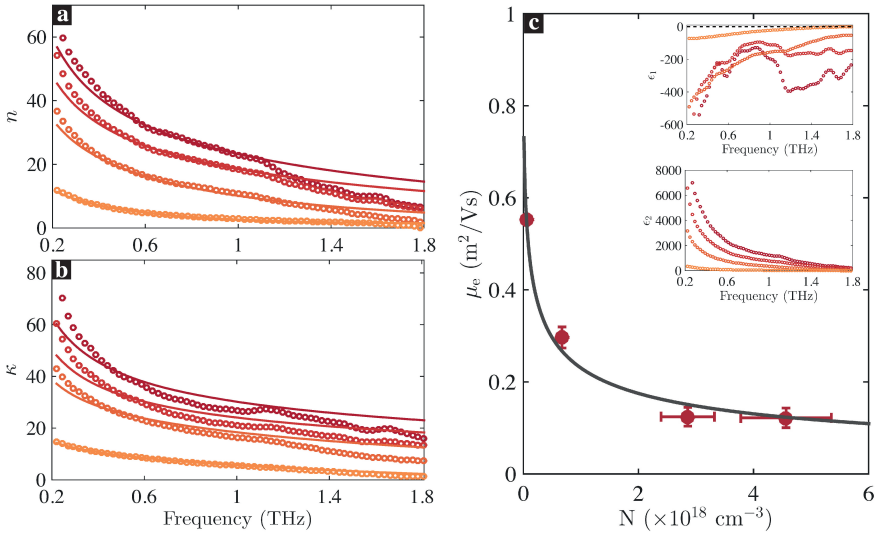

Figure 2.4: Optical-pump THz-probe characterization of GaAs (a) Real and (b) imaginary components of the refractive index, $\tilde{n} = \sqrt{\tilde{\epsilon}} = n + i\kappa$, for pump fluences 2, 20, 40 and 60 μJ/cm^2 from orange to red respectively. The cirles are the experimental data points and the solid lines are fits to the Drude model. (c) Mobility of free carriers for as a function of carrier density. The data points are the fitting parameters estimated from the Drude fits in (a) and (b) and the solid line is a fit to the emperical mobility equation (Eq. (2.13)). The insets of (c) shows the real (up) and imaginary (down) part of the permittivity.

In order to estimate the carrier mobility and density of free carriers in the photo-excited GaAs we use the Drude model. Drude model describes the microscopic transport properties of free electrons for a variety of materials (especially metals).

These properties are summarized in the macroscopic equation,

$$\tilde{n}^2 = \tilde{\epsilon} = \epsilon_\infty - \frac{\omega_\mathrm{p}^2}{\omega^2 + i\Gamma_\mathrm{e}\omega}, \tag{2.12}$$

where ϵ_∞, is the contribution of the ion background to the bulk permittivity. The second term of the equation describes the change of the bulk permittivity due to the presence of free electrons, where $\omega_\mathrm{p}^2 = Ne^2/\epsilon_0 m_\mathrm{eff}$ is the plasma frequency with N being the amount of free electrons per unit volume, ϵ_0 the permittivity of free space, m_eff the effective mass of electrons in the conduction band and $\Gamma_\mathrm{e} = e/\mu_\mathrm{e} m_\mathrm{eff}$ is the electron-electron scattering rate, which is inversely proportional to the effective mass (m_eff) and mobility (μ_e) of free electrons. For GaAs $\epsilon_\infty = 12.6$ and $m_\mathrm{eff} = 0.064$[50]. It is worthwhile to point out that although the Drude model describes very well the optical properties of many materials, as it will be discussed in Chapters 3 and 5 under certain resonant conditions the model needs to be properly modified[51,52].

Figure 2.4(a)-(b) illustrates the optical properties of the optically pumped ($\lambda_\mathrm{p} =$ 800 nm) GaAs for a number of fluences at pump-probe time $\Delta\tau_\mathrm{p-p} = 5$ ps. The circles illustrate the real and imaginary components of the refractive index, derived from the measurements and the transfer matrix equation (Eq. (2.10)), while the solid lines are fits to the Drude formula (Eq. (2.12)). The fitting parameters, carrier density (N) and mobility (μ_e), are shown in Fig. 2.4(c), where the error bars represent a 2σ confidence interval.

The data from Fig. 2.4(c) can be described by an empirical formula that relates the carrier mobility with the carrier concentration and it is valid for a number of semiconductors[53]. At room temperature the formula is,

$$\mu_\mathrm{e}(N) = \frac{\mu_1}{1 + (N \times 10^{-17})^\alpha}, \tag{2.13}$$

where μ_1 and α are free parameters that can be defined from the experimental data and 10^{-17} cm^{-3} is a normalization factor introduced to make the expression dimensionless. The solid dark line in Fig. 2.4(c) illustrates a non-linear fit to the mobility equation (Eq. (2.13)) with fitting parameters $\mu_1 = 0.96 \pm 0.19$ m^2/Vs and $\alpha = 0.50 \pm 0.18$. This result is in a good agreement with previous pump-probe studies in GaAs[50]. Although these studies report on the mobility of free electrons in bulk GaAs, we expect that deviations of the carrier mobility from the above formula in our photo-excited system are not significant for early pump-probe times ($\Delta\tau_\mathrm{p-p} = 5$ ps). On the contrary, at longer pump-probe times the mobility of free carriers will deviate from the values reported above when the carrier density is increased. As will be demonstrated later in this chapter the dynamics of the free carriers are non-linear due to impurities on the both the front and back surface of the thin film, which will therefore have an impact on the carrier mobility.

2.4.2 Carrier Dynamics

To study the carrier dynamics of the GaAs sample we perform pump-probe measurements by varying the pump delay stage (DS1 in Fig. 2.1) and keeping the

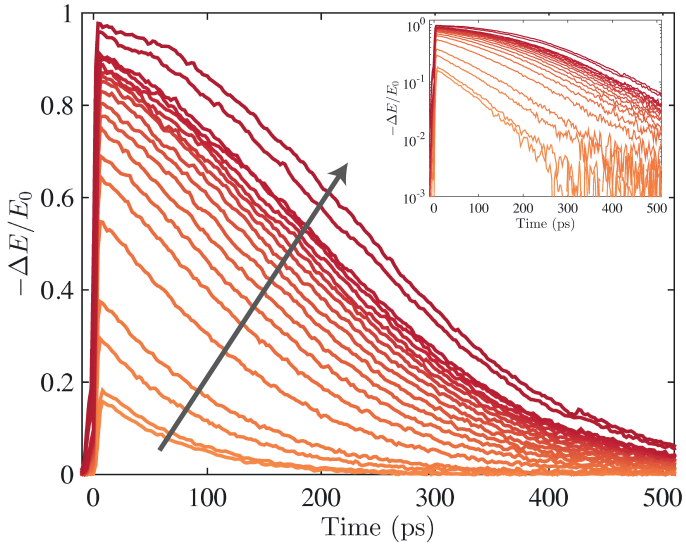

Figure 2.5: Carrier dynamics of GaAs for a number of pump fluences ranging from $0.125 - 70$ mW from orange to red respectively. The inset shows the data in a logarithmic scale for clarity.

THz delay stage at a fixed position, namely at the position of maximum signal (see $t = 0$ ps in Fig. 2.2(a)).
The pump-probe measurements are summarized in Fig. 2.5 where the dynamics of the GaAs are illustrated for a number of pump fluences from $0.25 - 140$ μJ/cm^{-2} from orange to red respectively, indicated also by the dark arrow The inset of the figure shows the carrier dynamics in a logarithmic scale for clarity. The ΔE E_0 is the differential signal (see Eq. (2.1)) normalized to the THz electric field transmitted through an unpumped sample. This quantity is proportional to the amount of photo-excited free carriers present in the semiconductor.

As it can be appreciated by the figure, for low pump fluences (orange) the dynamics of the free carriers exhibit a single exponential behaviour, whereas for larger pump fluences (red) the behaviour deviates from the single exponential especially at pump-probe times up to 150 ps. It is also evident from the dynamics that for low pump fluences the carriers tend to recombine much faster than for the higher fluences. The fast recombination of the free carriers can be attributed mainly to the ultrafast relaxation of the electrons into trap states below the conduction band, that are formed due to defects and impurities on both the surfaces of the semiconductor layer. The reduction of the carrier recombination rate for higher pump fluences suggests a saturation of the available trap states, since the photo-excited carrier density exceeds the density of the trap states[54]. When the carriers are trapped by the trap states the mobility of the electrons will be significantly influenced. The reported average carrier trapping time in GaAs samples, such as the one studied in this thesis, is approximately 10 ps

and therefore at earlier pump-probe times the mobility of the carriers will not deviate from the above empirical mobility equation (Eq. (2.13)).

2.5 Conclusions

In summary, this chapter introduces the time resolved THz-TDS technique and its great potential for THz photonics. More specifically, an extensive introduction was given on various far-infrared spectroscopy techniques with a particular attention to the THz-TDS. This technique can be complemented by a SLM that can be used to spatially shape the optical pump beam to contain several micrometer sized structures that can be optically projected on to the surface of a semiconductor.
In addition we have demonstrated the analysis techniques of the experimental data from a THz-TDS spectrometer giving emphasis on the retrieval of the complex optical properties of materials through the transfer matrix formulation. The sample fabrication and optical characterization is also discussed, in which we derive important quantities, such as the mobility and carrier concentration in the framework of the Drude model.

Bibliography

[1] M. Tonouchi, *Cutting-edge terahertz technology*, Nat Photon **1**, 97 (2007).

[2] P. R. Griffiths and J. A. De Haseth, *Fourier transform infrared spectrometry*, John Wiley & Sons, 2 edition, 2007.

[3] P. R. Griffiths and C. C. Homes, *Instrumentation for Far-Infrared Spectroscopy*, John Wiley & Sons, Ltd, 2006.

[4] P. L. Richards, *Bolometers for infrared and millimeter waves*, Journal of Applied Physics **76**, 1 (1994).

[5] L. E. S. Mathias and J. T. Parker, *STIMULATED EMISSION IN THE BAND SPECTRUM OF NITROGEN*, Applied Physics Letters **3**, 16 (1963).

[6] A. Crocker, H. A. Gebbie, M. F. Kimmitt, and L. E. S. Mathias, *Stimulated Emission in the Far Infra-red*, Nature **201**, 250 (1964).

[7] D. W. Faries, K. A. Gehring, P. L. Richards, and Y. R. Shen, *Tunable Far-Infrared Radiation Generated from the Difference Frequency between Two Ruby Lasers*, Phys. Rev. **180**, 363 (1969).

[8] K. H. Yang, P. L. Richards, and Y. R. Shen, *Generation of Far-Infrared Radiation by Picosecond Light Pulses in* $LiNbO_3$, Applied Physics Letters **19**, 320 (1971).

[9] D. H. Auston, *Picosecond optoelectronic switching and gating in silicon*, Applied Physics Letters **26**, 101 (1975).

[10] G. Mourou, C. V. Stancampiano, and D. Blumenthal, *Picosecond microwave pulse generation*, Applied Physics Letters **38**, 470 (1981).

[11] G. Mourou, C. V. Stancampiano, A. Antonetti, and A. Orszag, *Picosecond microwave pulses generated with a subpicosecond laser-driven semiconductor switch*, Applied Physics Letters **39**, 295 (1981).

[12] D. H. Auston, K. P. Cheung, and P. R. Smith, *Picosecond photoconducting Hertzian dipoles*, Applied Physics Letters **45**, 284 (1984).

[13] C. Fattinger and D. Grischkowsky, *Point source terahertz optics*, Applied Physics Letters **53**, 1480 (1988).

[14] C. Fattinger and D. Grischkowsky, *Terahertz beams*, Applied Physics Letters **54**, 490 (1989).

[15] M. van Exter, C. Fattinger, and D. Grischkowsky, *High-brightness terahertz beams characterized with an ultrafast detector*, Applied Physics Letters **55**, 337 (1989).

[16] M. van Exter and D. Grischkowsky, *Characterization of an optoelectronic terahertz beam system*, Microwave Theory and Techniques, IEEE Transactions on **38**, 1684 (1990).

[17] R. A. Cheville and D. Grischkowsky, *Far-infrared terahertz time-domain spectroscopy of flames*, Opt. Lett. **20**, 1646 (1995).

[18] M. Bass, P. A. Franken, J. F. Ward, and G. Weinreich, *Optical Rectification*, Phys. Rev. Lett. **9**, 446 (1962).

[19] D. H. Auston, A. M. Glass, and A. A. Ballman, *Optical Rectification by Impurities in Polar Crystals*, Phys. Rev. Lett. **28**, 897 (1972).

[20] Y. Shen, *Far-infrared generation by optical mixing*, Progress in Quantum Electronics **4**, 207 (1976).

[21] P. F. Moulton, *Spectroscopic and laser characteristics of* $\mathrm{Ti} : \mathrm{Al_2O_3}$, J. Opt. Soc. Am. B **3**, 125 (1986).

[22] D. H. Auston, *Subpicosecond electro-optic shock waves*, Applied Physics Letters **43**, 713 (1983).

[23] D. H. Auston, K. P. Cheung, J. A. Valdmanis, and D. A. Kleinman, *Cherenkov Radiation from Femtosecond Optical Pulses in Electro-Optic Media*, Phys. Rev. Lett. **53**, 1555 (1984).

[24] B. B. Hu, X. Zhang, D. H. Auston, and P. R. Smith, *Free-space radiation from electro-optic crystals*, Applied Physics Letters **56**, 506 (1990).

[25] L. Xu, X. Zhang, and D. H. Auston, *Terahertz beam generation by femtosecond optical pulses in electro-optic materials*, Applied Physics Letters **61**, 1784 (1992).

[26] X. Zhang, X. F. Ma, Y. Jin, T. Lu, E. P. Boden, P. D. Phelps, K. R. Stewart, and C. P. Yakymyshyn, *Terahertz optical rectification from a nonlinear organic crystal*, Applied Physics Letters **61**, 3080 (1992).

[27] X. Zhang, B. B. Hu, J. T. Darrow, and D. H. Auston, *Generation of femtosecond electromagnetic pulses from semiconductor surfaces*, Applied Physics Letters **56**, 1011 (1990).

[28] B. I. Greene, J. F. Federici, D. R. Dykaar, R. R. Jones, and P. H. Bucksbaum, *Interferometric characterization of 160 fs far-infrared light pulses*, Applied Physics Letters **59**, 893 (1991).

[29] S. L. Chuang, S. Schmitt-Rink, B. I. Greene, P. N. Saeta, and A. F. J. Levi, *Optical rectification at semiconductor surfaces*, Phys. Rev. Lett. **68**, 102 (1992).

[30] X. Zhang, Y. Jin, and X. F. Ma, *Coherent measurement of THz optical rectification from electro-optic crystals*, Applied Physics Letters **61**, 2764 (1992).

[31] A. Rice, Y. Jin, X. F. Ma, X.-C. Zhang, D. Bliss, J. Larkin, and M. Alexander, *Terahertz optical rectification from < 110 > zinc-blende crystals*, Applied Physics Letters **64**, 1324 (1994).

[32] J. A. Valdmanis, G. Mourou, and C. W. Gabel, *Picosecond electro-optic sampling system*, Applied Physics Letters **41**, 211 (1982).

[33] J. Valdmanis and G. Mourou, *Subpicosecond electrooptic sampling: Principles and applications*, Quantum Electronics, IEEE Journal of **22**, 69 (1986).

[34] Q. Wu and X. Zhang, *Free-space electro-optic sampling of terahertz beams*, Applied Physics Letters **67**, 3523 (1995).

[35] Q. Wu and X.-C. Zhang, *Ultrafast electro-optic field sensors*, Applied Physics Letters **68**, 1604 (1996).

[36] G. Gallot and D. Grischkowsky, *Electro-optic detection of terahertz radiation*, J. Opt. Soc. Am. B **16**, 1204 (1999).

[37] A. Nahata, A. S. Weling, and T. F. Heinz, *A wideband coherent terahertz spectroscopy system using optical rectification and electro-optic sampling*, Applied Physics Letters **69**, 2321 (1996).

[38] Q. Wu, M. Litz, and X. Zhang, *Broadband detection capability of ZnTe electro-optic field detectors*, Applied Physics Letters **68**, 2924 (1996).

[39] R. A. Kaindl, F. Eickemeyer, M. Woerner, and T. Elsaesser, *Broadband phase-matched difference frequency mixing of femtosecond pulses in GaSe: Experiment and theory*, Applied Physics Letters **75**, 1060 (1999).

[40] A. Leitenstorfer, S. Hunsche, J. Shah, M. C. Nuss, and W. H. Knox, *Detectors and sources for ultrabroadband electro-optic sampling: Experiment and theory*, Applied Physics Letters **74**, 1516 (1999).

[41] R. Huber, A. Brodschelm, F. Tauser, and A. Leitenstorfer, *Generation and field-resolved detection of femtosecond electromagnetic pulses tunable up to 41 THz*, Applied Physics Letters **76**, 3191 (2000).

[42] P. Yeh, *Optical Waves in Layered Media*, Wiley-Interscience, 2nd edition, 2005.

[43] L. Duvillaret, F. Garet, and J.-L. Coutaz, *A reliable method for extraction of material parameters in terahertz time-domain spectroscopy*, Selected Topics in Quantum Electronics, IEEE Journal of **2**, 739 (1996).

[44] L. Duvillaret, F. Garet, and J.-L. Coutaz, *Highly precise determination of optical constants and sample thickness in terahertz time-domain spectroscopy*, Appl. Opt. **38**, 409 (1999).

[45] T. D. Dorney, R. G. Baraniuk, and D. M. Mittleman, *Material parameter estimation with terahertz time-domain spectroscopy*, J. Opt. Soc. Am. A **18**, 1562 (2001).

[46] M. Scheller, *Data Extraction from Terahertz Time Domain Spectroscopy Measurements*, Journal of Infrared, Millimeter, and Terahertz Waves **35**, 638 (2014).

[47] D. R. Smith, D. C. Vier, T. Koschny, and C. M. Soukoulis, *Electromagnetic parameter retrieval from inhomogeneous metamaterials*, Phys. Rev. E **71**, 036617 (2005).

[48] M. M. A. J. Voncken, J. J. Schermer, A. T. J. van Niftrik, G. J. Bauhuis, P. Mulder, P. K. Larsen, T. P. J. Peters, B. de Bruin, A. Klaassen, and J. J. Kelly, *Etching AlAs with HF for Epitaxial Lift-Off Applications*, Journal of The Electrochemical Society **151**, G347 (2004).

[49] J. Schermer, G. Bauhuis, P. Mulder, E. Haverkamp, J. van Deelen, A. van Niftrik, and P. Larsen, *Photon confinement in high-efficiency, thin-film III–V solar cells obtained by epitaxial lift-off*, Thin Solid Films **511–512**, 645 (2006).

[50] S. Adachi, *Handbook on physical properties of semiconductors*, Springer US, 2004.

[51] R. Ulbricht, E. Hendry, J. Shan, T. F. Heinz, and M. Bonn, *Carrier dynamics in semiconductors studied with time-resolved terahertz spectroscopy*, Rev. Mod. Phys. **83**, 543 (2011).

[52] J. Lloyd-Hughes and T.-I. Jeon, *A Review of the Terahertz Conductivity of Bulk and Nano-Materials*, Journal of Infrared, Millimeter, and Terahertz Waves **33**, 871 (2012).

[53] C. Hilsum, *Simple empirical relationship between mobility and carrier concentration*, Electronics Letters **10**, 259 (1974).

[54] G. Segschneider, F. Jacob, T. Löffler, H. G. Roskos, S. Tautz, P. Kiesel, and G. Döhler, *Free-carrier dynamics in low-temperature-grown GaAs at high excitation densities investigated by time-domain terahertz spectroscopy*, Phys. Rev. B **65**, 125205 (2002).

3

Photo-generated surface plasmon polaritons at THz frequencies

We investigate theoretically the excitation and active control of the optical properties of surface plasmon polaritons on both doped and optically excited semiconductors at THz frequencies. In this work we discuss the use of semiconducting materials as an alternative to noble metals for plasmonics at THz frequencies and furthermore we suggest that due to their versatile nature they can be integrated more efficiently to the current semiconductor-based technology. This is supported by demonstrating that doped and optically excited semiconductors can support surface plasmon polaritons with optical properties that can be controlled in a continuous manner. Furthermore, we discuss the dynamics of surface plasmons influenced by the carrier diffusion and recombination mechanisms in the semiconductor. Finally, we suggest that based on the application, surface plasmon polaritons can be modulated or switched on time scales that range between few picoseconds to milliseconds.

3.1 Introduction

The integration of surface plasmon-based devices with the current semiconductor-based technology is predicted to be essential for future photonic and opto-electronic applications [1,2]. The principles of these devices are linked with the excitation of surface plasmon polaritons (SPPs), which are coherent oscillations of free charges coupled to propagating electromagnetic waves on the surface of a conducting material [3].

The physical properties, as well as the excitation mechanisms of SPPs, have been extensively studied for over a decade unveiling their unique characteristics. These include amongst others the confinement of light into subwavelength dimensions, which provides the opportunity of localizing and guiding electromagnetic waves at subwavelength scales [4]. Manipulating light at these scales has been the starting point of a fertile research with the objective of designing fast opto-electronic components and interconnects as well as the development of smart techniques that have revolutionized the fields of spectroscopy [5,6] and solid state lighting [7,8].

Inspired by the advances on reconfigurable photonic devices [9–12], a great emphasis has been given on studying and developing active plasmonic components. These components are composed out of metallic structures positioned on materials with optical properties that can be modified either thermally, electrically or optically. Studies have reported the use of semiconductors [13–16], organic molecules [17,18], quantum dots [19], as well as phase change materials [20–23] for optical switching and plasmon modulation.

While all of the above studies rely on changes of the refractive index in the surrounding medium recent works have shown active control of surface plasmons by changing the optical properties of the metallic elements. This has been achieved by perturbing the electron energy density of the metal by optical illumination (pump). As a consequence energy states above the Fermi level are filled whereas the states below the Fermi level become empty. This process results into a change of the optical properties of the metal on a femtosecond time scale, before the electrons return to their initial state due to electron cooling processes. Using this mechanism a femtosecond plasmon modulation has been shown in metallic gratings [24,25] and waveguides [26] as well as in optically excited gratings using interferometric techniques [27].

A more direct method for active surface plasmon switching and modulation has been experimentally shown using optically excited semiconducting structures at terahertz (THz) frequencies [28]. In these studies the switching properties rely on the material dynamics, whereas the modulation properties depend on the plasma frequency of the semiconductor which can be tuned by varying the amount of free electrons that are optically excited. By taking advantage of the versatile nature of optically excited semiconductors, our experiments (see Chapter 4) have reported photo-generated surface plasmons at THz frequencies based on a structured optical excitation of a flat semiconductor [29,30]. The active photo-excitation of surface plasmons on semiconducting surfaces will render the integration of plasmonic devices with the current semiconductor-based technology more accessible and versatile. Therefore, a more systematic study on the nature and the dynamics of photo-excited

plasmonic modes has to be carried out.

In this work we present theoretical calculations on photo-generated SPP modes on the surface of a semiconductor for various carrier concentrations and thicknesses. Various carrier densities were used to illustrate active control of SPP modes, while the two different thickness (1 μm and 350 μm) were used to illustrate the excitation of SPP modes in systems that can be experimentally realised [29–31]. In the system under investigation we consider a non-homogeneous carrier excitation due to the Beer-Lambert-like absorption of semiconductors. In addition we extend our results to include free carrier dynamics such as diffusion and recombination, effects that will dynamically change the properties of the SPP modes.

3.2 Surface plasmon polaritons in semiconducting materials

The simplest system that supports the excitation and propagation of SPPs is a metal - dielectric interface. In this simplified system the SPP wave can travel along the interface with a dispersion relation given by [3],

$$k_{\mathrm{spp}} = \frac{\omega}{c}\sqrt{\frac{\tilde{\epsilon}_{\mathrm{m}}\epsilon_{\mathrm{d}}}{\tilde{\epsilon}_{\mathrm{m}}+\epsilon_{\mathrm{d}}}}, \tag{3.1}$$

where ω is the angular frequency of the wave, c is the speed of light in vacuum, ϵ_{d} is the permittivity of the dielectric and $\tilde{\epsilon}_{\mathrm{m}} = \epsilon_1 + i\epsilon_2$ is the complex permittivity of the metal. Semiconductors can have either dielectric or metallic behaviour at certain frequencies depending on the amount free charges present in the conduction band. In addition to the Drude model introduced in Chapter 2 (Eq. (2.12)), the permittivity of semiconductors can be described by the Drude-Lorentz model, which takes into account contributions from the free electron "sea" as well as vibrations of the optical lattice (phonons),

$$\tilde{\epsilon}_{\mathrm{m}} = \epsilon_\infty - \frac{\omega_{\mathrm{p}}^2}{\omega^2 + i\Gamma_{\mathrm{e}}\omega} + \frac{\epsilon_\infty\left(\omega_{\mathrm{LO}}^2 - \omega_{\mathrm{TO}}^2\right)}{\omega_{\mathrm{TO}}^2 - \omega^2 + i\Gamma_{\mathrm{p}}\omega}, \tag{3.2}$$

The first term of the above equation, ϵ_∞, is the contribution of the ion background to the permittivity (bulk). The second term describes the change of the bulk permittivity due to the presence of free electrons where $\omega_{\mathrm{p}}^2 = Ne^2/\epsilon_0 m_{\mathrm{eff}}$ is the plasma frequency, with N being the amount of free electrons per unit volume, ϵ_0 the permittivity of free space, m_{eff} the effective mass of electrons in the conduction band and $\Gamma_{\mathrm{e}} = e/\mu_{\mathrm{e}} m_{\mathrm{eff}}$ is the electron-electron scattering rate, which is inversely proportional to the effective mass (m_{eff}) and mobility (μ_{e}) of free electrons. The last term of the equation depicts the contribution of lattice vibrations (phonons) to the permittivity, where ω_{LO} and ω_{TO} are the frequencies of longitudinal and transverse vibrations respectively and Γ_{p} is the damping coefficient of optical phonons.

The plasma frequency of semiconductors and therefore the permittivity can be changed in a continuous way using a variety of methods. These methods rely on the variation of the free electron density in the semiconductor by either thermally tuning the intrinsic carrier concentration ($N_\mathrm{i} \propto T^{3/2}$), or by introducing impurity atoms that can donate electrons or holes to the semiconductor (ion implantation), or by an above the bandgap optical excitation. Increasing the free electron density of a material can have significant implications on the carrier mobility (μ_e), which is considered to be an important material property for SPPs[32]. The mobility of carriers is closely related to the dissipative losses inside the material and therefore linked to critical surface plasmon properties such as propagation length and lifetime.

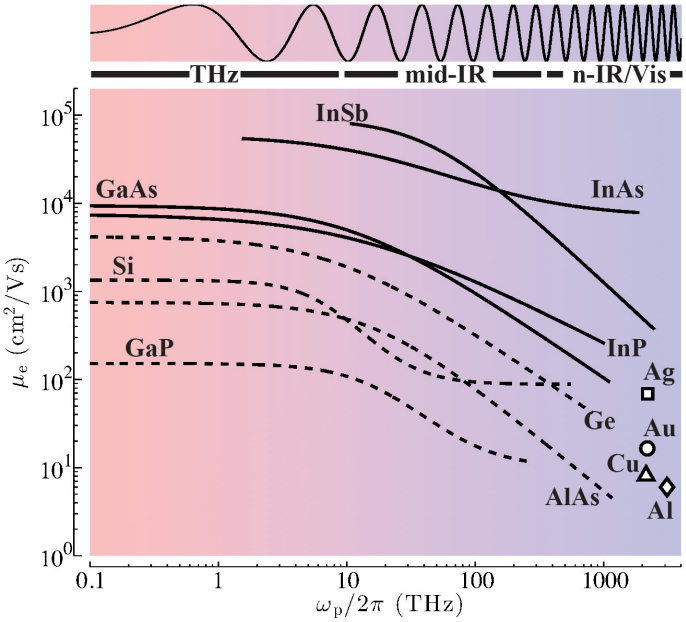

Figure 3.1: Mobility (μ_e) of doped semiconductors and metals for increasing plasma frequency and therefore carrier concentration, $\omega_\mathrm{p} \propto \sqrt{N}$, at room temperature (T=300 K). The mobilities are calculated for carrier densities that range between $10^{13}\mathrm{cm}^{-3}$ and $10^{20}\mathrm{cm}^{-3}$. The solid and dashed lines illustrate semiconductors with direct and indirect energy bandgaps respectively. The open symbols show the mobilities and plasma frequencies of some of the most frequently used metals for plasmonics and metamaterials. The above mobilities are calculated from empirical formulas based on experimental data taken from various sources[33–35].

Figure 3.1 illustrates the free electron mobility for a collection of semiconductors and metals for increasing plasma frequency. The plasma frequency in the semiconductors is tuned by increasing the concentration of free carriers in the conduction band of the semiconductor from $10^{13}\mathrm{cm}^{-3}$ to $10^{20}\mathrm{cm}^{-3}$. As shown in Fig. 3.1 the plasma frequency of the semiconductors can be tuned from far-IR (THz) to visible frequencies

in a continuous way.

As it can be appreciated by this figure the mobility of carriers decreases as a function of the plasma frequency, which is a result of the increased electron-electron scattering rate. Semiconductors with narrow bandgaps and small carrier effective masses (m_{eff}), such as InSb and InAs, have the highest mobilities at room temperature with $\mu_{\text{e}}^{\text{InSb}} \simeq 8 \times 10^4$ cm^2/Vs and $\mu_{\text{e}}^{\text{InAs}} \simeq 5.5 \times 10^4$ cm^2/Vs respectively. The tuneability of the plasma frequency for InSb and InAs is possible for frequencies above $\omega_{\text{p}}^{\text{InSb}} \geq 10.4$ THz and $\omega_{\text{p}}^{\text{InAs}} \geq 1.5$ THz respectively, due to their high intrinsic carrier concentration at room temperature ($N_{\text{i}}^{\text{InSb}} = 1.8 \times 10^{16}$ cm^{-3}, $N_{\text{i}}^{\text{InAs}} = 6.4 \times 10^{14}$ cm^{-3}).

A very promising frequency range for plasmonics using semiconductors is the THz (far-IR) regime of the electromagnetic spectrum. At these frequencies the mobility of semiconductors is significantly higher than the mobility of metals at near-IR and THz frequencies, allowing doped semiconductors to be potentially better materials for plasmonics. At THz frequencies some of the semiconductors can have mobilities as high as 9×10^3 cm^2/Vs at room temperature, with their plasma frequencies easily feasible with moderate carrier concentration densities $N \sim 10^{16} - 10^{17}$ cm^{-3}.
Although due to its high mobility InSb is considered to be the best semiconductor for plasmonics, it is impractical to be used for THz plasmonics at room temperature because of the high intrinsic carrier density.
An alternative semiconductor for THz plasmonics, which is also used in nowadays electronics, is GaAs with peak mobility $\mu_{\text{e}}^{\text{GaAs}} \simeq 9.4 \times 10^3$ cm^2/Vs. The plasma frequency of GaAs can be easily modulated for more than four orders of magnitude using ion implantation (i.e. Si atoms) as well as optical excitation with photons that have energy $E_{\text{ph}} \geq E_{\text{g}} = 1.43$ eV, where E_{g} is the bandgap energy of GaAs at room temperature. In the following sections we will study the excitation of SPPs in both doped and optically excited GaAs in the frequency range $0.1 - 5$ THz.

3.3 Surface plasmon polaritons in doped semiconductors

Although the excitation of SPPs on metallic surfaces at THz frequencies has been previously studied with spoof plasmons by tailoring the dispersion relation of a metal to mimic the one of surface plasmons [36–38], very little knowledge has been developed on the excitation and propagation of SPPs using doped semiconductors [39–42]. In this section we will investigate the excitation of SPPs using doped GaAs at THz frequencies and examine how their properties are influenced due to the carrier density.

For doped semiconductors a very realistic experimentally configuration that can support SPPs (TM - surface modes) at THz frequencies is a three - layered system that is composed out of air - doped GaAs - substrate (dielectric). The solution of Maxwell's equations for a wave travelling along the x-axis, as it is illustrated in the inset of Fig. 3.2, can result into an equation for the dispersion relation that can be solved using a minimisation algorithm [3]. Figure 3.2 shows the dispersion relation of a surface wave normalised to the free space wavevector, k_{spp}/k_0, where the dark

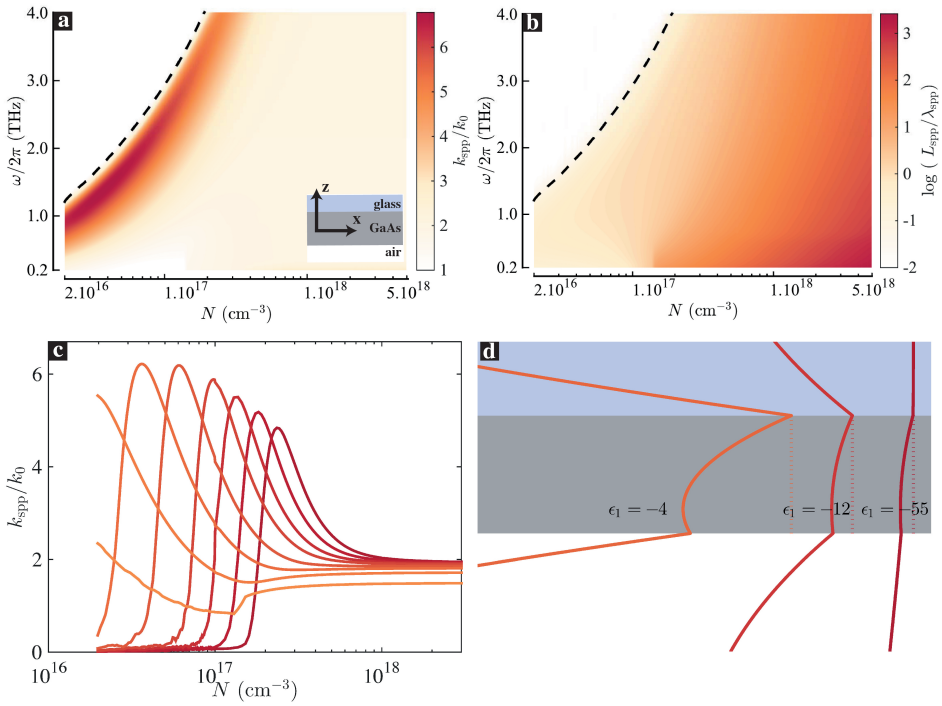

Figure 3.2: Dispersion relation of a doped semiconductor (GaAs) for increasing carrier concentration. (a) Surface plasmon polariton wavevector (k_{spp}) normalized to the free space wavevector (k_0). The black dashed line is the boundary for the surface plasmon modes that can be supported by the three layered system shown on the top left inset. (b) Surface plasmon polariton propagation length (L_{spp}) normalized to the plasmon wavelength (λ_{spp}). (c) Isofrequency cuts (horizontal cuts) as a function of the carrier density (from (a)) for the frequencies 0.5-4 THz with 0.5 THz increment step and (d) shows the normalised $E_x(z)$ component of the electric field at 1 THz for three different carrier concentrations, namely from left to right 2×10^{16} cm^{-3}, 3×10^{16} cm^{-3} and 1×10^{17} cm^{-3} respectively. The electric fields are shifted for clarity and the dotted lines indicate the base line.

dashed line illustrates the air light cone, i.e. $k_{spp}/k_0 = 1$. For these calculations the substrate is amorphous silica (SiO_2) with $\epsilon = 4$. The thickness of GaAs is 1 μm and its permittivity is described by Eq. (3.2), with[33] $\epsilon_\infty = 12.85$, $m_{eff} = 0.063\ m_e$, $\Gamma_p = 0.072$ THz, $\omega_{TO}/2\pi = 8$ THz, $\omega_{LO}/2\pi = 8.54$ THz, and the mobility of free carriers (μ_e) is taken from Fig. 3.1.

As it is apparent from Fig. 3.2(a) the normalized wavevector has the highest values for relatively low carrier densities that correspond to permittivities close to the transition between dielectric and metallic nature of the semiconductor. The bottom left panel, Fig. 3.2(c), shows isofrequency cuts for the frequencies in the range 0.5 - 4 THz with 0.5 THz increment step (from light orange to dark red). Three regions

of interest can be identified in this plot that are manifestations of three different physical effects, all at the same frequency. In the first region, for low carrier densities, the semiconductor behaves as a dielectric $\tilde{\epsilon} > 0$ and therefore no plasmonic modes can be supported since the in-plane wavevector falls inside the light cone region, i.e. $k_{\mathrm{spp}}/k_0 < 1$. For slightly higher carrier concentrations we observe a transition from dielectric to plasmonic nature, where this transition coincides with a change in the permittivity of the semiconductor from positive to negative. The plasmonic regime extends over a narrow set of carrier densities until it reaches a maximum and begin a gradual transition to a perfect-electric-conductor-like behaviour (PEC).

These three regions are also illustrated by the in-plane propagation length normalized to the plasmon wavelength (λ_{spp}) as shown on a logarithmic scale in Fig. 3.2(b). For low carrier densities the propagation of the SPP modes is limited to a few plasmon wavelengths, behaviour which is characteristic for plasmonic systems since the penetration of the propagating electric field inside the doped semiconductor suffers significant losses that results into short propagation lengths. On the other end, when the carrier density is high, the propagation length can have values that are several orders of magnitude larger than the SPP wavelength (λ_{spp}). This is due to the limited losses of a PEC-like material because the propagating electric field is predominantly in the surrounding dielectrics (air or glass), causing little to almost no attenuation. The normalised profile of the $E_x(z)$ component of the electric field is shown in Fig. 3.2(d) for three different carrier concentrations at 1 THz. The carrier densities of the semiconductor correspond to permittivities with values $\tilde{\epsilon} = -4 + 12i$, $\tilde{\epsilon} = -12 + 18i$ and $\tilde{\epsilon} = -55 + 64$ from left to right respectively. The electric field shown for the three different permittivities corresponds to the anti-symmetric TM mode and it is evident that for permittivities close to the transition between metal and dielectric ($\epsilon_1 = -1$), the electric field is well confined on the glass/semiconductor and air/semiconductor interfaces. As the permittivity of the semiconductor becomes more negative the anti-symmetric mode is less confined at the two interfaces and it mainly exists in both air and substrate.

The transition from dielectric to plasmonic and to PEC behaviour in GaAs as it is shown in Fig. 3.2 can be generalized to other semiconductors as well. In fact, a previous theoretical study on semiconducting bowtie antennas made out of InSb [43] has shown that the near field enhancement provided by such antennas has a very similar profile as the one described above, which is a result of the excitation of SPP modes.

Doped semiconductors could potentially allow the design of tunable plasmonic devices that can be easily integrated in future opto-electronic devices. In the following section we will investigate the excitation of SPPs by photo-excitation of free electrons from the valence band to the conduction band of a semiconductor.

3.4 Photo-generated surface plasmon polaritons

Recent studies have demonstrated experimentally the photo-excitation and active control of SPPs at THz frequencies using Si[15,28] and GaAs[29] (Chapter 4). The use of photo-excited semiconductors as an alternative to doped semiconductors allows the ultrafast control of the optical properties of the material and therefore of its dielectric, plasmonic and PEC behaviour.

The excitation of surface plasmon modes on optically illuminated semiconductors will be the subject of this section. These modes can be excited on a dielectric-semiconductor-dielectric system that is more complicated than the one studied in the previous section because the Beer-Lambert exponential-like absorption of light will result in a non-homogeneous carrier density over the thickness of the semiconductor. Furthermore, as we will show later in this section, the surface modes are subjected to the ultrafast carrier dynamics of the semiconductor, such as free carrier diffusion and recombination that change the optical properties of the material as a function of time and can result to time dependent surface plasmon modes.

3.4.1 Optical excitation of free carriers

The density of optically excited (pumped) free carriers depends on the number of photons absorbed by the semiconductor, which in the linear regime obeys the Beer-Lambert law with an exponential-like absorption profile,

$$N_{\mathrm{ph}}(z) = N_{\mathrm{ph}}(0)e^{-\alpha z}, \tag{3.3}$$

where $\alpha = 4\pi\kappa/\lambda_{\mathrm{p}}$ is the absorption coefficient, which is proportional to the extinction coefficient of the semiconductor, κ, and inversely proportional to the wavelength of light, λ_{p}. The initial photon number, $N_{\mathrm{ph}}(0)$, is proportional to the optical fluence, Φ, which is the energy of light contained in a single pulse per unit area, typically measured in $\mu\mathrm{J/cm}^2$. For a pulsed laser with repetition rate f_{r} and average power P, the energy per pulsed is defined as $E = P/f_{\mathrm{r}}$ and the fluence is related to the the overall number of photons by,

$$\Phi = \frac{E}{A} = N_{\mathrm{ph}}(0)\frac{hc}{\lambda_{\mathrm{p}}}, \tag{3.4}$$

where $h = 6.63 \cdot 10^{-34}$ J·s is the Plank's constant. The rate of absorbed photons by the semiconductor and therefore the rate of carrier generation is given by,

$$N_{\mathrm{e}} = -\frac{dN_{\mathrm{ph}}}{dz} = \alpha\,(1-R)\,\Phi\frac{\lambda_{\mathrm{p}}}{hc}\;e^{-\alpha z}, \tag{3.5}$$

where the Fresnel reflection coefficient, R, from the surface of the semiconductor was taken into account. Based on the pulse fluence (Φ) the optical properties of the semiconductor can be actively tuned in a continuous manner, which in turn allows the permittivity of having a wide range of values that extends from the permittivity of a dielectric to the one of a PEC.

Figure 3.3 illustrates the dependence of the permittivity of GaAs as a function of the sample depth for a collection of carrier concentrations. In contrast to the

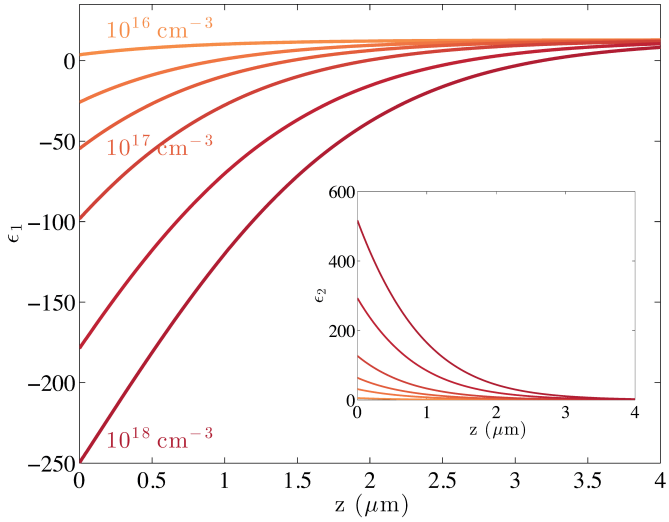

Figure 3.3: Real ϵ_1 and imaginary ϵ_2 (inset) permittivity of GaAs as a function of the sample depth for various carrier concentrations ranging from 10^{16} cm^{-3} to 10^{18} cm^{-3}. The calculation was performed using Eq. (3.2) and Eq. (3.5) with absorption coefficient $\alpha^{-1} = 0.75$ μm at $\lambda_p = 0.8$ μm.

homogeneously doped GaAs, where the permittivity is constant whatever the thickness of the semiconductor is, Fig. 3.3 reveals that the real and imaginary (inset) part of the permittivity is depth dependent and in addition it follows an exponential-like profile which is a consequence of the Beer-Lambert absorption of photons by the semiconductor. Therefore, it is clear that for a given carrier concentration the permittivity of the semiconductor undergoes variations from an almost PEC to dielectric. As it will be discussed in the next subsection this exponential-like profile can have beneficial effects on the profile of the surface plasmon modes.

Furthermore, the depth of the photo-excited metallic area can be actively controlled by changing the optical pump wavelength (λ_p), which will result into a variation of the absorption coefficient (α).

3.4.2 Photo-excited surface plasmons

The excitation of surface plasmons on optically excited semiconductors can be described by solving Maxwell's equations for TM waves. While there are well established analytical solutions for surface waves supported by simple systems (see previous section on doped-semiconductors), the spatial variation of the permittivity in the metallic region does not allow for an analytical solution and therefore numerical methods

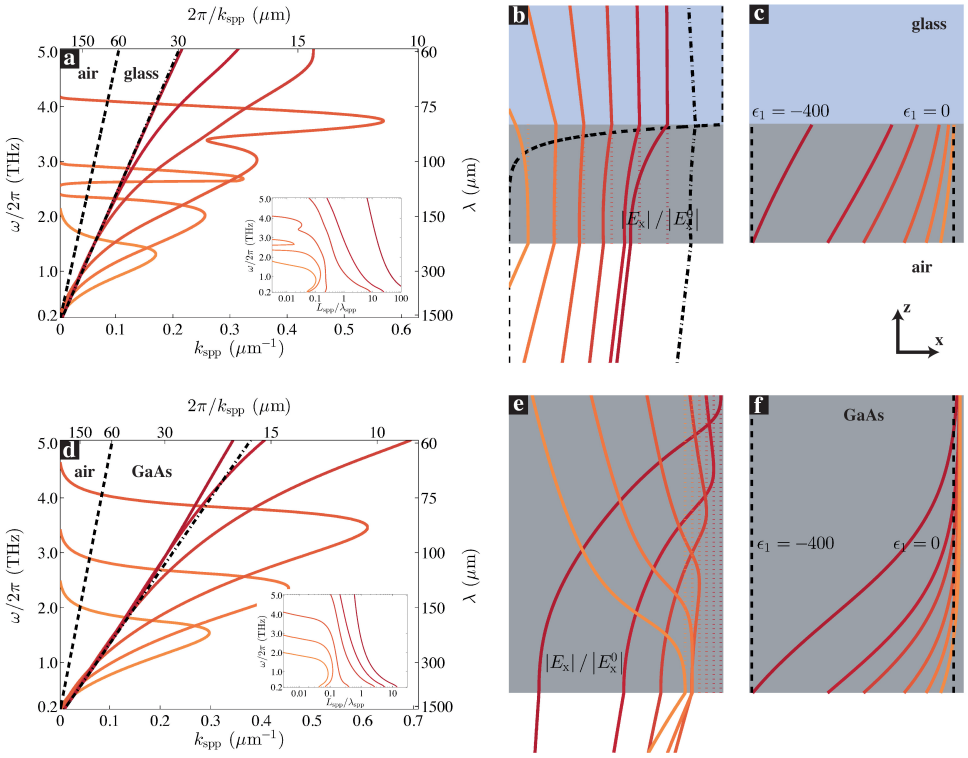

Figure 3.4: Photo-generated surface plasmons on GaAs for 1 μm (a)-(c) and 8 μm (d)-(f) for various carrier concentrations. (a) and (d) Dispersion relation of the photo-generated plasmons on a 1 μm and 8 μm $>> \alpha^{-1} = 0.75$ μm thick GaAs on top of a glass substrate with $\tilde{\epsilon} = 4$ and of an undoped GaAs with $\tilde{\epsilon} = 12.85$ respectively. The black dashed and dashed-dotted lines indicate the light cones for air and substrate respectively. The inset shows the propagation length (L_{spp} - 1/e decay) of the SPP mode normalized to the plasmon wavelength (λ_{spp}). The carrier densities shown in these figures correspond to $5 \cdot 10^{16}$ cm^{-3}, $1 \cdot 10^{17}$ cm^{-3}, $2 \cdot 10^{17}$ cm^{-3}, $5 \cdot 10^{17}$ cm^{-3}, $1 \cdot 10^{18}$ cm^{-3} and $5 \cdot 10^{18}$ cm^{-3} from orange to red respectively. (b,e) Normalised electric field profiles, $|E_x(z)|$ and (c-f) real part of the permittivity for photo-excited GaAs, $\epsilon_1(z)$ calculated at $\nu = 1$ THz for a collection of carrier densities. The black dashed line and dashed-dotted line in (b) shows the TM mode for a 1 μm thick Au and homogeneously doped GaAs ($N = 2 \cdot 10^{17}$ cm^{-3}) respectively, surrounded by air and glass for comparison.

have to be utilized. To take into account for the non-homogeneous permittivity we have divided the photo-excited region into infinitesimally small layers for which the permittivity between consecutive layers can be considered constant. Consecutively, we solve Maxwell's equations for TM waves subjected to the continuity equations at all the interfaces, as it is illustrated in Appendix A.

For our study we focus on two types of systems, that can be both realized ex-

perimentally[29,31]. The first one is a semiconductor with thickness comparable to its absorption length ($L = 1\ \mu\text{m} \sim \alpha^{-1}$) on a substrate, such that the photo-excitation is approximately homogeneous as a function of the thickness. For the second configuration we used a semiconductor with thickness much larger than its absorption length ($L >> \alpha^{-1}$) such as a standard, commercially available wafer. This type of semiconductor is separated into two sections, namely the optically excited region and the substrate region with permittivity equal to $\tilde{\epsilon} = \epsilon_\infty$, which is the permittivity of the bulk semiconductor without the contribution of any phonon resonances since they are situated at frequencies higher than the frequency range studied in this chapter.

Figures 3.4(a) and 3.4(d) show the dispersion of the two systems for a number of carrier densities that range from 5×10^{16} cm^{-3} to 5×10^{18} cm^{-3}. For the 1 μm GaAs on a substrate we have divided the photo-excited region into 20 layers while for the thicker sample we used an 8 μm thick photo-excited region divided into 80 layers, since for an above the bandgap excitation ($\lambda_\text{p} = 800$ nm) and at this depth the absorption of photons is nearly zero and therefore the permittivity is equal to the bulk permittivity of GaAs, $\tilde{\epsilon} = \epsilon_\infty$.

By increasing the carrier density (orange to red curves) we observe that for a fixed frequency there is a transition from a plasmonic to a PEC behaviour since the dispersion curve converges to the light cone of the substrate indicated by a black dashed-dotted line. Furthermore, relative to the free-space wavevector (k_0), the photo-excited wafer appears to have larger in-plane wavevector than the thin semiconductor by approximately a factor of two. This is also evident from the insets of Fig. 3.4(a, d) where the propagation length (L_spp - 1/e amplitude decay) normalised to the surface plasmon wavelength (λ_spp) is marginally smaller for the optically excited wafer than for the optically excited thin semiconductor. Furthermore, even though we observe sort propagation lengths for both thin and thick semiconductors at certain carrier densities, by tuning the carrier densities accordingly an overall propagation of hundred times the plasmon wavelength can be achieved.

The dispersion curves for carrier densities $1 \cdot 10^{17}$ cm^{-3} and $2 \cdot 10^{17}$ cm^{-3} exhibit a distinct feature around 2.5 THz and 3.5 THz respectively. Our analysis has shown that these very apparent features are connected with surface plasmon frequencies that originate from the inhomogeneous free carrier distribution in the bulk of the semiconductor. In particular the first surface plasmon frequency ($\omega_\text{sp}^{(1)}$) is linked to the initial carrier density, $N_e(z = 0)$, while the second surface plasmon frequency ($\omega_\text{sp}^{(2)}$) is linked to an average carrier density, $N_e^\text{av}(0 < z < L)$, along the depth of the semiconductor. For these two carrier densities we can associate two transitions from metal to dielectric. Further calculations have shown that this distinct double plasmonic behaviour depends also on the permittivity of the substrate. In the limit where the permittivity of the substrate approaches the permittivity of the bulk semiconductor, this feature disappears completely (Fig. 3.4(d)).

To get a deeper understanding of the surface plasmon modes, in both thick and thin semiconductor systems, Figs. 3.4(b, e) show the normalised $|E_x(z)|$ component of the electric field, which is the anti-symmetric TM mode. The electric fields in both

figures are shifted for clarity and the dotted lines illustrate the base lines. Figures. 3.4(c, f) illustrate the real part of the permittivity as a function of the depth. For high carrier densities (red curves), although the permittivity has an exponential-like profile, the penetration depth of THz waves inside the semiconductor is significantly small and results into a very poor confinement of the wave on the surface of the semiconductor. Since most of the wave is situated in the dielectric medium (air) the surface wave propagates with negligible attenuation for many wavelengths. As the carrier density becomes smaller (orange lines) and therefore the permittivity of the semiconductor approaches the value of $\epsilon_1 = -1$, the penetration of the wave inside the semiconductor becomes larger. As a result a significant fraction of the wave is confined inside the semiconductor instead in the dielectric, allowing for large field intensities per volume in concession of propagation length. In addition, it is evident from Fig. 3.4(e) that even though there is no physical boundary inside the semiconductor, the transition from metal to dielectric at depths well inside the bulk of the semiconductor defines an active boundary for the surface plasmon mode. The position of the active boundary can be tuned by varying the photo-generated carrier density.

3.4.3 Dynamics of photo-excited surface plasmons

Following the optical excitation of free carriers, the permittivity of the semiconductor will be dominated by the dynamics of free carriers, such as carrier diffusion and recombination. As a result, the change in the permittivity will induce a distinct variation on the SPPs properties. As will be explained in more detail later in this section, the carrier diffusion will rearrange the distribution of free carriers inside the semiconductor on a picosecond time scale, resulting into a spatially dependent permittivity that deviates from the exponential-like profile discussed previously. Furthermore, the carrier density will be progressively reduced due to surface and bulk recombination, resulting into a change in the behaviour of the semiconductor from metallic to dielectric on a sub-picosecond to millisecond time scales.

The dynamics of an optically excited semiconductor are governed by the continuity equation, which takes into account the change of the carrier density due to carrier generation and recombination, as well as the currents flowing in the semiconductor, which in the absence of an external potential is equal to the diffusion of free carriers. The continuity equation can be summarized in the following expression [44],

$$\frac{\partial}{\partial t_\mathrm{p}} N_\mathrm{e}(z, t_\mathrm{p}) = G_\mathrm{e}(z, t_\mathrm{p}) - R_\mathrm{e}(t_\mathrm{p}) + D \frac{\partial^2}{\partial z^2} N_\mathrm{e}(z, t_\mathrm{p}), \tag{3.6}$$

where t_p is the pump-probe time, namely the time between the optical excitation of the free carriers and the time of the surface plasmon excitation which takes values between $t_0 \leq t_\mathrm{p} \leq \infty$, while z is the depth of the semiconductor and ranges between $0 \leq z \leq L$. The first term on the right side is the carrier generation term, which can be approximated by Eq. (3.5),

$$G_\mathrm{e}(z, t_\mathrm{p}) = \alpha \, (1 - R) \, \Phi \frac{\lambda_\mathrm{p}}{hc} \; \delta \, (t_\mathrm{p} - t_0) \; \; e^{-\alpha z}, \tag{3.7}$$

where the Kronecker delta function ensures that the carrier generation occurs at a time $t_p = t_0$. The second term of the continuity equation accounts for all the recombination mechanisms, i.e.,

$$R_e(z, t_p) = -\left(\frac{N_e}{\tau_b} + \frac{N_e^2}{\tau_r} + \frac{N_e^3}{\tau_\gamma}\right), \tag{3.8}$$

where τ_b is the non-radiative bulk recombination rate, τ_r is the radiative bimolecular recombination rate and τ_γ is the Auger recombination rate[45]. The third term of Eq. (3.6) is the carrier diffusion mechanism, where D is the diffusion coefficient. In the most general case the continuity equation is subjected to Robin boundary conditions (BCs), where the non-radiative surface recombination (s) on both interfaces has to be taken into account (see Appendix B). The solution of the continuity equation will determine the permittivity of the semiconductor (Eq. (3.2)), which does not only depend on the spatial distribution of the free carriers but also on the pump-probe time, $\tilde{\epsilon} = \tilde{\epsilon}(\omega, z, t_p)$.

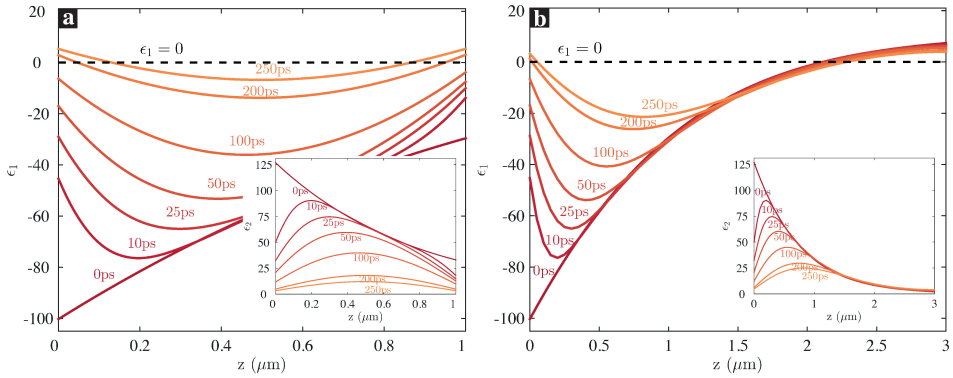

Figure 3.5: Dynamics of the spatially dependent permittivity for various pump-probe times at 1 THz for initial carrier density $N_e = 2 \cdot 10^{17}$ cm^{-3}. (a) Real and imaginary (inset) permittivity of an optically excited $L = 1$ μm GaAs on a glass substrate and (b) of GaAs with thickness larger than the absorption length, $L = 8$ μm $>> \alpha^{-1}$.

Figure 3.5 shows the permittivity of GaAs for various pump-probe times at 1 THz for the thin and thick optically excited semiconductor. The carrier density at $t_p = t_0$ was chosen to be $N_e = 2 \cdot 10^{17}$ cm^{-3}, the diffusion coefficient $D = 10^{-3}$ m^2/s, the surface recombination[46] $s_1 = s_2 = 8.5 \cdot 10^3$ m/s, the bulk recombination $\tau_b = 1$ ns, while for simplicity we have omitted the non-linear recombination terms. For both the thin and thick GaAs, the spatially dependent permittivity at $t_p = t_0$, has an exponential profile due to the Beer-Lambert absorption (see carrier generation mechanism Eq. (3.7)). For larger pump-probe times the carriers diffuse in both directions, while their motion is restricted by the boundaries of the semiconductor, i.e. $z_1 = 0$ μm and $z_2 = 1$ μm (see Fig. 3.5(a)). When the free carriers interact with the two boundaries of GaAs a fraction of the carriers suffers surface recombination due to lattice

imperfections and impurities at the semiconductor surface, while the remaining carriers are "reflected" back to the semiconductor. In addition to the surface recombination at the two boundaries, the free carriers diffusing in the semiconductor will experience bulk recombination, which results into a modification of the optical properties of GaAs from metallic to dielectric in just 250 ps.

The apparent difference in the optical properties between the two semiconducting systems (thin and thick layers) is a result of the surface recombination mechanism which is effectively absent on the back surface of the thick GaAs. As shown in Fig. 3.5(b) the lack of surface recombination at one of the two boundaries appears to slow down the transition from a metallic to a dielectric behaviour. In addition, our calculations show that for even thinner semiconducting systems the dynamics governing the motion of the free carriers is faster, reaching metal-to-dielectric transition times in the order of few picoseconds, which can be potentially beneficial for opto-electronic devices with ultrafast switching times.

As it was illustrated in the previous section, an optically excited semiconductor can support SPPs (see Fig. 3.4). The dynamics of the propagating surface plasmons are strongly influenced by the diffusion and recombination processes in the semiconductor. To study the dynamics of SPPs we utilize a similar approach as the one used in the previous section and described in Appendix A. In particular, the surface plasmon modes are calculated for a multilayered system, which is composed out of a semiconductor with spatially and temporally dependent permittivity, as shown in Fig. 3.5, and surrounded by two dielectrics.

Figure 3.6 summarizes the dynamics of SPPs for the thin (a-c) and thick (d-f) GaAs with an initial carrier density of $N_e = 2 \cdot 10^{17}$ cm^{-3}. The calculated surface plasmon modes correspond to pump-probe times $t_p = 0,\ 10,\ 25,\ 50,\ 100,\ 200,\ 250$ ps from red to orange respectively. The temporal evolution of the in-plane wavevector (k_{spp}) for the thin semiconductor, Fig. 3.6(a), appears to be larger than the in-plane wavevector of the homogeneously doped semiconductor, shown with a black line, for all the frequencies. This is due to the fact that the thickness of the optically excited GaAs is effectively thinner than the homogeneously doped GaAs and defined by the absorption length at the pump wavelength. Furthermore, at a particular frequency (i.e. 1 THz) we observe that at very short pump-probe times the dispersion of the plasmonic mode is very close to the light cone (black-dotted line for glass and black dashed line for air) and as the carriers diffuse and recombine the in-plane wavevector reaches values of around ten times the free space wavevector. For even larger pump-probe times the plasmonic mode vanishes. The above three stages are strongly linked to the transitions from dielectric to plasmonic and to PEC-like nature as discussed earlier, although now it is evolving in the reverse order. This is because upon the optical excitation of free carriers ($t_p = 0$) the semiconductor behaves like a PEC with a large negative permittivity (see Fig. 3.5) causing the surface mode wavevector to be restricted very close to the air light cone (black dashed line). While the carrier recombination mechanisms reduce the amount of free carriers in the conduction band of the semiconductor the permittivity converges to the value of $\tilde{\epsilon} = -1$, resulting therefore to the largest value of the in-plane wavevector. In the limit of very large pump-probe times the density of free carriers

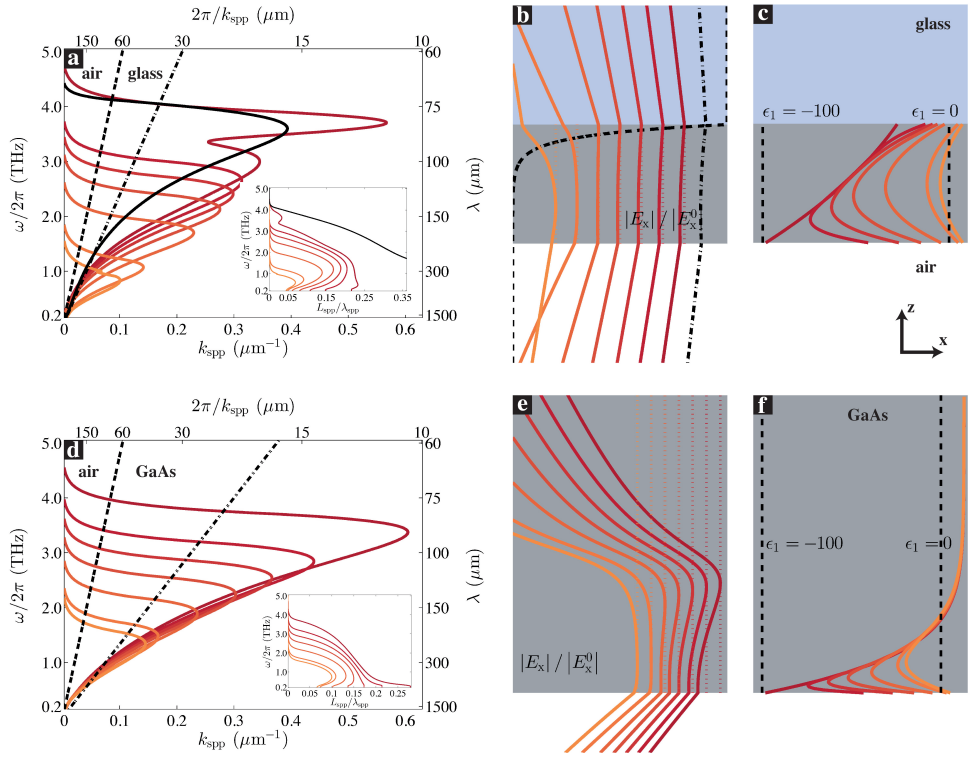

Figure 3.6: Dynamics of photo-generated surface plasmons on GaAs for 1 μm (a)-(c) and 8 μm (d)-(f) for various pump-probe times. The initial carrier density was fixed for all the pump-probe times at $N_e = 2 \cdot 10^{17}$ cm^{-3}. The color lines represent the different times after the photo-excitation of free carriers, namely t_p = 0, 10, 25, 50, 100, 200, 250 ps from red to orange respectively, while the black dash-dotted line represents a homogeneously doped GaAs. (a) and (d) Dispersion relation of the photo-generated plasmons on a 1 μm and 8 μm thick GaAs on top of a glass substrate with $\tilde{\epsilon} = 4$ and of an undoped GaAs with $\tilde{\epsilon} = 12.85$ respectively. The two shaded areas indicate the light cones for air and substrate respectively. The inset shows the propagation length (L_{spp} - 1/e decay) of the SPP mode normalized to the plasmon wavelength (λ_{spp}). (b-c) Electric field profiles, $E_z(z)$ and (e-f) real part of the permittivity for photo-excited GaAs, $\epsilon_1(z)$ calculated at $\nu = 1$ THz. The black dotted line in (b) shows the TM mode for a 1 μm thick Au surrounded by air and glass for comparison.

is further reduced causing the semiconductor to behave like a dielectric, and hence forcing the surface plasmon polariton mode to disappear. The dispersion of the thick GaAs, Fig. 3.6(d), displays very similar dynamics as the one of Fig. 3.6(a) with the difference that the transition from PEC-like to plasmonic and to dielectric is slower. The slower transition is a consequence of the slower carrier dynamics in the thicker semiconductor which is due to the effectively absent surface recombination at one of the two interfaces.

Since surface recombination is the main mechanism that causes reduction of the carrier density, even slower transitions can be achieved by reducing the amount of surface defects, normally by surface passivation [47]. On the other hand, for faster transitions, in the order of few picoseconds, reducing the thickness of the semiconductor will cause the free carriers to interact more frequently with the two surfaces, reducing therefore the carrier density at a much higher rate.

The dynamics of the electric field for the propagating anti-symmetric surface plasmon mode $E_x(z, t_\mathrm{p})$ is shown in Figs. 3.6(b),(e) for the thin and thick semiconductor respectively, while for illustrative purposes Figs. 3.6(c),(f) shows the permittivity of the semiconductor at 1 THz. As it is clear from the electric field profiles, for pump-probe times right after the photo-excitation of free carriers, there is a limited penetration of the THz fields into the semiconductor as it is expected for PEC-like materials. Surprisingly the surface recombination at the front surface of the semiconductor ($z = 0$ μm), which causes a considerable change to the permittivity of the semiconductor does not affect significantly the electric field profile. For longer pump-probe times the electric field is more bounded to the surface of the semiconductor, a characteristic profile of plasmonic modes. For $t_\mathrm{p} = 250$ ps the surface plasmon mode excited in the thin semiconductor is significantly influenced by the surface recombination at both surfaces of the semiconductor, namely $z = 0$ μm and $z = 1$ μm. As a result the mode exists inside the semiconductor and it is surrounded by a dielectric with higher permittivity than the surrounding air and glass (bulk GaAs), causing a better electric field confinement on the surface of the semiconductor.

For comparison purposes, Fig. 3.6(b) shows with black dashed line and black dashed-dotted line the electric field profiles of a 1 μm thick gold (Au) and 1 μm thick homogeneously doped GaAs ($N_\mathrm{e} = 2 \cdot 10^{17}$ cm^{-3}) respectively. It is clear that Au behaves as a PEC since the penetration of the THz field inside Au is in the range of few tens of nanometers. On the other hand, the penetration of the THz electric field inside the homogeneously doped GaAs is slightly better, however as in the case of $t_\mathrm{p} = 0$ ps (red line) the confinement of the electric field at the semiconductor surface is weak.

3.5 Conclusions

In conclusion, we have studied the properties of photo-excited SPPs on optically excited and doped semiconductors at THz frequencies. In particular, we have examined the use of semiconductors as an alternative to noble metals for plasmonics at THz frequencies, pointing out that plasmonic devices made out of semiconductors can be easily integrated with the current semiconductor-based technology. Moreover, we have studied the influence of the carrier density on the properties of surface plasmon polaritons for doped and optically excited semiconductors identifying a transition of the TM-mode through three distinct regions of interest, namely dielectric, plasmonic and perfect electric conductor. In addition we have examined the dynamics of SPPs that originate from physical processes in the semiconductor such as carrier diffusion

and recombination. These processes are responsible for a spatially and temporally dependent pemrittivity of the semiconductor, which in turn affects the properties of surface plasmon polaritons.

Our results illustrate the tuneability and dynamics of photo-excited SPPs using semiconductors at THz frequencies. The versatile nature of semiconductors can provide a plethora of possibilities ranging from plasmonic antennas [29,30], where strong confinement is necessary, to non-lossy waveguides [48] where long propagations distances are required.

Bibliography

[1] E. Ozbay, *Plasmonics: Merging Photonics and Electronics at Nanoscale Dimensions*, Science **311**, 189 (2006).

[2] H. A. Atwater, *The promise of plasmonics*, Scientific American **296**, 56 (2007).

[3] S. A. Maier, *Plasmonics: Fundamentals and Applications*, Springer US, 2007.

[4] W. L. Barnes, A. Dereux, and T. W. Ebbesen, *Surface plasmon subwavelength optics*, Nature **424**, 824 (2003).

[5] M. Moskovits, *Surface-enhanced Raman spectroscopy: a brief retrospective*, Journal of Raman Spectroscopy **36**, 485 (2005).

[6] P. L. Stiles, J. A. Dieringer, N. C. Shah, and R. P. V. Duyne, *Surface-Enhanced Raman Spectroscopy*, Annual Review of Analytical Chemistry **1**, 601 (2008).

[7] E. F. Schubert and J. K. Kim, *Solid-State Light Sources Getting Smart*, Science **308**, 1274 (2005).

[8] G. Lozano, D. J. Louwers, S. R. Rodriguez, S. Murai, O. T. Jansen, M. A. Verschuuren, and J. Gomez Rivas, *Plasmonics for solid-state lighting: enhanced excitation and directional emission of highly efficient light sources*, Light Sci Appl **2**, e66 (2013).

[9] S. Sanchez, C. De Matos, and M. Pugnet, *Instantaneous optical modulation in bulk GaAs semiconductor microcavities*, Applied Physics Letters **78**, 3779 (2001).

[10] V. Van, T. Ibrahim, K. Ritter, P. Absil, F. Johnson, R. Grover, J. Goldhar, and P.-T. Ho, *All-optical nonlinear switching in GaAs-AlGaAs microring resonators*, Photonics Technology Letters, IEEE **14**, 74 (2002).

[11] S. W. Leonard, H. M. van Driel, J. Schilling, and R. B. Wehrspohn, *Ultrafast band-edge tuning of a two-dimensional silicon photonic crystal via free-carrier injection*, Phys. Rev. B **66**, 161102 (2002).

[12] V. R. Almeida, C. A. Barrios, R. R. Panepucci, and M. Lipson, *All-optical control of light on a silicon chip*, Nature **431**, 1081 (2004).

[13] T. Nikolajsen, K. Leosson, and S. I. Bozhevolnyi, *Surface plasmon polariton based modulators and switches operating at telecom wavelengths*, Applied Physics Letters **85**, 5833 (2004).

[14] E. Hendry, M. J. Lockyear, J. Gómez Rivas, L. Kuipers, and M. Bonn, *Ultrafast optical switching of the THz transmission through metallic subwavelength hole arrays*, Phys. Rev. B **75**, 235305 (2007).

[15] E. Hendry, F. J. Garcia-Vidal, L. Martin-Moreno, J. G. Rivas, M. Bonn, A. P. Hibbins, and M. J. Lockyear, *Optical Control over Surface-Plasmon-Polariton-Assisted THz Transmission through a Slit Aperture*, Phys. Rev. Lett. **100**, 123901 (2008).

[16] J. N. Caspers, N. Rotenberg, and H. M. van Driel, *Ultrafast silicon-based active plasmonics at telecom wavelengths*, Opt. Express **18**, 19761 (2010).

[17] J. Dintinger, I. Robel, P. Kamat, C. Genet, and T. Ebbesen, *Terahertz All-Optical Molecule- Plasmon Modulation*, Advanced Materials **18**, 1645 (2006).

[18] R. A. Pala, K. T. Shimizu, N. A. Melosh, and M. L. Brongersma, *A Nonvolatile Plasmonic Switch Employing Photochromic Molecules*, Nano Letters **8**, 1506 (2008).

[19] D. Pacifici, H. J. Lezec, and H. A. Atwater, *All-optical modulation by plasmonic excitation of CdSe quantum dots*, Nat Photon **1**, 402 (2007).

[20] S. Y. Park and D. Stroud, *Surface-Enhanced Plasmon Splitting in a Liquid-Crystal-Coated Gold Nanoparticle*, Phys. Rev. Lett. **94**, 217401 (2005).

[21] G. Xu, Y. Chen, M. Tazawa, and P. Jin, *Surface Plasmon Resonance of Silver Nanoparticles on Vanadium Dioxide*, The Journal of Physical Chemistry B **110**, 2051 (2006).

[22] G. Xu, C.-M. Huang, M. Tazawa, P. Jin, and D.-M. Chen, *Nano-Ag on vanadium dioxide. II. Thermal tuning of surface plasmon resonance*, Journal of Applied Physics **104** (2008).

[23] W. Dickson, G. A. Wurtz, P. R. Evans, R. J. Pollard, and A. V. Zayats, *Electronically Controlled Surface Plasmon Dispersion and Optical Transmission through Metallic Hole Arrays Using Liquid Crystal*, Nano Letters **8**, 281 (2008).

[24] N. Rotenberg, M. Betz, and H. M. van Driel, *Ultrafast control of grating-assisted light coupling to surface plasmons*, Opt. Lett. **33**, 2137 (2008).

[25] N. Rotenberg, J. N. Caspers, and H. M. van Driel, *Tunable ultrafast control of plasmonic coupling to gold films*, Phys. Rev. B **80**, 245420 (2009).

[26] K. F. MacDonald, Z. L. Samson, M. I. Stockman, and N. I. Zheludev, *Ultrafast active plasmonics*, Nat. Photonics **3**, 55 (2009).

[27] N. Rotenberg, M. Betz, and H. M. van Driel, *Ultrafast All-Optical Coupling of Light to Surface Plasmon Polaritons on Plain Metal Surfaces*, Phys. Rev. Lett. **105**, 017402 (2010).

[28] A. Berrier, R. Ulbricht, M. Bonn, and J. G. Rivas, *Ultrafast active control of localized surface plasmon resonances in silicon bowtie antennas*, Opt. Express **18**, 23226 (2010).

[29] G. Georgiou, H. K. Tyagi, P. Mulder, G. J. Bauhuis, J. J. Schermer, and J. G. Rivas, *Photo-generated THz antennas*, Sci. Rep. **4** (2014).

[30] G. Georgiou, C. Tserkezis, M. C. Schaafsma, J. Aizpurua, and J. Gómez Rivas, *Active loaded plasmonic antennas at terahertz frequencies: Optical control of their capacitive-inductive coupling*, Phys. Rev. B **91**, 125443 (2015).

[31] I. Chatzakis, P. Tassin, L. Luo, N.-H. Shen, L. Zhang, J. Wang, T. Koschny, and C. M. Soukoulis, *One- and two-dimensional photo-imprinted diffraction gratings for manipulating terahertz waves*, Applied Physics Letters **103**, 043101 (2013).

[32] P. Tassin, T. Koschny, M. Kafesaki, and C. M. Soukoulis, *A comparison of graphene, superconductors and metals as conductors for metamaterials and plasmonics*, Nat Photon **6**, 259 (2012).

[33] S. Adachi, *Handbook on physical properties of semiconductors*, Springer US, 2004.

[34] P. B. Johnson and R. W. Christy, *Optical Constants of the Noble Metals*, Phys. Rev. B **6**, 4370 (1972).

[35] H. Ehrenreich, H. R. Philipp, and B. Segall, *Optical Properties of Aluminum*, Phys. Rev. **132**, 1918 (1963).

[36] J. B. Pendry, L. Martín-Moreno, and F. J. Garcia-Vidal, *Mimicking Surface Plasmons with Structured Surfaces*, Science **305**, 847 (2004).

[37] C. R. Williams, S. R. Andrews, S. A. Maier, A. I. Fernandez-Dominguez, L. Martin-Moreno, and F. J. Garcia-Vidal, *Highly confined guiding of terahertz surface plasmon polaritons on structured metal surfaces*, Nat Photon **2**, 175 (2008).

[38] J. G. Rivas, *Terahertz: The art of confinement*, Nat Photon **2**, 137 (2008).

[39] S. J. Allen, D. C. Tsui, and R. A. Logan, *Observation of the Two-Dimensional Plasmon in Silicon Inversion Layers*, Phys. Rev. Lett. **38**, 980 (1977).

[40] J. Gómez Rivas, C. Schotsch, P. Haring Bolivar, and H. Kurz, *Enhanced transmission of THz radiation through subwavelength holes*, Phys. Rev. B **68**, 201306 (2003).

[41] J. G. Rivas, M. Kuttge, P. H. Bolivar, H. Kurz, and J. A. Sánchez-Gil, *Propagation of Surface Plasmon Polaritons on Semiconductor Gratings*, Phys. Rev. Lett. **93**, 256804 (2004).

[42] J. G. Rivas, C. Janke, P. Bolivar, and H. Kurz, *Transmission of THz radiation through InSb gratings of subwavelength apertures*, Opt. Express **13**, 847 (2005).

[43] V. Giannini, A. Berrier, S. A. Maier, J. A. Sánchez-Gil, and J. G. Rivas, *Scattering efficiency and near field enhancement of active semiconductor plasmonic antennas at terahertz frequencies*, Opt. Express **18**, 2797 (2010).

[44] S. M. Sze and K. K. Ng, *Physics of semiconductor devices*, John Wiley & Sons, 2006.

[45] L. A. Coldren, S. W. Corzine, and M. L. Mashanovitch, *Diode lasers and photonic integrated circuits*, volume 218, John Wiley & Sons, 2012.

[46] M. C. Beard, G. M. Turner, and C. A. Schmuttenmaer, *Transient photoconductivity in GaAs as measured by time-resolved terahertz spectroscopy*, Phys. Rev. B **62**, 15764 (2000).

[47] C. J. Sandroff, R. N. Nottenburg, J.-C. Bischoff, and R. Bhat, *Dramatic enhancement in the gain of a GaAs/AlGaAs heterostructure bipolar transistor by surface chemical passivation*, Applied Physics Letters **51**, 33 (1987).

[48] H. K. Tyagi and J. G. Rivas, *Photo-generated THz plasmonic waveguides*, Journal of Optics **16**, 094011 (2014).

4

Photo-generated THz antennas

Electromagnetic resonances in conducting structures give rise to enhancements of local fields and extinction efficiencies. Conducting structures are conventionally fabricated with a fixed geometry that determines their resonant response. Here, we challenge this conventional approach by experimentally demonstrating the photo-generation of THz linear antennas on a flat semiconductor layer by the structured optical illumination through a spatial light modulator. Free charge carriers are photo-excited only on selected areas, which enables the definition of different conducting antennas on the same sample by simply changing the illumination pattern, thus without the need of physically structuring the sample. These results open a wide range of possibilities for an all-optical spatial control of resonances on surfaces and the concomitant control of THz extinction and local field enhancements.

4.1 Introduction

The possibility of confining electromagnetic fields in subwavelength volumes has been a main motivation driving the current interest on optical plasmonics [1–3]. Optical antennas with localised resonances resulting from the coherent oscillation of conduction

electrons are characterised by large local field enhancements in subwavelength volumes. One of the greatest challenges for optical antennas and plasmonics in general is the efficient and fast active control of resonant frequencies and local fields. Coherent control of local fields by temporally shaping optical pulses [4,5] or by phase shaping of beams [6–8] has been demonstrated. Ultrafast active control of surface waves has been also achieved by the transient modulation of the dielectric function. This modulation is attained by a pump laser that induces changes in the electron distribution function and the optical properties of the metal [9–14], or by modifying the permittivity of the surrounding dielectric [15]. An alternative to metals at THz frequencies for the active control of localised resonances are high mobility semiconductors with a metallic behavior at THz frequencies [16]. Doped semiconductors have charge carrier densities that are orders of magnitude lower than in metals [17–19], which enables the excitation of resonances at THz frequencies with a similar behavior to that of metals at near- and mid-infrared frequencies [20–23]. Moreover, this characteristic offers the possibility of actively tuning THz resonances from a plasmonic behavior to that of surface currents in perfect electrical conductors by controlling the carrier density [16] (see Chapter 3). This concept has been used to modify the propagation of surface waves [24], and the resonant response of THz antennas [25] and of metamaterials structured on top of semiconducting substrates [26,27] by the photo-excitation of electrons across the semiconductor bandgap. Common to all these works is that electromagnetic fields are controlled in surfaces that have been physically structured with nano and micro-structures.

In this Chapter we demonstrate experimentally a full all-optical generation of linear antennas at THz frequencies. The photo-generation is realised by illuminating a thin GaAs layer with a laser beam shaped by a Spatial Light Modulator (SLM) to contain several micro antennas. This approach does not require any physical structuring of the sample and offers the unique possibility of controlling spatially and spectrally resonances and local fields by modifying the illumination pattern. Okada and coworkers have recently proposed the photo-generation of THz devices [28,29]. In these works, diffraction gratings were photo-generated on a Si surface by illuminating through a SLM and investigated in reflection. Chatzakis *et al.* have extended this work to GaAs gratings generated by illumination through an optical mask [30]. Also, THz beam steering using photoactive semiconductors has been recently demonstrated by Busch *et al.* [31], and photo-generated metamaterials have been theoretically proposed by Rizza *et al.* [32]. Although these works have laid a solid background for the realisation of all-optical active THz devices, they have not demonstrated experimentally the possibility of inducing resonant phenomena by the structured illumination of flat surfaces.

4.2 Setup and sample description

The measurements have been performed using the modified time-resolved THz-TDS setup that incorporates a SLM for the projection of micro-structures, as described in Chapter 2. The sample used for the experiments consists of a layer of single crystalline undoped GaAs with a thickness of 1 μm bonded to a SiO_2 substrate (see Chapter

2). Intrinsic GaAs has a dielectric behavior at THz frequencies. However, its real component of the permittivity becomes negative, hence GaAs becomes conducting, at 1 THz for carrier densities above 1.5×10^{16} cm^{-3}. These carrier densities are easy to reach by pumping the sample with an optical pulse of moderate fluence. The high electron mobility of intrinsic GaAs at room temperature ($\sim$ 7000 cm^{2}V^{-1}s^{-1}), favours the excitation of localised SPPs. Moreover, the small thickness of the semiconductor slab, which is comparable to the optical absorption length of GaAs ($L_a = \alpha^{-1} = 0.75$ μm at $\lambda_\mathrm{p} = 800$ nm), allows the (nearly) homogeneous excitation of carriers as a function of the depth in the layer. For the experiments we used pump fluences up to 80 μJ/cm^2, which excites $\sim 10^{18}$ cm^{-3} free carriers on the bright pixels of the illuminated pattern. The carrier density in GaAs at the regions illuminated by dark pixels is lower than 10^{16} cm^{-3}. Therefore, the optical pumping of GaAs with a shaped beam results into the local change of the permittivity from an insulating to a conducting state.

4.3 Photo-generated THz antennas

To demonstrate the photo-generation of THz antennas on the GaAs layer we have measured the THz extinction spectra of random arrays of rods with the same orientation generated with the same optical fluence and with different lengths. Our study has been extended to include arrays of rods with the same length but generated with different fluences. Figure 4.1(a) shows an image of a random array of rods. This image is taken by placing a CCD camera at the sample position. Their random distribution suppresses any effect due to periodicity in the THz extinction, while their horizontal alignment enables the excitation of localised SPPs for THz radiation incident with a horizontal polarization. A close view of a single linear antenna rod is shown in Fig. 4.1(b). The illuminated area (filling fraction of the rods) corresponds to 18% of the surface. The spacing between two consecutive rods was chosen to be larger than 100 μm along the long axis of the rod and 40 μm along the short axis. These distances are large enough to minimise the near field coupling between consecutive rods[33], while maximising their filling fraction to increase the THz extinction.

For the THz extinction measurements the sample was first illuminated with a pump pulse with a center wavelength $\lambda_\mathrm{p} = 800$ nm and a duration of 100 fs. Subsequently, a THz pulse was transmitted through the sample. The time delay between the optical pump and the arrival of the THz pulse was chosen to be $\Delta\tau_{p-p} = 10$ ps, which is sufficiently long to enable the relaxation of hot electrons to the lowest energy state of the conduction band[34]. Furthermore, this time delay was much shorter than the carrier recombination time, which was experimentally determined to be $\tau_r \sim 450$ ps. The THz transmission amplitude is measured within a time window of 12 ps. Over this time window the carrier diffusion length is much shorter than all the characteristic lengths in the experiment, i.e., the dimensions of the structures and the THz wavelength. Therefore, the photo-excited antennas can be described in a first approximation as having stationary dimensions and carrier density.

We measure the zeroth order differential transmission transients, $\Delta E(t)$, i.e., the

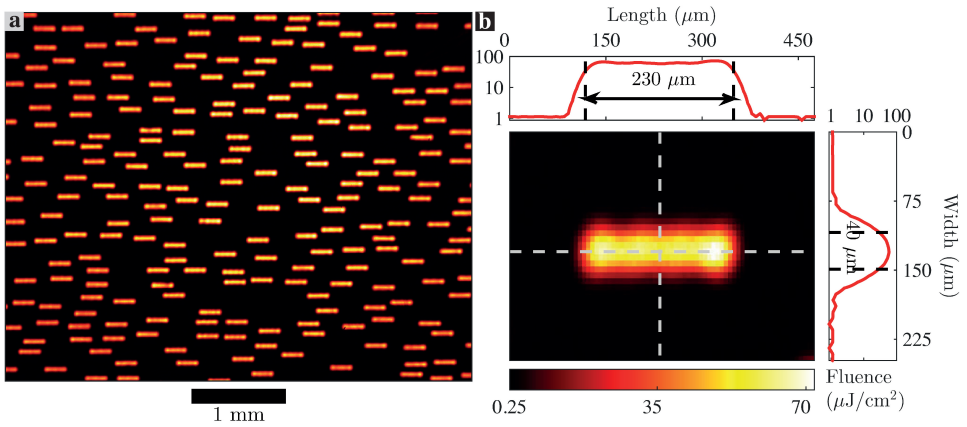

Figure 4.1: (a) Image of a random array of photo-generated rods. (b) Close view image of a single rod. The upper and right plots are the intensity profiles along the horizontal and vertical dotted lines. The vertical axis and the color scale indicate the pump fluence in μJ/cm^2. The effective dimensions of the rods are defined by the FWHM of the pump beam intensity marked by the vertical dashed lines.

THz amplitude transient transmitted through the optically pumped sample in the forward direction minus the transmitted transient of the unpumped sample $\Delta E(t) = E_{\mathrm{P}}(t) - E_{\mathrm{NP}}(t)$. These measurements are done by chopping the pump beam at half the repetition rate of the laser, i.e., 500 Hz[35], as described in Chapter 2. To gain spectral information about this transmission, the transients are Fourier transformed and squared to obtain the transmittance. The extinction $\mathcal{E}(\nu)$, defined as the sum of scattering and absorption, is given according to the optical theorem as one minus the zeroth-order transmittance. The latter is equal to the ratio of the pumped to the unpumped transmittance $\mathcal{T}_{\mathrm{P}}/\mathcal{T}_{\mathrm{NP}}$. Therefore, $\mathcal{E}(\nu) = 1 - \mathcal{T}_{\mathrm{P}}/\mathcal{T}_{\mathrm{NP}}$.

Figure 4.2 is the main result of this chapter. Figure 4.2 (a) shows the extinction spectra of photo-generated THz antennas with a fixed dimension of 230×40 μm^2 and varying optical pumping fluences. The polarization of the THz beam was set parallel to the long axis of the rods. A resonance appears in the extinction spectrum for optical fluences higher than 12 μJ/cm^2. At this fluence the number of photo-excited carriers in GaAs is large enough to give a metallic behavior to the semiconductor in the THz frequency range. The maximum extinction reaches values higher than 65% while the illuminated fraction of the GaAs is only 18%. This enhanced extinction can be explained in terms of the large THz scattering cross section of the rods resulting from their antenna like behavior. The resonance can be associated to the fundamental antenna mode, which occurs when the length of the rod is approximately equal to half the effective wavelength of the mode, i.e., $L = \lambda/(2n_{\mathrm{eff}}) - 2\delta$, where λ is the vacuum wavelength, n_{eff} the effective refractive index of the THz antenna mode defining its phase velocity[36] and δ is a parameter that leads to an apparent increase of the antenna

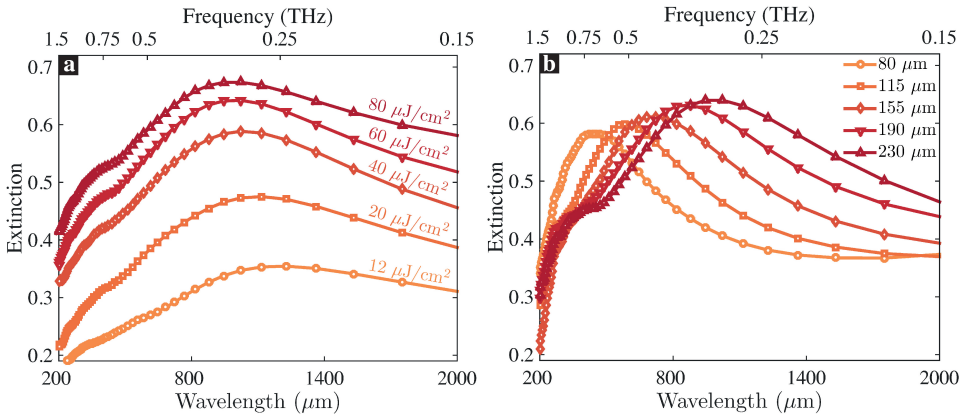

Figure 4.2: Extinction spectra of photo-generated rods on a layer of undoped GaAs. (a) The dimension of the rods is kept fixed to 230 × 40 μm^2 and the pump fluence is varied. (b) The pump fluence for the photo-generation of the rods is 70 μJ/cm^2 for all the samples and the length of the rods is varied.

length to $L + 2\delta$ due to the reactance at the ends[36,37]. This parameter depends on the antenna width and on the materials defining the antenna and its surrounding. It is thus expected to change with the pump fluence.

There is also a clear blue shift of the resonance as the pump fluence increases. This blue shift is a consequence of the increase in conductivity of the pumped GaAs and the evolution of the resonance from a plasmonic behaviour to a behaviour that approaches that of a perfect electric conductor[16]. Indeed, a larger conductivity results in a weaker penetration of the THz field in the pumped GaAs and a reduction of n_{eff}[36]. In the limit of perfect electric conductor the field does not penetrate into the metal and n_{eff} is defined by the dielectrics surrounding the antenna.

The extinction spectra of photo-generated THz linear antennas with various lengths and a fixed width of 40 μm pumped at 70 μJ/cm^2 is shown in Fig. 4.2(b). A significant redshift of the resonance and an apparent increase of the extinction is observed as the length of the photo-generated rods is increased.

In Fig. 4.3 we plot the rod length as a function of the resonant wavelength of maximum extinction. From the slope of the linear fit, illustrated by the solid line, we obtain $n_{\text{eff}} = 1.84 \pm 0.07$, while the intersection of this fit with the ordinate axis equals -2δ with $\delta = 20.8 \pm 3.9$ μm.

A closer look to Fig. 4.2(b) reveals a shoulder at shorter wavelengths (around 300 μm) in the extinction spectrum of the longer rods. We attribute this shoulder, which is absent in the spectra of the shorter rods, to the excitation of the next higher order antenna mode in a rod by normal incident THz radiation, i.e., the $3\lambda/2n_{\text{eff}}$ mode[38]. The observation of multi-polar photo-generated modes is a consequence of the high quality of the GaAs layer used for the experiments.

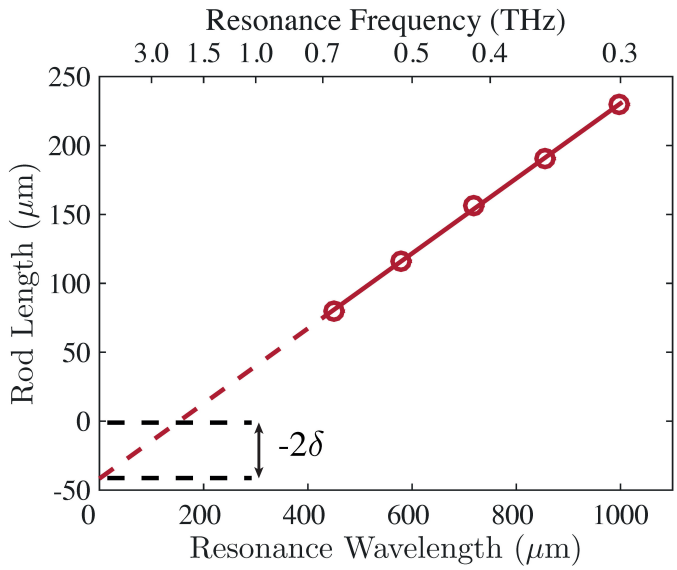

Figure 4.3: Length of photo-generated rods on an undoped GaAs layer as a function of the resonant wavelength of maximum extinction. The solid line is a linear fit to the measurements.

4.4 Numerical simulations of photo-excited antennas

To further investigate the localised modes associated to the photo-generated rods, we have performed Finite Difference in Time Domain (FDTD) simulations using a commercial software package (Lumerical Solutions).

The simulated structures were chosen to be as close as possible to the experimental conditions, i.e., a multi-layered structure consisting of air - silicon oxide - bonding polymer - GaAs - air. The experimentally determined values of the permittivity of the bonding layer and the substrate were used for the simulations. A homogeneous carrier concentration was considered through the thickness of 1 μm of the GaAs layer. The illuminated rods were simulated by considering a rectangular region with rounded corners and a permittivity given by the Drude model. A graded illumination across the edges of the rods (see side graphs in Fig. 4.1(b)) was taken into account by considering consecutive shells with varying length and a reduced carrier density as the shell dimensions are increased. The carrier density in the innermost region of the rod is $N = 2 \times 10^{18}$ cm^{-3}, while the outermost shell has $N = 5 \times 10^{16}$ cm^{-3}. The non-illuminated GaAs was assumed to have $N = 5 \times 10^{15}$ cm^{-3} to take into account the finite contrast between bright and dark pixels in the structured illumination. For the simulations we used a total field scattered field source, a perfectly matched layer as boundary of the simulated volume and a transmission monitor to determine the extinction. The simulated transmission was corrected by the rod's filling fraction to

compare quantitatively with the experiments.

Figure 4.4 (a) shows the extinction spectra of the 230 μm and 80 μm long rods. As can be appreciated in Fig. 4.4(a), this geometry reproduces reasonably well the resonance wavelength and magnitude of the extinction. Figures 4.4(b) and 4.4(c) show the near field enhancement at the GaAs-air interface and at the wavelengths of the maximum extinction for the 230 μm and 80 μm long rods respectively. The enhancement, defined as the near field intensity normalised to the incident intensity at the GaAs-air interface, has the dipolar character expected for the $\lambda/(2n_{\text{eff}})$ mode in the rod-shaped antennas. The maximum field enhancement, which is larger for the shorter rods, is achieved at the edges of the rods where the charge density is maximum.

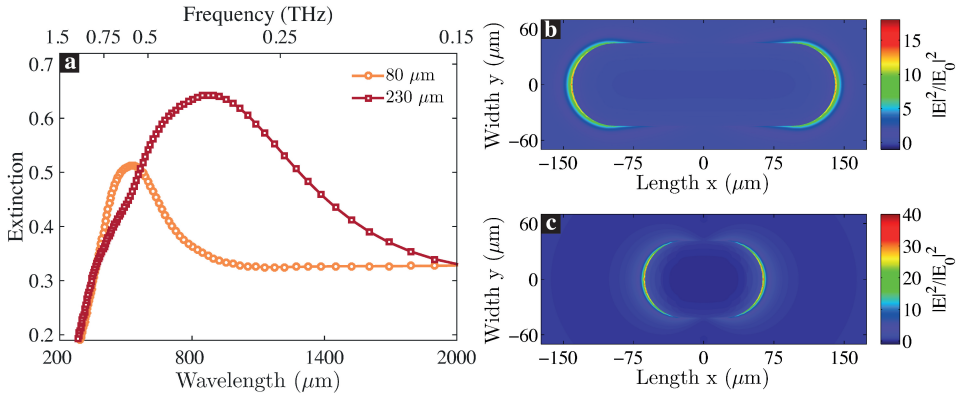

Figure 4.4: Finite difference in time domain simulations of photo-generated rods. (a) Simulated extinction for rods with effective dimensions 230 × 40 μm^2 and 80 × 40 μm^2. (b) simulated total field enhancement at the GaAs-air interface for a rod with an effective length of 230 μm. (c) same as (b) but for a rod with an effective length of 80 μm.

It is worthwhile to stress that the near-field enhancement in photo-generated antennas can be fully controlled in magnitude and spatial position by simply changing the illumination pattern defined with the SLM. By controlling the time delay between the optical pump and THz probe pulse, it is also possible to tune the magnitude of the enhancement. This approach could be exploited to enhance the sensitivity of locally functionalised surfaces or to realise spectroscopy of subwavelength structures by resonant enhancement of the local fields. Moreover, larger field enhancements could be achieved by coupling rods to form dimers [22] or by defining bowtie antennas with sharp tips and small gaps [25].

4.5 Conclusion

In conclusion, we have demonstrated the photo-generation of THz antennas by the structured illumination of a thin layer of undoped GaAs. This illumination is

accomplished with a spatial light modulator that allows the full optical control of resonant frequencies and local field enhancements. This approach can be extended to the photo-generation of metamaterials exhibiting magnetic resonances, i.e., split ring resonators[39], metasurfaces for active beam steering[40], and THz wave guiding structures[41].

Bibliography

[1] T. W. Ebbesen, H. J. Lezec, H. F. Ghaemi, T. Thio, and P. A. Wolff, *Extraordinary optical transmission through sub-wavelength hole arrays*, Nature **391**, 667 (1998).

[2] W. L. Barnes, A. Dereux, and T. W. Ebbesen, *Surface plasmon subwavelength optics*, Nature **424**, 824 (2003).

[3] J. A. Schuller, E. S. Barnard, W. Cai, Y. C. Jun, J. S. White, and M. L. Brongersma, *Plasmonics for extreme light concentration and manipulation*, Nat Mater **9**, 193 (2010).

[4] M. I. Stockman, M. F. Kling, U. Kleineberg, and F. Krausz, *Attosecond nanoplasmonic-field microscope*, Nat Photon **1**, 539 (2007).

[5] M. Aeschlimann, M. Bauer, D. Bayer, T. Brixner, F. J. Garcia de Abajo, W. Pfeiffer, M. Rohmer, C. Spindler, and F. Steeb, *Adaptive subwavelength control of nano-optical fields*, Nature **446**, 301 (2007).

[6] G. Volpe, S. Cherukulappurath, R. Juanola Parramon, G. Molina-Terriza, and R. Quidant, *Controlling the Optical Near Field of Nanoantennas with Spatial Phase-Shaped Beams*, Nano Letters **9**, 3608 (2009).

[7] B. Gjonaj, J. Aulbach, P. M. Johnson, A. P. Mosk, L. Kuipers, and A. Lagendijk, *Active spatial control of plasmonic fields*, Nat Photon **5**, 360 (2011).

[8] T. S. Kao, E. T. F. Rogers, J. Y. Ou, and N. I. Zheludev, *"Digitally" Addressable Focusing of Light into a Subwavelength Hot Spot*, Nano Letters **12**, 2728 (2012).

[9] M. Perner, P. Bost, U. Lemmer, G. von Plessen, J. Feldmann, U. Becker, M. Mennig, M. Schmitt, and H. Schmidt, *Optically Induced Damping of the Surface Plasmon Resonance in Gold Colloids*, Phys. Rev. Lett. **78**, 2192 (1997).

[10] S. Link and M. A. El-Sayed, *Spectral Properties and Relaxation Dynamics of Surface Plasmon Electronic Oscillations in Gold and Silver Nanodots and Nanorods*, The Journal of Physical Chemistry B **103**, 8410 (1999).

[11] N. Rotenberg, M. Betz, and H. M. van Driel, *Ultrafast control of grating-assisted light coupling to surface plasmons*, Opt. Lett. **33**, 2137 (2008).

[12] V. Halté, A. Benabbas, and J. Y. Bigot, *Surface plasmon dynamics in arrays of subwavelength holes: the role of optical interband transitions*, Optics Express **16**, 11611 (2008).

[13] K. F. MacDonald, Z. L. Samson, M. I. Stockman, and N. I. Zheludev, *Ultrafast active plasmonics*, Nat Photon **3**, 55 (2009).

[14] V. V. Temnov, K. A. Nelson, G. Armelles, A. Cebollada, T. Thomay, A. Leitenstorfer, and R. Bratschitsch, *Femtosecond surface plasmon interferometry*, Optics Express **17**, 8423 (2009).

[15] J. Dintinger, I. Robel, P. Kamat, C. Genet, and T. Ebbesen, *Terahertz All-Optical Molecule- Plasmon Modulation*, Advanced Materials **18**, 1645 (2006).

[16] V. Giannini, A. Berrier, S. A. Maier, J. Sánchez-Gil, and J. G. Rivas, *Scattering efficiency and near field enhancement of active semiconductor plasmonic antennas at terahertz frequencies*, Optics Express **18**, 2797 (2010).

[17] S. J. Allen, D. C. Tsui, and R. A. Logan, *Observation of the Two-Dimensional Plasmon in Silicon Inversion Layers*, Phys. Rev. Lett. **38**, 980 (1977).

[18] J. G. Rivas, M. Kuttge, P. H. Bolivar, H. Kurz, and J. A. Sánchez-Gil, *Propagation of Surface Plasmon Polaritons on Semiconductor Gratings*, Phys. Rev. Lett. **93**, 256804 (2004).

[19] J. G. Rivas, *Terahertz: The art of confinement*, Nat Photon **2**, 137 (2008).

[20] F. Neubrech, A. Pucci, T. W. Cornelius, S. Karim, A. García-Etxarri, and J. Aizpurua, *Resonant Plasmonic and Vibrational Coupling in a Tailored Nanoantenna for Infrared Detection*, Phys. Rev. Lett. **101**, 157403 (2008).

[21] J. Kundu, F. Le, P. Nordlander, and N. J. Halas, *Surface enhanced infrared absorption (SEIRA) spectroscopy on nanoshell aggregate substrates*, Chemical Physics Letters **452**, 115 (2008).

[22] M. Schnell, A. Garcia-Etxarri, A. J. Huber, K. Crozier, J. Aizpurua, and R. Hillenbrand, *Controlling the near-field oscillations of loaded plasmonic nanoantennas*, Nat Photon **3**, 287 (2009).

[23] R. Adato, A. A. Yanik, J. J. Amsden, D. L. Kaplan, F. G. Omenetto, M. K. Hong, S. Erramilli, and H. Altug, *Ultra-sensitive vibrational spectroscopy of protein monolayers with plasmonic nanoantenna arrays*, Proceedings of the National Academy of Sciences **106**, 19227 (2009).

[24] J. Gómez Rivas, M. Kuttge, H. Kurz, P. Haring Bolivar, and J. A. Sánchez-Gil, *Low-frequency active surface plasmon optics on semiconductors*, Applied Physics Letters **88**, 082106 (2006).

[25] A. Berrier, R. Ulbricht, M. Bonn, and J. G. Rivas, *Ultrafast active control of localized surface plasmon resonances in silicon bowtie antennas*, Optics Express **18**, 23226 (2010).

[26] H.-T. Chen, W. J. Padilla, J. M. O. Zide, A. C. Gossard, A. J. Taylor, and R. D. Averitt, *Active terahertz metamaterial devices*, Nature **444**, 597 (2006).

[27] H.-T. Chen, J. F. O'Hara, A. K. Azad, A. J. Taylor, R. D. Averitt, D. B. Shrekenhamer, and W. J. Padilla, *Experimental demonstration of frequency-agile terahertz metamaterials*, Nat Photon **2**, 295 (2008).

[28] T. Okada, K. Ooi, Y. Nakata, K. Fujita, K. Tanaka, and K. Tanaka, *Direct creation of a photoinduced metallic structure and its optical properties in the terahertz frequency region*, Optics Letters **35**, 1719 (2010).

[29] T. Okada and K. Tanaka, *Photo-designed terahertz devices*, Scientific Reports **1**, 121 (2011).

[30] I. Chatzakis, P. Tassin, L. Luo, N.-H. Shen, L. Zhang, J. Wang, T. Koschny, and C. M. Soukoulis, *One- and two-dimensional photo-imprinted diffraction gratings for manipulating terahertz waves*, Applied Physics Letters **103**, 043101 (2013).

[31] S. Busch, B. Scherger, M. Scheller, and M. Koch, *Optically controlled terahertz beam steering and imaging*, Opt. Lett. **37**, 1391 (2012).

[32] C. Rizza, A. Ciattoni, L. Columbo, M. Brambilla, and F. Prati, *Terahertz optically tunable dielectric metamaterials without microfabrication*, Optics Letters **38**, 1307 (2013).

[33] O. L. Muskens, V. Giannini, J. A. Sánchez-Gil, and J. Gómez Rivas, *Optical scattering resonances of single and coupled dimer plasmonic nanoantennas*, Optics Express **15**, 17736 (2007).

[34] M. C. Beard, G. M. Turner, and C. A. Schmuttenmaer, *Subpicosecond carrier dynamics in low-temperature grown GaAs as measured by time-resolved terahertz spectroscopy*, Journal of Applied Physics **90**, 5915 (2001).

[35] R. Ulbricht, E. Hendry, J. Shan, T. F. Heinz, and M. Bonn, *Carrier dynamics in semiconductors studied with time-resolved terahertz spectroscopy*, Rev. Mod. Phys. **83**, 543 (2011).

[36] L. Novotny, *Effective Wavelength Scaling for Optical Antennas*, Phys. Rev. Lett. **98**, 266802 (2007).

[37] E. Cubukcu and F. Capasso, *Optical nanorod antennas as dispersive one-dimensional Fabry-Pérot resonators for surface plasmons*, Applied Physics Letters **95**, 201101 (2009).

[38] V. Giannini, G. Vecchi, and J. Gómez Rivas, *Lighting Up Multipolar Surface Plasmon Polaritons by Collective Resonances in Arrays of Nanoantennas*, Phys. Rev. Lett. **105**, 266801 (2010).

[39] W. J. Padilla, A. J. Taylor, C. Highstrete, M. Lee, and R. D. Averitt, *Dynamical Electric and Magnetic Metamaterial Response at Terahertz Frequencies*, Phys. Rev. Lett. **96**, 107401 (2006).

[40] N. Yu, P. Genevet, M. A. Kats, F. Aieta, J.-P. Tetienne, F. Capasso, and Z. Gaburro, *Light Propagation with Phase Discontinuities: Generalized Laws of Reflection and Refraction*, Science **334**, 333 (2011).

[41] D. Gacemi, J. Mangeney, R. Colombelli, and A. Degiron, *Subwavelength metallic waveguides as a tool for extreme confinement of THz surface waves*, Scientific Reports **3**, 1369 (2013).

5

Active loaded plasmonic antennas at THz frequencies

We demonstrate experimentally the photo-generation of loaded dipole plasmonic antennas resonating at THz frequencies. This is achieved by the patterned optical illumination of a semiconductor surface using a spatial light modulator. Our experimental results indicate the existence of capacitive and inductive coupling of localised surface plasmon polaritons. By varying the load in the antenna gap we are able to switch between both coupling regimes. Furthermore, we determine experimentally the effective impedance of the antenna load and verify that this load can be effectively expressed as a LC resonance formed by a THz inductor and capacitor connected in a parallel circuit configuration. These findings are theoretically supported by full-electrodynamic calculations and by simple concepts of lumped circuit theory. Our results open new possibilities for the design of active THz circuits for optoelectronic devices.

5.1 Introduction

Optical antennas are crucial components in the design of future opto-electronic devices. Their main function is to convert free space electromagnetic radiation into

localised energy and vice versa.[1] Over the past decade plasmonic antennas have gained an exceptional popularity mainly because of their ability to confine visible and infrared radiation into lengths much smaller than the free-space wavelength.[2] Their prospective use in nanoscale electronic devices and detectors[3–5] as well as in systems that arbitrarily control wavefronts[6] has stimulated many research groups to thoroughly investigate their optical far-field properties and near field interactions with neighbouring elements. The configurations that have been proposed, inspired by their radiofrequency analogues, include among others, dipole[7], Yagi-Uda[8,9] and bow-tie[10–12] antennas whose purpose is to control directivity and bandwidth of visible and infrared waves. Furthermore, new antenna designs that exhibit more exotic properties have been proposed recently. These designs combine multiple resonating elements to achieve asymmetric Fano-like resonances[13–18] and Electromagnetically Induced Transparency[19,20] as well as metasurfaces that introduce gradual phase retardation along the propagation direction.[6,21,22]

In addition to these studies, a great emphasis has been given to the investigation of actively controlling the optical properties of plasmonic antennas. For this purpose dielectric and metallic loading of antenna elements has been considered and lumped circuit theory has been used to describe their resonant properties.[23–25] Near-field optical microscopy has been used to study the amplitude and phase of the fields in loaded nanoantennas verifying the validity of the lumped circuit theory at the nanoscale.[26] A similar design has been used recently to investigate the scattering and non-linear optical properties of such loaded antennas.[27,28] These works have laid a solid ground for actively controlling the properties of metallic antennas.

Semiconducting materials can be the ultimate candidate for actively controllable antennas, owing to their versatile nature. Their optical properties can be easily adjusted by simply controlling the density of free charge carriers, which leads also into a tuneability of their plasmonic behaviour from the infrared to the far-infrared (THz) regime.[29,30] Several studies have exploited the flexible nature of semiconductors in combination with metals to achieve tuneability of resonances in plasmonic and metamaterial structures.[31–34] Besides these studies, an all-optical control of plasmonic antennas made completely out of semiconductors has been recently demonstrated using a Spatial Light Modulator (SLM).[35]

In this chapter we present an experimental and theoretical study on photo-generated coupled plasmonic antennas, made out of semiconductors and functioning at THz frequencies. Furthermore, we explore the photo-excitation of loads at the gaps of these antennas that act as capacitors or inductors, and discuss the optical response of the antennas in terms of a simple electrical circuit model. In contrast to previous studies[26,27], using the information of the complex electric field provided by THz time domain spectroscopy, we are able to determine experimentally an effective impedance of the equivalent resonant LC circuit. Finally, we observe the existence of a capacitive and an inductive behaviour of localised surface plasmon polaritons formed at different frequencies.

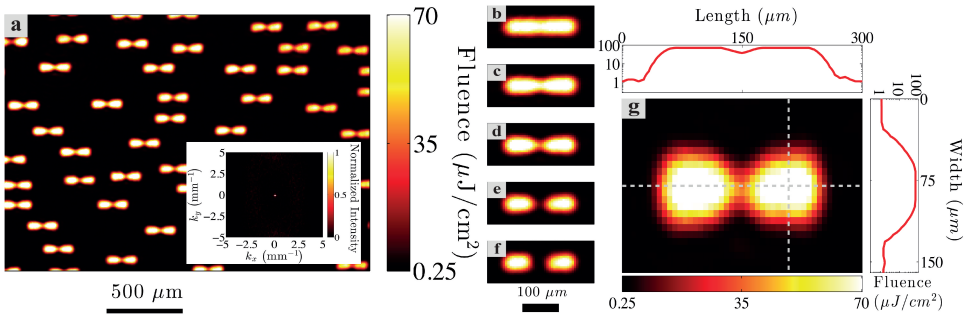

Figure 5.1: Photo-generated dimer THz antennas. (a) Camera image of the photo-generated loaded antennas with $W_b = 34.5$ μm. The average loaded antenna density is approximately 9.5 antennas/mm^2. The inset of (a) illustrates the 2D Fourier transform of the image. The colour bar of the inset shows the normalised intensity of the Fourier transform. (b) The two components of the coupled antennas are merged together forming a single linear antenna, (f) the coupled antennas are separated by a dielectric gap with length $L_g = 53 \pm 3$ μm, (c-e) intermediate cases where the two constituent components of the dimer antenna are bridged with a metallic-like connector. (g) shows a detailed analysis of (d). The colour scale and the vertical scale of the horizontal and vertical cuts illustrates the pump fluence.

5.2 Photo-excitation of active loaded antennas

Our experiments have been performed using the time-resolved THz Time Domain Spectrometer (TDS) described in Chapter 2. The excitation beam, which is spatially shaped by the SLM and projected on the sample, excites free electrons at the illuminated areas of a semiconductor surface in the form of coupled dimer antennas (Fig. 5.1). The sample used for the experiments is a 1 μm thick single crystalline GaAs bonded on to a 1 mm thick amorphous quartz substrate[35] (see Chapter 2). A pump-probe time delay of $\Delta\tau_{p-p} = 10$ ps was chosen for our experiments. This time delay is sufficiently short such that the spatial diffusion of the free carriers does not modify the dimensions of the photo-excited structures. In addition, the number of photo-excited carriers remains unchanged during the propagation of the THz pulse through the sample since its temporal envelope τ^{THz} is much shorter than the recombination time τ_r of the free charge carriers in GaAs ($\tau^{THz} \sim 1$ ps $\ll \tau_r$).

Figure 5.1(a) shows an image taken by a CCD camera at the sample position. The loaded antennas in all the experiments are arranged in a random configuration, which provides the advantage of suppressing any diffraction orders due to periodicity in the far field extinction spectrum. As can be appreciated from Fig. 5.1(a), the loaded antennas are well separated from their neighbouring antennas and therefore any near field coupling is negligible. The number of loaded antennas probed by the THz beam is approximately 45 (the average density of loaded antennas is ~ 9.5 antennas/mm^2 and the THz beam FWHM is 2.5 mm). The inset of Fig. 5.1(a) shows the 2D Fourier

transform of the image taken by the camera. The white dot at the center of the figure is the DC component of the Fourier transform, which can be associated to the zeroth order transmission.

Figure 5.1(b - f) shows images of the photo-excited structures taken by placing a CCD camera at the sample position. As can be appreciated in this figure the total length and width of the antennas is kept constant and only the intensity in the gap is varied. Figure 5.1(g) represents a more detailed analysis of Fig. 5.1(d). To have an estimate of the photo-induced antenna dimensions, we define an effective length and width by taking the size at which the pump intensity drops at half of its maximum (FWHM). This gives an effective length of $L = 195 \pm 3$ μm and width of $W = 56.5 \pm 3$ μm, where the uncertainties in the estimated values are associated with half of the pixel size of the CCD camera. The single linear antenna (Fig. 5.1(b)) is being split into two coupled antennas that are connected with a bridge that has constant effective length of $L_{\mathrm{g}} = 53 \pm 3$ μm and varying width W_{b} from 0 to 56.5 μm. Determining the bridge dimensions as well as the carrier concentration is critical. The bridge width is defined by summing the number of pixels in the gap area that have an intensity larger than the intensity at half the maximum (FWHM). Taking into consideration the pixel dimensions (6.45^2 μm^2) of the camera, this calculation will result into an effective area that has intensity higher than half the maximum. Subsequently, we define the effective bridge width, W_{b}, by dividing the calculated area by the gap length L_{g}. The values of W_{b} are reported in the insets of Fig. 5.2 for each case.

As it can be seen by the detailed analysis on one of the intermediate antennas (Fig. 5.1(g)), the maximum pump fluence is 70 μJ/cm^2. To understand the behaviour of our sample at these high pump fluences we have performed a pump-probe analysis. In this analysis we have measured the THz transmission through a homogeneously pumped GaAs layer. From this measurement we have determined the conductivity of the sample, which has a Drude-like behaviour with carrier density $N = 2 \times 10^{18}$ cm^{-3} and carrier mobility of $\mu = 0.15$ m^{2}V^{-1}s^{-1}. It is worthwhile to note that the finite contrast of the image projected by the SLM leads to a finite pump fluence in the regions defined as dark by the SLM. This fluence is lower than < 0.25 μJ/cm^2. A detailed analysis on a transmission measurement from a fully dark image, as defined by the SLM, showed that the conductivity of the sample follows a Drude-like behaviour with carrier density $N = 3 \times 10^{15}$ cm^{-3} and mobility $\mu = 0.7$ m^{2}V^{-1}s^{-1}.

5.3 Results

To determine the THz response of the dimer antennas, we excite them at normal incidence and we measure the THz transmission spectrum in the forward direction. Figure 5.2(a) illustrates the main experimental results of this chapter. This plot shows the far-field extinction spectra, defined as one minus the transmittance, as a function of wavelength (bottom axis) and frequency (top axis). The extinction is equal to the

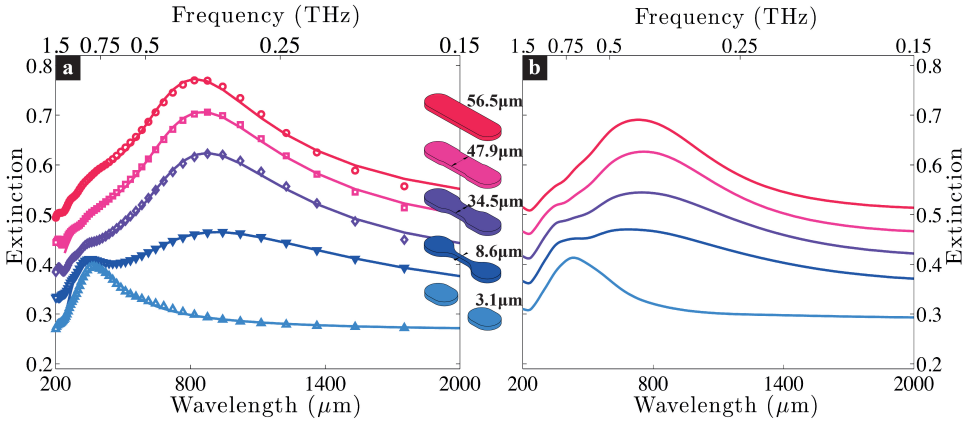

Figure 5.2: (a) Far field extinction measurements of randomly positioned loaded antennas with different bridge widths, as shown in the insets. The symbols are the experimental data and the solid curves represent bi-Lorentzian fits to the data. (b) Numerical FDTD calculations of far field extinction. The curves are displaced for clarity by a vertical shift of 0.2, 0.15, 0.1, 0.05 and 0 from red to blue respecively.

sum of scattering and absorption. The symbols are the experimental data points while the solid lines are bi-Lorentzian fits to the data. The main feature of this figure is a resonance at long wavelengths that redshifts from 850 μm to 1034 μm as we decrease the width of the bridge. This resonance corresponds to the fundamental resonant mode of the plasmonic antennas ($\lambda/2$ resonance), defined by an effective length that characterises the entire loaded antenna as described above. Moreover, as the bridge width decreases (i.e. bridge width of 8.6 μm) a second resonance appears at shorter wavelengths ($\lambda = 327$ μm, dark blue curve). This resonance is slightly blue-shifted with respect to the $\lambda/2$ resonance of the individual arms of the dimer antenna at $\lambda = 380$ μm (see light blue curve, which corresponds to $W_b = 3.1$ μm). The transition from the $\lambda/2$ resonance of the entire plasmonic antenna to the $\lambda/2$ resonance of the dimer antenna is controlled by the width of the gap linking the two components. As it is elucidated later in the chapter, this behaviour can be explained by a simple lumped circuit model. Figure 5.2(b) represents full 3D electrodynamic calculations of the far-field extinction using the Finite-Difference in the Time-Domain (FDTD Lumerical) method. The design of the structures used for the simulations incorporates a graded carrier concentration towards the edges of the antenna to mimic as close as possible the conditions of the experiment [35]. The simulations qualitatively reproduce the main far-field resonant features of the experimental observations. The small quantitative discrepancies between measurements and simulations can be attributed to the difficulty in defining from the CCD images the exact antenna geometry and dimensions for the simulations.

Although the spectra from both the experiment and simulations provide qualitative

information about the different modes of this system, it is important to investigate in more detail the interaction of the antenna with its load. Therefore, with use of the FDTD method we have numerically calculated the electric field enhancement $|\mathbf{E}(\mathbf{r},\omega)/\mathbf{E_0}(\mathbf{r},\omega)|$ and the surface charge $\sigma(\mathbf{r},\omega)$ distribution of one of the antennas ($W_\mathrm{b} = 8.6$ μm), at the short- and long- wavelength resonances. We should note that the obtained surface charge distributions have been smoothened, in order to remove the artificial (much lower) surface charges induced by the sequential shells of graded carrier concentrations. In Fig. 5.3(a) we show the electric field enhancement at $\lambda = 327$ μm, calculated at the middle of the antenna's height. The corresponding surface charge distribution $\sigma(\mathbf{r},\omega)$ is displayed in Fig. 5.3(b), where a dipole-dipole distribution typical of a bonding mode can be observed [36]. This mode, which is slightly blue-shifted with respect to the corresponding mode in the absence of a conducting bridge (see Fig. 5.2), indicates a capacitive load.

On the other hand, the presence of the photo-induced bridge allows for charge transfer along the entire antenna, which manifests itself by the appearance of a charge transfer mode at longer wavelengths [36]. In the particular case we are examining here, due to the small width of the bridge, this mode appears as a very broad, low-intensity mode. As the width of the bridge increases, charge transfer along the dimer is easier, and this mode becomes more intense and blue-shifts, eventually becoming the antenna $\lambda/2$ mode of a continuous rod, as can be seen in Fig. 5.2. For this mode the electric field (shown in Fig. 5.3(c) for $W_\mathrm{b} = 8.6$ μm and at $\lambda = 1030$ μm) is distributed along the entire antenna, which resembles a long dipole, as observed also in the surface charge distribution of Fig. 5.3(d). This field distribution indicates an inductive behaviour of the antenna load for this bridge width and wavelength. A non-negligible electric field intensity is also obtained around the bridge, associated with the presence of small surface charge densities of opposite sign at the crevices around the bridge.

An important parameter characterizing the resonant behaviour of these loaded antennas is their impedance. The impedance determines the interaction of a dipole antenna with its load. More precisely, it is defined as the ratio of the input voltage over the displacement current and it quantifies the total amount of energy dissipated or stored in the system. In terms of the electromagnetic properties, the impedance is defined as,

$$Z \equiv R - iX = \sqrt{\frac{\mu_0\ \mu}{\epsilon_0\ \epsilon}}, \tag{5.1}$$

where R is the resistance, X the reactance, $\mu_0 = 4\pi \times 10^{-7}$ H.m^{-1} and $\epsilon_0 = 8.85 \times 10^{-12}$ F.m^{-1} are the vacuum permeability and permittivity respectively. The impedance is a complex quantity with its real component being twice the average power dissipated in the system and its imaginary component related to the difference between the average inductive and capacitive energies stored in the system. [37]
The estimation of the complex impedance from the experimental data is difficult since it requires the complex transmitted and reflected signals. [38] However, in the simplest case, where there are no intrinsic magnetic fields due to circulating currents in the photo-generated antennas, we can assume that the magnetic permeability is equal to

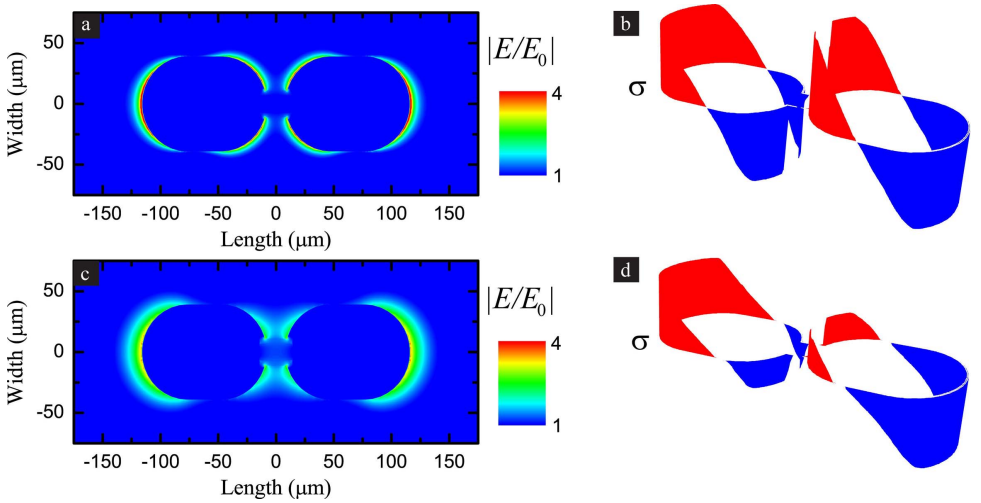

Figure 5.3: (a) Electric field enhancement ($|E/E_0|$) and (b) surface charge distribution (σ), calculated for an antenna with bridge width 8.6 μm, along an in-plane cross section of the antenna through its height centre, at $\lambda = 327$ μm. (c) Electric field enhancement ($|E/E_0|$) and (d) surface charge distribution of the same antenna at $\lambda = 1030$ μm. The red and blue areas in (b) and (d) denote positive and negative charges, respectively.

unity. Using this assumption the calculation of the impedance is simplified to only the knowledge of the complex transmitted signal.

In contrast to other works, where the optical properties and therefore the impedance of such loaded devices are estimated from the far field transmission intensity measurements and assuming a lumped circuit model[27], here we measure the complex transmission and thus extract these values directly from the experimental data, i.e. without any a-priori assumption. As it is demonstrated later in the text, the retrieved quantities are in a very good agreement with the far field resonant frequencies. In the following we discuss the retrieval of the effective load impedance, describing the random distribution of the antennas. This analysis is thus performed for the whole sample and not for single loaded antennas. In a conventional THz - TDS experiment the measured signal is the electric field as a function of time, which when Fourier transformed results in the complex electric field as a function of frequency, encompassing information about the amplitude and phase accumulated by the transmitted field. In order to retrieve the complex effective permittivity from transmission measurements we use the transfer matrix method.[39] In a sample that consists of a thin layer of material on a substrate (such as the one studied here), the wavelength is much longer than the thickness of the layer, $d \ll \lambda$. Therefore, the thin film approximation can be applied without any loss of generality. As shown in Chapter 2, in this approximation the complex effective

permittivity can be obtained from

$$\frac{\tilde{E}_{\mathrm{sam}}(\nu)}{\tilde{E}_{\mathrm{sub}}(\nu)} \simeq \frac{1+i\beta\sqrt{\tilde{\epsilon}_{\mathrm{eff}}}}{1+i\beta\ \frac{(1-\sqrt{\tilde{\epsilon}_{\mathrm{eff}}})(\sqrt{\tilde{\epsilon}_{\mathrm{eff}}}-\sqrt{\tilde{\epsilon}_{\mathrm{sub}}})}{1+\sqrt{\tilde{\epsilon}_{\mathrm{sub}}}}}, \tag{5.2}$$

where $\tilde{E}_{\mathrm{sam}}(\nu)$ and $\tilde{E}_{\mathrm{sub}}(\nu)$ are the THz electric fields transmitted through the sample and through the substrate respectively, $\beta = \omega d/c$, ω is the angular frequency, c is the speed of light in vacuum, $\tilde{\epsilon}_{\mathrm{sub}}$ is the complex permittivity of the substrate and $\tilde{\epsilon}_{\mathrm{eff}}$ is the complex effective permittivity of the photo-generated structures. The experimentally obtained effective permittivities for the loaded antennas are illustrated in Fig 5.4(a-b). The real component of the effective permittivity exhibits a resonant Drude - Lorentz like behaviour.[40] This response is characteristic for the motion of free charge carriers in the presence of an external driving force, which in our case is the THz electric field.[41] The frequency that corresponds to the transition through the $\tilde{\epsilon}_{\mathrm{eff}} = \epsilon_\infty$ dashed line indicates the dominant resonant frequency of the antennas, where ϵ_∞ is the contribution of the ion lattice and bound charges to the permittivity of GaAs. This is also depicted in the imaginary component of the effective permittivity, which exhibits a resonant behaviour. The increasing character of the imaginary component of the permittivity at low frequencies is due to the non-resonant absorption of THz radiation.

In order to define the effective permittivity of the load we divide the transmitted THz electric fields measured for the photo-generated loaded antennas (Fig. 5.1(a-d)) with the transmission measured from the dimer antenna (Fig. 5.1(e)) (see Eq. (5.2)). The obtained electric field corresponds to an effective response of the antenna load. This field is then normalised by the transmitted electric field obtained through a dark image as defined by the SLM. Consequently, the effective permittivity of the load is retrieved by using the transfer matrix method in the thin film approximation. By defining the permittivity of the load we calculate the effective load impedance ($Z_{\mathrm{eff}}^{\mathrm{load}}$) using Eq. (5.1). To calculate the impedance of the dimer, $Z_{\mathrm{eff}}^{\mathrm{dimer}}$, we use an approach similar to the one described above, in which we normalise the THz electric field transmitted through the photo-generated dimers with the electric field taken when there are no pumped structures (reference). As the measurement that defines the impedance of the dimer contains also the contribution from the free charge carriers that are being generated in the background due to the finite contrast of the SLM, it is necessary to correct for this background. Therefore, we subtract the impedance of a dark image, $Z_{\mathrm{eff}}^{\mathrm{dark}}$.

Figures 5.4(c-f) show the resistive (R_{eff}) component while Figures 5.4(g-j) show the reactive (X_{eff}) component of the effective impedance for different bridge widths, from $W_{\mathrm{b}} = 56.5$ μm (red) to $W_{\mathrm{b}} = 8.6$ μm (blue). As can be observed in the figure, the real and imaginary components of the impedance show a resonant feature. An interesting aspect of the load behaviour relies on the imaginary component of impedance (Figs. 5.4(g-j)) that undergoes a change of sign from negative at high frequencies to positive at low frequencies. This change of sign is directly related to a transition from an inductive to a capacitive behaviour of the effective load. It is also noteworthy to mention that

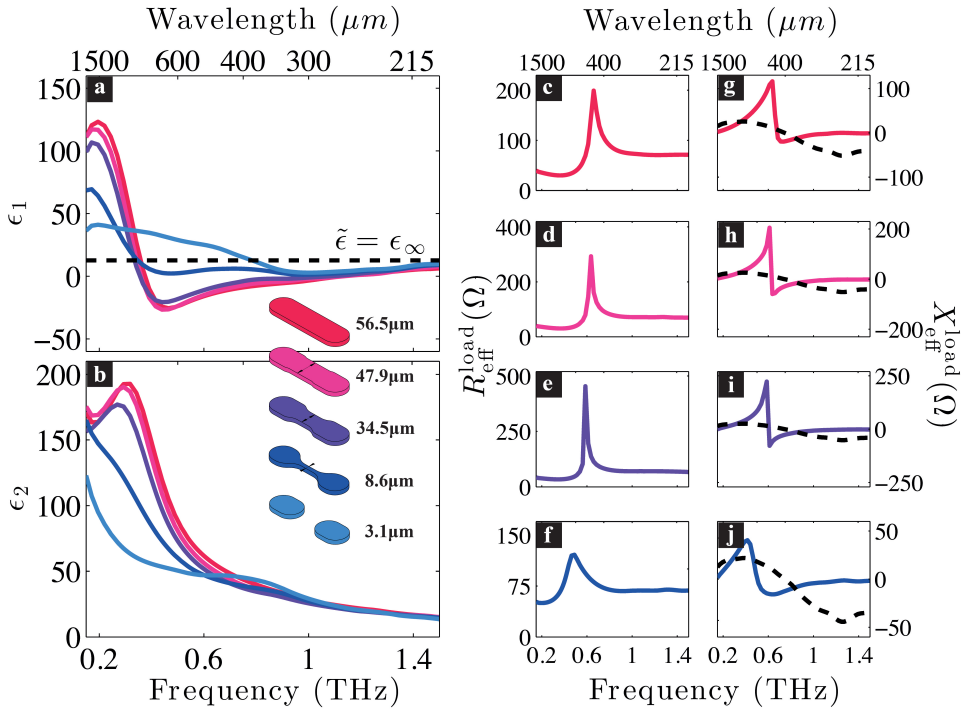

Figure 5.4: Detailed analysis of the transmitted signals through the photo-generated antennas. (a-b) Real (ϵ_1) and imaginary (ϵ_2) components of the effective permittivity for the randomly positioned loaded antennas as determined by the transfer matrix method in the thin film approximation. (c-f) Real component of the effective impedance (resistance, $R_{\text{eff}}^{\text{load}}$), (g-j) imaginary component of the effective impedance (reactance, $X_{\text{eff}}^{\text{load}}$). The black dashed lines illustrate the conjugate effective reactance of the randomly positioned dimer antennas ($X_{\text{eff}}^{*\text{dimer}}$).

we observe a redshift of the resonance as we decrease the bridge size. This means that the transition from inductive to capacitive behaviour also redshifts. From this analysis we observe experimentally that the behaviour of the effective impedance exhibits a similar behaviour to the impedance of a resonating LC circuit connected in parallel, as it was previously predicted [24,42], where L is the inductive load added by the conductive bridge and C the parallel capacitive load introduced by the dielectric gap. In addition to this behaviour, we show on the reactance plots the conjugate values of the reactance for the dimer, $X_{\text{eff}}^{*\ \text{dimer}}$ (dashed black line). The intersection points in the effective reactance plots (Figs. 5.4(g-j)) correspond to the impedance matching conditions between the antenna and its load ($X_{\text{eff}}^{\text{dimer}} = -X_{\text{eff}}^{\text{load}}$) . The frequencies for which these impedance matching conditions are fulfilled are shown in Fig. 5.5 as circles and triangles, and they are in excellent agreement with the positions of the

far-field resonances extracted from Fig. 5.2(a) and displayed as grey points in Fig. 5.5.

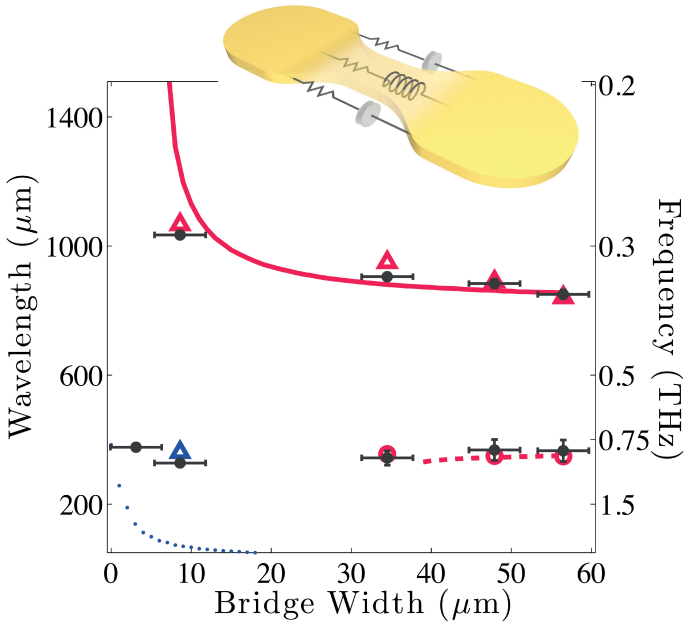

Figure 5.5: Lumped circuit model (lines) and experimental values (symbols) for varying bridge width. The blue dotted line corresponds to the capacitive mode for the $\lambda/2$ mode of the individual component of the dimer, while the red solid and dashed lines correspond to the $\lambda/2$ (long wavelengths) and $3\lambda/2$ (short wavelengths) inductive modes. The grey circles correspond to the resonant frequencies of the loaded antennas as obtained from a bi-Lorentzian fit to the far-field extinction measurements of Fig. 5.2. The blue/red triangles and red circles are the wavelength at which the effective dimer reactance equals to minus the effective load reactance of the measured sample as shown in Fig. 5.4 (g-j) ($X_{\mathrm{eff}}^{\mathrm{dimer}} = -X_{\mathrm{eff}}^{\mathrm{load}}$). The inset illustrates an artistic representation of the theoretical model that has been used for the calculations.

To qualitatively explain the spectral response of the loaded dimers we theoretically employ impedance matching conditions between the dimer antenna and its load. The impedance of a dimer antenna is similar to the response of an RF antenna [43] with the difference that its effective length is larger, due to its plasmonic nature and geometry. [44] The impedance of the load is defined by a parallel addition of the plasmonic bridge, $Z_b = iL_{\mathrm{g}}/\omega\epsilon_{\mathrm{b}}dW_{\mathrm{b}}$ and the dielectric gap, $Z_{\mathrm{g}} = iL_{\mathrm{g}}/\omega\epsilon_{\mathrm{g}}d(W - W_{\mathrm{b}})$ [42], where W and W_{b} are the experimentally obtained width of the gap and bridge respectively, d is the thickness of the sample and $\epsilon_{\mathrm{b,g}}$ are the permittivities of the bridge and gap calculated from the Drude model. For the calculation of the permittivities a carrier concentration of 10^{18} cm^{-3} for the bridge, 10^{16} cm^{-3} for the gap and 3×10^{15} cm^{-3} for the surrounding semiconductor were used. An artistic illustration of the model used for the calculation is shown in the inset of Fig. 5.5.

The results of this calculation display three distinct regimes as shown in Fig. 5.5. The first one, represented by the red solid line at long wavelengths, is the fundamental resonant mode, $\lambda/2$, of the entire loaded antenna and corresponds to an inductive behaviour. To confirm the inductive nature of the mode our FDTD simulations have shown that in contrast to the undoped GaAs layer, the magnetic field around the loaded antenna with bridge width 47.9 μm has a four-fold enhancement and decreases as the bridge width becomes smaller. This mode diverges for small bridge widths due to the high resistance and capacitance added by the dielectric surrounding the bridge. Additionally, at short wavelengths we observe two modes. The first one for large bridge widths (red dashed line) corresponds to the higher order resonant mode, $3\lambda/2$, of the entire resonant antenna while the second one for small bridge sizes (blue dotted line) is related to the $\lambda/2$ resonant mode of the individual components of the dimer. The above theoretical calculations are in a very good agreement with the experimental data shown by grey points in Fig. 5.5.

5.4 Conclusions

In summary, we have demonstrated the all-optical generation of loaded plasmonic antennas for THz radiation on a flat GaAs layer using a spatial light modulator. The proposed concept allows full control over the antenna properties and provides flexibility on defining the applied load. Furthermore, we are able to retrieve experimentally, for the first time, the effective impedance on the load and verify the validity of the lumped circuit theory in semiconducting systems by recovering a resonant behaviour that is analogous to an LC circuit. We have shown the existence of a capacitive and an inductive behaviour of localised surface plasmon polaritons at THz frequencies. Our results indicate that the transition between these two regimes can be actively controlled by tuning the design of the loaded antennas, which is controlled by the optical illumination pattern on a flat GaAs layer. The demonstration of active semiconductor lumped circuits and the possibility of optically generating these circuits will open new venues for fundamental research and new technologies. Examples of these are the ultrafast dynamics of photo-generated circuits [45] or their applications for resonant THz sensing and spectroscopy [46,47] on flat layers which are optically structured.

Bibliography

[1] P. Bharadwaj, B. Deutsch, and L. Novotny, *Optical Antennas*, Adv. Opt. Photon. **1**, 438 (2009).

[2] P. Mühlschlegel, H.-J. Eisler, O. Martin, B. Hecht, and D. Pohl, *Resonant optical antennas*, Science **308**, 1607 (2005).

[3] P. Biagioni, J.-S. Huang, and B. Hecht, *Nanoantennas for visible and infrared radiation*, Reports on Progress in Physics **75**, 024402 (2012).

[4] F. Neubrech, A. Pucci, T. W. Cornelius, S. Karim, A. García-Etxarri, and J. Aizpurua, *Resonant Plasmonic and Vibrational Coupling in a Tailored Nanoantenna for Infrared Detection*, Phys. Rev. Lett. **101**, 157403 (2008).

[5] M. W. Knight, H. Sobhani, P. Nordlander, and N. J. Halas, *Photodetection with Active Optical Antennas*, Science **332**, 702 (2011).

[6] N. Yu, P. Genevet, M. A. Kats, F. Aieta, J.-P. Tetienne, F. Capasso, and Z. Gaburro, *Light Propagation with Phase Discontinuities: Generalized Laws of Reflection and Refraction*, Science **334**, 333 (2011).

[7] P. Ghenuche, S. Cherukulappurath, T. H. Taminiau, N. F. van Hulst, and R. Quidant, *Spectroscopic Mode Mapping of Resonant Plasmon Nanoantennas*, Phys. Rev. Lett. **101**, 116805 (2008).

[8] A. F. Koenderink, *Plasmon Nanoparticle Array Waveguides for Single Photon and Single Plasmon Sources*, Nano Letters **9**, 4228 (2009).

[9] A. G. Curto, G. Volpe, T. H. Taminiau, M. P. Kreuzer, R. Quidant, and N. F. van Hulst, *Unidirectional Emission of a Quantum Dot Coupled to a Nanoantenna*, Science **329**, 930 (2010).

[10] F. González and G. Boreman, *Comparison of dipole, bowtie, spiral and log-periodic IR antennas*, Infrared Physics & Technology **46**, 418 (2005).

[11] H. Fischer and O. J. F. Martin, *Engineering the optical response ofplasmonic nanoantennas*, Opt. Express **16**, 9144 (2008).

[12] H. Guo, T. P. Meyrath, T. Zentgraf, N. Liu, L. Fu, H. Schweizer, and H. Giessen, *Optical resonances of bowtie slot antennas and their geometry and material dependence*, Opt. Express **16**, 7756 (2008).

[13] A. M. Funston, C. Novo, T. J. Davis, and P. Mulvaney, *Plasmon Coupling of Gold Nanorods at Short Distances and in Different Geometries*, Nano Letters **9**, 1651 (2009).

[14] B. Luk'yanchuk, N. I. Zheludev, S. A. Maier, N. J. Halas, P. Nordlander, H. Giessen, and C. T. Chong, *The Fano resonance in plasmonic nanostructures and metamaterials*, Nature Materials **9**, 707 (2010).

[15] A. E. Miroshnichenko, S. Flach, and Y. S. Kivshar, *Fano resonances in nanoscale structures*, Rev. Mod. Phys. **82**, 2257 (2010).

[16] Y. Francescato, V. Giannini, and S. A. Maier, *Plasmonic Systems Unveiled by Fano Resonances*, ACS Nano **6**, 1830 (2012).

[17] M. Abb, Y. Wang, P. Albella, C. H. de Groot, J. Aizpurua, and O. L. Muskens, *Interference, Coupling, and Nonlinear Control of High-Order Modes in Single Asymmetric Nanoantennas*, ACS Nano **6**, 6462 (2012).

[18] A. Lovera, B. Gallinet, P. Nordlander, and O. J. F. Martin, *Mechanisms of Fano Resonances in Coupled Plasmonic Systems*, ACS Nano **7**, 4527 (2013).

[19] N. Papasimakis, V. A. Fedotov, N. I. Zheludev, and S. L. Prosvirnin, *Metamaterial Analog of Electromagnetically Induced Transparency*, Phys. Rev. Lett. **101**, 253903 (2008).

[20] N. Liu, L. Langguth, T. Weiss, J. Kästel, M. Fleischhauer, T. Pfau, and H. Giessen, *Plasmonic analogue of electromagnetically induced transparency at the Drude damping limit*, Nature Materials **8**, 758 (2009).

[21] S. Sun, Q. He, S. Xiao, Q. Xu, X. Li, and L. Zhou, *Gradient-index meta-surfaces as a bridge linking propagating waves and surface waves*, Nature materials **11**, 426 (2012).

[22] P. Genevet, N. Yu, F. Aieta, J. Lin, M. A. Kats, R. Blanchard, M. O. Scully, Z. Gaburro, and F. Capasso, *Ultra-thin plasmonic optical vortex plate based on phase discontinuities*, Applied Physics Letters **100**, (2012).

[23] N. Engheta, A. Salandrino, and A. Alù, *Circuit Elements at Optical Frequencies: Nanoinductors, Nanocapacitors, and Nanoresistors*, Phys. Rev. Lett. **95**, 095504 (2005).

[24] A. Alù and N. Engheta, *Input Impedance, Nanocircuit Loading, and Radiation Tuning of Optical Nanoantennas*, Phys. Rev. Lett. **101**, 043901 (2008).

[25] N. Liu, F. Wen, Y. Zhao, Y. Wang, P. Nordlander, N. J. Halas, and A. Alú, *Individual Nanoantennas Loaded with Three-Dimensional Optical Nanocircuits*, Nano Letters **13**, 142 (2013).

[26] M. Schnell, A. Garcia-Etxarri, A. Huber, K. Crozier, J. Aizpurua, and R. Hillenbrand, *Controlling the near-field oscillations of loaded plasmonic nanoantennas*, Nature Photonics **3**, 287 (2009).

[27] Y. Wang, M. Abb, S. A. Boden, J. Aizpurua, C. H. de Groot, and O. L. Muskens, *Ultrafast Nonlinear Control of Progressively Loaded, Single Plasmonic Nanoantennas Fabricated Using Helium Ion Milling*, Nano Letters **13**, 5647 (2013).

[28] M. Abb, P. Albella, J. Aizpurua, and O. L. Muskens, *All-Optical Control of a Single Plasmonic Nanoantenna–ITO Hybrid*, Nano Letters **11**, 2457 (2011).

[29] J. Gómez-Rivas, M. Kuttge, P. H. Bolivar, H. Kurz, and J. A. Sánchez-Gil, *Propagation of surface plasmon polaritons on semiconductor gratings*, Phys. Rev. Lett. **93**, 256804 (2004).

[30] A. J. Huber, F. Keilmann, J. Wittborn, J. Aizpurua, and R. Hillenbrand, *Terahertz Near-Field Nanoscopy of Mobile Carriers in Single Semiconductor Nanodevices*, Nano Letters **8**, 3766 (2008).

[31] H.-T. Chen, W. J. Padilla, J. M. O. Zide, A. C. Gossard, A. J. Taylor, and R. D. Averitt, *Active terahertz metamaterial devices*, Nature **444**, 597 (2006).

[32] E. A. Shaner, J. G. Cederberg, and D. Wasserman, *Electrically tunable extraordinary optical transmission gratings*, Applied Physics Letters **91**, 181110 (2007).

[33] H.-T. Chen, H. Lu, A. K. Azad, R. D. Averitt, A. C. Gossard, S. A. Trugman, J. F. O'Hara, and A. J. Taylor, *Electronic control of extraordinary terahertz transmission through subwavelength metal hole arrays*, Opt. Express **16**, 7641 (2008).

[34] J. Gu, R. Singh, X. Liu, X. Zhang, Y. Ma, S. Zhang, S. A. Maier, Z. Tian, A. K. Azad, H.-T. Chen, A. J. Taylor, J. Han, and W. Zhang, *Active control of electromagnetically induced transparency analogue in terahertz metamaterials*, Nature Communications **3**, 1151 (2012).

[35] G. Georgiou, H. Tyagi, P. Mulder, G. Bauhuis, J. Schermer, and J. Gómez-Rivas, *Photo-generated THz antennas*, Scientific Reports **4** (2014).

[36] O. Pérez-González, N. Zabala, A. G. Borisov, N. J. Halas, P. Nordlander, and J. Aizpurua, *Optical Spectroscopy of Conductive Junctions in Plasmonic Cavities*, Nano Letters **10**, 3090 (2010).

[37] R. B. Adler, L. J. Chu, and R. M. Fano, *Electromagnetic energy transmission and radiation*, Wiley, 1960.

[38] D. R. Smith, D. C. Vier, T. Koschny, and C. M. Soukoulis, *Electromagnetic parameter retrieval from inhomogeneous metamaterials*, Phys. Rev. E **71**, 036617 (2005).

[39] Y. Pochi, *Optical Waves in Layered Media*, John Wiley & Sons, 2005.

[40] R. Ulbricht, E. Hendry, J. Shan, T. F. Heinz, and M. Bonn, *Carrier dynamics in semiconductors studied with time-resolved terahertz spectroscopy*, Rev. Mod. Phys. **83**, 543 (2011).

[41] A. Agrawal, Z. V. Vardeny, and A. Nahata, *Engineering the dielectric function of plasmonic lattices*, Opt. Express **16**, 9601 (2008).

[42] A. Alù and N. Engheta, *Tuning the scattering response of optical nanoantennas with nanocircuit loads*, Nature photonics **2**, 307 (2008).

[43] C. A. Balanis, *Antenna theory: analysis and design*, John Wiley & Sons, 2012.

[44] L. Novotny, *Effective Wavelength Scaling for Optical Antennas*, Phys. Rev. Lett. **98**, 266802 (2007).

[45] H. K. Tyagi and J. Gómez-Rivas, *Photo-generated THz plasmonic waveguides*, Journal of Optics **16**, 094011 (2014).

[46] A. Berrier, M. C. Schaafsma, G. Nonglaton, J. Bergquist, and J. Gómez-Rivas, *Selective detection of bacterial layers with terahertz plasmonic antennas*, Biomed. Opt. Express **3**, 2937 (2012).

[47] S. J. Park, J. T. Hong, S. J. Choi, H. S. Kim, W. K. Park, S. T. Han, J. Y. Park, S. Lee, D. S. Kim, and Y. H. Ahn, *Detection of microorganisms using terahertz metamaterials*, Sci. Rep. **4** (2014).

6

Terahertz wireless communications using photo-generated metasurfaces

The efficient steering of THz waves is crucial for future terabit-per-second (Tbps) wireless communications at the THz band. Terahertz beams are inherently very directional and therefore the alignment between transmitter and receiver is very critical. In this valorization chapter we propose active beam steering of terahertz waves using photo-excited metasurfaces. We further demonstrate experimentally a proof-of-principle of this application by showing selective beam steering of THz waves using a photo-excited blazed grating metasurface.

6.1 Broad-, broader-, broadest-band wireless communications

The necessity of exchanging vast amount of information fast and efficiently, has established internet an integral part of our everyday communications, such as social

media, entertainment, education, and online trade. This necessity has been largely supported by desktop and laptop computers and lately by smaller portable devices.

The advent of "smart" portable electronic devices, such as smartphones, tablets, watches and glasses, has been accompanied by an exploding increase of the data generated on a daily basis. This increase is directly connected to the versatile nature of these devices which are equipped with a variety of sensors and instruments that can generate, upload and share data at any instance. With the amount of smart devices and data shared increasing, the demands for ultra-broadband wireless internet access is becoming a reality. Based on the annual report of ETNO* [1], it is astonishing to note that while new subscribers for fixed-wired communications (DSL) are increasing at a constant rate, new subscribers for broadband wireless communications, such as 3G and 4G, are increasing at significantly higher rates. The increased demand for broadband wireless communications is by no means a great surprise, since these emerging technologies are able for the first time to compete on equal terms against their fixed-wired analogues, especially in rural areas, such as small islands, where the deployment of cables for wired communications is less likely to be realised.

Although current wireless technologies (Wi-Fi and 4G) can support very fast and reliable broadband communications, one of the greatest challenges of these technologies is to catch up with the demands for higher data transfer rates. These demands are directly related with the tendency of users to shift to high-volume data communications, such as high definition (HD) video, audio and imaging that will require almost instantaneous data transfers. Based on the above trends, it has been predicted that wireless communications with data rates up to 1 Tbps† will become a necessity by the year 2020 [2,3].

One of the main limitations of the current wireless technology is the scarcity of the available bandwidth, which is the foundation of ultrafast communications. Technologies such as Wi-Fi and 4G operate at carrier frequencies around 5 GHz and 1.8 GHz respectively with a bandwidth of just few tens of MHz. This limited bandwidth is unable to meet consumers demands for Tbps connections [4], even with advanced multi-antenna schemes such as MIMO‡. A very promising technology that could potentially support high data rates is the WiGig, operating at millimeter waves with frequencies around 60 GHz and bandwidths up to 7 GHz. Even though these bandwidths can support data rates up to 10 Gbps, they are not broad enough for Tbps links, since the useful bandwidth is 7 GHz imposing therefore an upper boundary for this technology.

Most of the limitations for ultra-broad bandwidths originate from the radio frequencies that are currently available for wireless communications. It is worthwhile to point out that most of the frequencies of the spectrum up to 300 GHz are already allocated for various applications such as satellite navigation, radio-astronomy and research, leaving therefore no room for broadband communications. On the contrary, frequencies above 300 GHz (THz band), have not been allocated yet to any application

*European Telecommunications Network Operators' Association

†The equivalent of transferring a 7 hour Blu-Ray HD-video (125 GB) in 1 second

‡MIMO: Multiple-Input Multiple-Output is a technology based on a multipath propagation of a signal emitted from multiple antennas

Box 6.1 ▶ Big data

The emergence of "smart" technologies has brought along a great challenge: big data. It is remarkable to note that more data have been created within the last two years than ever before, while 1.7 MB of new data are created by us every second, more than 300 hours of video are uploaded every hour and in 2015 alone a breathtaking amount of 1 trillion photos has been shared online. The majority of these data are created and shared by "smart" mobile phones who are currently taking over the market with up to now 2.6 billion subscriptions globally. This number is expected to triple (6.1 billion) in the next five years due to markets that are currently under development, such as in Asia and Africa. In addition, it is expected that by 2020 over 50 billion "smart" devices will be connected online, while almost a third of all the available data will be passing through the cloud [5–7].
Is the current technology ready to support these demands?

and can be therefore used for Tbps communications.

6.1.1 Terahertz wireless communications

Communications at THz frequencies have the capacity of supporting the desired links for Tbps data rates, since the THz band can have intrinsically 10-100 times larger bandwidth than existing state-of-art technologies. Although the development of THz wireless communications is still at a very early stage, with the latest advances in the fields of THz electronics and optoelectronics it is reassuring to witness an accelerating interest towards realising the first prototypes for Tbps links.

These developments are further encouraged by the growing interest of hi-tech companies, such as Fujitsu and IBM that aim on promoting these technologies for broadcasting, medical and general consumer applications. Some of the suggested applications include among others the use of THz wireless communications for the new generations of mobile networks (5G or 6G), high definition video or holographic broadcasting for home use or medical applications, short range secure military communications and wireless local area networks (WLAN) for houses or offices (see Fig. 6.1).

In addition, Tbps links can be used for wireless communications at the microscale and nanoscale. Based on the proposed applications, processors in multi-CPU computers can communicate wirelessly [8] enabling therefore the design of compact systems that can be also energy efficient (green) since a significant amount of interconnects responsible for large energy losses would be redundant. Moreover, nanosensors introduced to the skin or blood of humans can monitor and send to "smart devices" vital informations about the health of certain groups of people, such as hospital patients, athletes, astronauts etc.

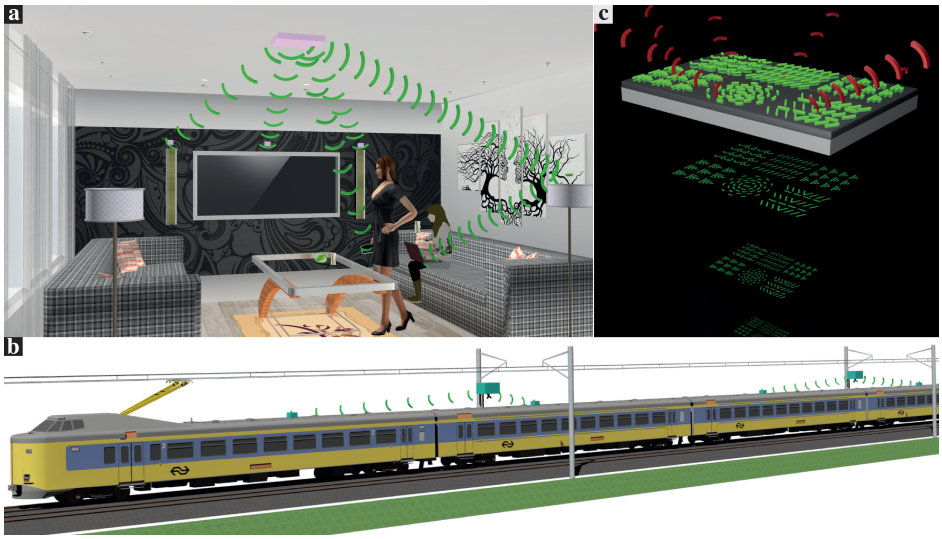

Figure 6.1: Artistic illustration of THz wireless communications. The left image (a) shows a wireless home network (T-WLAN), in which a THz transceiver attached to the ceiling of a living room can send and receive THz signals to a variety of smart devices. The bottom panel (b) illustrates a THz public network used in trains. The transceivers are located on the side of train tracks and are connected with a fiber cable to a central network. The passengers of a passing-by train can connect to these transceivers through Tbps links. (c) Conceptual design of a THz transceiver in which there are photo-generated six different metasurface patterns that steer the THz radiation emitted by a THz emitter (light gray area). Image by *Ricardo Struik*, FOM Institute AMOLF.

6.1.2 Fundamental concepts

Prior to the development of any technology for wireless communications at the THz band some fundamental concepts should be addressed.
The most important aspect concerns the carrier frequency and bandwidth; parameters that are generally very sensitive to external factors such as weather conditions. The propagation of THz waves is largely affected by the absorption and scattering due to rain, snow and fog. Computer simulations considering the above effects demonstrate that the frequency windows 0.41, 0.49, 0.67 and 0.85 THz with bandwidths between 50 - 150 GHz can have the highest transmission, while the propagation length at the above frequencies is between several meters to few tens of meters [9,10]. These studies also show that the attenuation of THz waves propagating at the micro- and nano-scale is not significant and therefore the whole THz band can be used for communications.

Another important factor that can affect the communication between a transmitter and a receiver is the directionality of THz waves, which is also the main subject of this chapter. Waves in the THz band are inherently more directional than their radio-frequency analogues since there is less diffraction by the environment. As shown by

the Friis formula the power received by an antenna P_r is inversely proportional to the wavelength squared, i.e.,

$$P_\mathrm{r} = P_\mathrm{in} \frac{A_\mathrm{r} A_\mathrm{t}}{r^2 \lambda^2} \; F_\mathrm{r}(\theta_\mathrm{r}, \phi_\mathrm{r}) \; F_\mathrm{t}(\theta_\mathrm{t}, \phi_\mathrm{t}) \; \tau \varepsilon_\mathrm{p}, \tag{6.1}$$

where P_in is the input power to the transmitting antenna, A_r and A_t are the effective areas of the receiving and transmitting antennas respectively, r is the separation between the two antennas, λ is the wavelength of the transmitted wave, τ is the path transmission factor and F_r, F_t ε_p are beam parameters such as shape and polarisation.

From the above equation (Eq. 6.1) it is clear that the received power is larger for shorter wavelengths since they are less diffracted and therefore more directional. A very important implication of this directionality is that both transmitter and receiver need to be in a "line-of-sight" without any obstacles in between that can perturb the transmission. This can be a crucial limitation for the implementation of THz communications, since otherwise Tbps links cannot be established by portable devices on the move, such as mobile phones and laptops.

6.1.3 Terahertz transceivers with photo-generated metasurfaces

The alignment between transmitter and receiver can be tuned by arrays of antennas known as metasurfaces that can control the wavefront of THz waves and therefore the directionality, as it will be elucidated later in the chapter. In this way both antennas can "decide" the most optimum propagation path with the highest bandwidth.

In this valorisation chapter we propose the use of photo-generated metasurfaces on the surface of semiconducting THz transceivers, such as Gallium Nitride (GaN), Indium Phosphide (InP) and quantum cascade lasers (QCL). Based on the projection technique described in Chapter 2 arrays of metasurfaces can be projected on the transceivers allowing therefore highly directional THz beams as well as the connection of multiple users with the same transmitter and the implementation of multi-band MIMO schemes. By actively exciting metasurface arrays on the surfaces of the transceivers it is possible to tune the directionality of THz waves on a picosecond time scale.

Metasurfaces are planar optical components, which contain arrays of subwavelength plasmonic scatterers of varying shape, resonant frequencies and orientation. The use of plasmonic scatterers for the implementation of the proposed application is of great importance since plasmonic scatterers can have dimensions smaller than THz wavelengths and can enable the design of compact THz transceivers.

Terahertz waves scattered by each subwavelength structure will acquire a different phase and the far-field interference of these scattered waves gives rise to beaming in defined directions or to more complex wave front shapes. The directional beam steering by metasurfaces has been described in the context of the generalised laws of refraction and reflection in which a constant gradient of phase discontinuity along the interface is introduced by the subwavelength scatterers[11,12]. Although, this concept shares some similarities with antenna phased arrays in which antenna elements emit radiation

with a defined phase relation relative to other elements to achieve beaming [13,14], the generalised laws of reflection and refraction are a simple way of describing complicated wave propagation through interfaces using ray optics. The validity of these laws is further supported by a more sophisticated model based on wave diffraction by Larouche and Smith [15]. The possibility of controlling the direction, shape and polarisation of electromagnetic waves has motivated an intensive research especially at visible and near-infrared frequencies [16–27].

In this chapter we demonstrate a proof-of-principle for active THz beam steering using the simplest metasurface, i.e. a planar photo-generated blazed grating. This is achieved on a thin gallium arsenide (GaAs) layer* by using a graded illumination profile over the period of the grating using the SLM (see Chapter 2). This graded illumination produces a spatially dependent free-carrier density along the surface of the layer that increases linearly with the illumination fluence. An incident THz pulse, time-delayed with respect to the illuminated blazed grating, experiences a phase delay that depends on the free-carrier density and it is therefore selectively beamed to the $+1$ or -1 diffraction orders of the grating.

6.2 Terahertz beaming

Prior to the experimental results we numerically calculate the optical properties of the optically thin GaAs layer for different excitation powers as well as the phase delay experienced by the THz wave travelling through the layer.

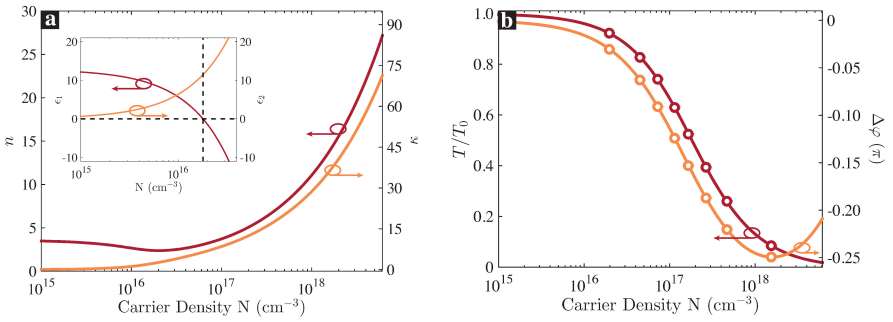

Figure 6.2: (a) Real (red) and imaginary (orange) components of the refractive index of GaAs at $\nu = 1$ THz as a function of the carrier density, N, calculated using the Drude model. The inset shows the complex permittivity ($\tilde{\epsilon} = \epsilon_1 + i\epsilon_2$) as a function of N. (b) Transmission amplitude at $\nu = 1$ THz through a GaAs layer with a 1 μm thickness calculated as a function of the carrier density and normalized to the transmission through an intrinsic GaAs layer (red circles and red curve). The orange circles and orange curve correspond to the phase difference between the transmission through the GaAs layer with carrier density N and the transmission through a GaAs layer with intrinsic carrier density.

*The thin GaAs layer can substitute the THz emitter.

Figure 6.2(a) shows the complex refractive index of GaAs as a function of the carrier density calculated using the Drude model at $\nu = 1$ THz. For a carrier concentration of $N = 10^{15}$ cm^{-3} the layer has a dielectric behaviour with refractive index $n = 3.5$ and extinction coefficient $\kappa \approx 0$. The dielectric nature of the GaAs is also illustrated by the positive value of the real part of the permittivity ϵ_1 displayed in the inset of Fig. 6.2(a). A slightly higher carrier density, $N = 1.8 \times 10^{16}$ cm^{-3}, renders the behaviour of the semiconducting layer metallic with refractive index $n = 2.4$, which corresponds to negative values of the real part of the permittivity ($\epsilon_1 < 0$). For even higher carrier concentrations the refractive index increases rapidly following Drude-like behaviour, while the extinction coefficient, κ, increases monotonously for increasing carrier concentration.

Using the transfer matrix method [28,29] and the complex refractive index of GaAs as it is obtained from the Drude model (see Chapter 2 and 3), we can determine the amplitude and phase of THz waves transmitted through the GaAs layer as a function of the carrier density. For these calculations we consider a three layer system surrounded by air, as in the sample described in Chapter 2. These layers are the SiO_2 substrate, the mercapto-ester based bonding polymer with 40 μm thickness and the 1 μm thick layer of GaAs. The calculated normalised transmission amplitude T/T_0 and phase shift $\Delta\varphi = \varphi - \varphi_0$ at $\nu = 1$ THz are shown in Fig. 6.2(b), while the reference values (T_0 and φ_0) used to normalise the transmission and phase are obtained by using the same three layers but with a carrier concentration that corresponds to an intrinsically doped GaAs ($n = 3.56$, $\kappa \approx 0$).

The transmission amplitude of the THz field through the layer decreases with increasing carrier concentration N. This is attributed to an increased reflection and absorption as the layer becomes metallic ($N > 1.8 \times 10^{16}$ cm^{-3}), while a maximum phase shift of -0.25π is obtained for a carrier density of $N = 1.5 \times 10^{18}$ cm^{-3}. This behaviour is caused by the interplay of two effects [30]. First, the change of the refractive index along the surface of the photo-excited semiconductor will cause a gradual variation of the optical path length, which will therefore result into a phase shift of the propagating wave,

$$\Delta\varphi = \frac{2\pi\nu}{c}\,\delta L, \tag{6.2}$$

where c denotes the speed of light in vacuum and δL is the variation of the optical path length. The second contribution to the phase shift arises from the transmission at the interfaces and it is described by the Fresnel coefficients. In particular, besides the variation in the optical path length, the absorptive nature of the optically illuminated semiconductor introduces an extra phase shift that adds up to the total phase shift of the transmitted THz wave from one medium to the next, as shown in more detail in Appendix C.

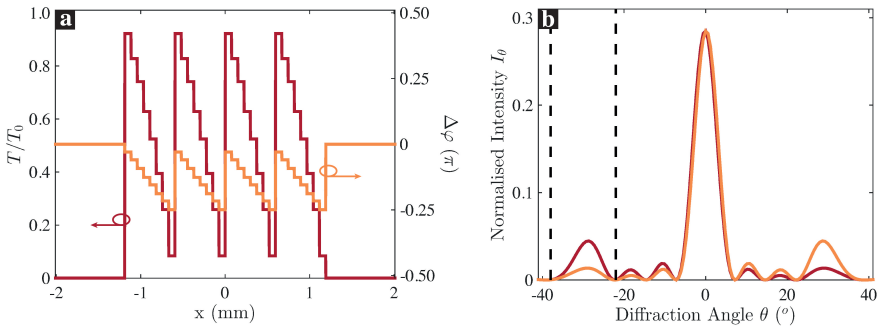

Figure 6.3: (a) Blazed grating with 4 grating periods and grating constant $\Gamma = 600$ μm. One grating period consists out of 8 carrier densities as indicated by the red and orange circles in Fig. 6.3(b). The carrier density, N, decreases from right to left in each period. (b) Calculated far-field intensity pattern at $\nu = 1$ THz of the blazed grating with carrier density that decreases from right to left (red) and from left to right (orange) in each period. The intensity is normalized with the transmission through a fully transparent window with the dimensions of 4 grating periods and zero transmission outside. The vertical dashed lines indicate the angular range of interest for the experiment.

6.3 Experimental results

6.3.1 Photo-generated blazed gratings

In order to demonstrate selective THz beam steering we photo-excite a blazed grating metasurface on the surface of the sample described above using the method introduced in Chapter 2. To define a linear phase gradient along the surface of the semiconductor we use the normalised transmission amplitude and phase shift shown in Fig. 6.2(b). Consequently, each grating period is subdivided into 8 steps with increasing carrier density that result into 8 equidistant phase steps defining a constant phase gradient. The 8 carrier densities chosen for our experiments are indicated by circles in Fig. 6.2(b).

The calculated complex transmission function of the designed blazed grating with a grating constant $\Gamma = 600$ μm is shown in Fig. 6.3(a). For these calculations we have chosen four grating periods since the THz beam used for our experiments has diameter that corresponds to approximately 4Γ. Figure 6.3(a) shows the normalised transmission (red curve) and phase shift (orange curve) of THz radiation, in the directions normal to the sample along the four periods of the blazed grating. As pointed out above the careful selection of the 8 carrier densities results into linear phase shift that will consequently give rise to beam steering.

To calculate the beam steering we use a model based on diffraction theory that can predict the diffraction pattern of a beam diffracted by a blazed grating with properties such as the one shown in Fig. 6.3(a) The far-field intensity pattern $I(\theta)$ of a grating structure can be determined by calculating the Fourier transform of the

complex transmission function $\tilde{T}(x)$ of the structure that causes the diffraction

$$I(\theta) = \mathcal{F}[\tilde{T}(x)]^2 = \mathcal{F}\left[T(x)e^{i\varphi(x)}\right]^2, \tag{6.3}$$

The red curve in Fig. 6.3(b) shows the far-field intensity pattern $I(\theta)$ of the blazed grating calculated using Eq. (6.3), while the orange curve is the intensity pattern of the complementary grating, i.e., a blazed grating with the same grating constant and N decreasing from left to right for each grating period. Besides the central peak, which represents the zeroth order diffraction, the $+1$ and -1 diffracted orders at 30^o and -30^o respectively are also present. The phase gradient introduces a pronounced asymmetry in the intensity between these orders, which is in accordance with the generalised law of reflection and refraction.

Based on the diffraction theory, the beam steering efficiency is influenced by the following three key ingredients. The most important is the phase shift $\Delta\varphi(x)$ experienced by the transmitted wave in each grating period. When the phase shift is less than 2π part of the wave is scattered into other diffraction orders, such as the zeroth, and the beam steering efficiency decreases. Additionally, the efficiency is also influenced by the transmission amplitude $\tilde{T}(x)$ along the surface of the photo-excited semiconductor. If the transmission is less than unity, THz waves are absorbed or reflected by the grating structure and hence the efficiency of the grating decreases. Finally, the efficiency of the blazed grating can be further improved by increasing the number of the grating periods. By increasing this number, the grating orders can become sharper resulting therefore to more selective beam steering.

The finite amount of periods in the grating shown in Fig. 6.3(a), along with the reduced transmission and the limited phase shift, are the reasons for the relatively weak change in the asymmetry between the two complementary blazed gratings.

6.3.2 THz diffraction measurements

Figure 6.4(a) shows images of the two complementary blazed gratings photo-generated with the technique discussed in Chapter 2. The images were taken by replacing the GaAs sample in the setup by a CCD camera. The colour scale represents the illumination fluence. The upper panel displays the grating with increasing carrier density N in each period from left to right, while the lower panel corresponds to the grating with decreasing carrier density N. Cuts through the images along the horizontal dashed lines are shown in the central panel of Fig. 6.4(a) by the red and orange curves for the increasing and decreasing carrier densities, respectively. The right axis in this panel is the estimated photo-generated carrier density obtained from the illumination fluence.

Due to the fixed configuration of the THz spectrometer setup for measuring zeroth-order transmissions ($\theta = 0^o$), we used a pyroelectric detector to detect the ± 1 diffracted orders of the photo-generated blazed gratings. In order to improve the detected signal, a Winston cone was placed in front of the detector to collect the radiation over a larger solid angle, 0.56 sr. The Winston cone is very sensitive to the angle of incidence,

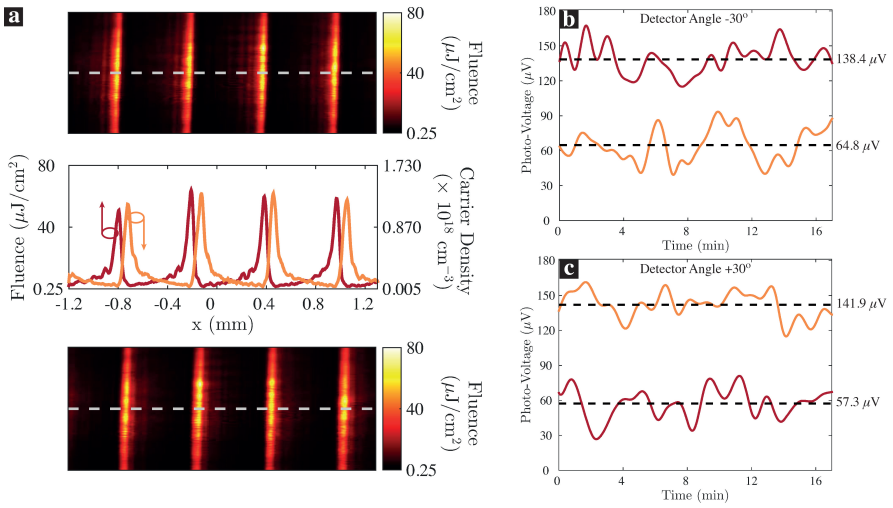

Figure 6.4: (a) CCD camera images of the projected images taken at the sample position. The pump beam is spatially modulated by the SLM in the shape of a blazed grating with $\Gamma = 600$ μm with a carrier density tail to the left (top) and to the right (bottom). The central panel shows horizontal cuts through both gratings. (b) Output of the pyroelectric detector at a position of $\theta = -30^o$ with respect to the normal of the surface of the sample. The orange curve corresponds to the blazed grating with decreasing carrier density from left to right, while the red curve corresponds to the blazed grating with decreasing carrier density from right to left. (c) The same as in (b) but at a detector angle of $\theta = 30^o$ with respect to the normal of the surface of the sample.

e.g. for an angle of incidence that deviates 4^o from its axis the signal detected by the pyroelectric detector is reduced by a factor of 2. In addition, the cone functions as a spatial filter that significantly reduces the detection of THz radiation at angles other than the ± 1 diffracted orders. In our experiments, the pyroelectric detector was placed at a distance of 72 mm behind the sample at $\theta = -30^o$ and $\theta = +30^o$ with respect to the normal of the sample surface. The pyroelectric detector could only be used for relative intensity measurements because there is no calibration available for the absorption efficiency of the device at frequencies below 0.75 THz. The absorption efficiency for frequencies between $0.75 - 1$ THz is $\sim 10\%$ and increases rapidly for higher frequencies. The photo-voltage in the pyroelectric detector was detected using a lock-in amplifier and a mechanical chopper modulating the THz waves at 5 Hz.

The photo-voltage from the pyroelectric detector is measured within a time window of 17.5 minutes for $\theta = \pm 30^o$ and for the two blazed gratings, as shown in Figs. 6.4(b) and 6.4(c) respectively. In this time window several low frequency noise contributions are observed, and therefore to illustrate the selective beam steering we define the mean value of the signal, indicated by the dark dashed lines in Figs. 6.4(b) and 6.4(c). From these figures we observe a distinct difference in the mean values, favouring the left steering grating when the detector is placed at $\theta = -30^o$ and the right steering

grating when the detector is at $\theta = +30^o$. The intensity ratio $R = I_{\text{left}}/I_{\text{right}}$ between the mean values at $\theta = \pm 30^o$ are $R_{-30^o} = 2.14 \pm 0.21$ and $R_{30^o} = 0.40 \pm 0.04$. The uncertainties on these ratios are determined by conducting a dark photo-voltage measurement with the THz beam blocked, which is later used to filter the noise from the signal. By determining the frequency components of the background noise we apply to the measurements performed at $\theta = \pm 30^o$ a low frequency cut-off filter that filters the contribution from the background noise. The error, σ, on the photo-voltage is determined by calculating the variance of the filtered signal. Due to the long integration time of the lock-in amplifier ($\tau_{\text{lock-in}} = 20$ s with a filter slope of 24 dB/Oct) not all the data points shown in the curves of Figs. 3(b) and 3 (c) are uncorrelated. Based on the response time of the locking amplifier for the above settings, there are 9 fully uncorrelated photo-voltage data points in each 17.5 min measurement. Therefore, we can treat these measurements as independent, all with an uncertainty σ. From this we can determine the standard error on the mean value of the photo-voltage I, which is given by $\sigma_{\text{err}} = \sigma/\sqrt{9}$, while the errors on the intensity ratios $\sigma_{\text{R}_{\pm 30^o}}$ are calculated through standard error-propagation.

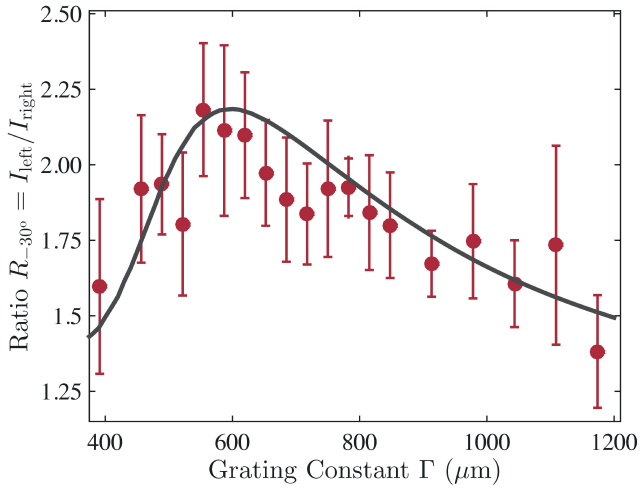

Figure 6.5: Ratio between the diffracted THz intensities by the left and the right steering blazed gratings measured at $\theta = -30^o$ for a series of grating constants. The red data points are measurements while the gray curve is a calculation based on the diffraction theory.

To further investigate the beam steering properties of the blazed gratings, a new set of measurements was conducted in which the pyroelectric detector was kept fixed at $\theta = -30^o$. The photo-voltage was measured for a series of left and right steering gratings with grating constants varying between $\Gamma = 391$ μm and $\Gamma = 1174$ μm. The ratios between left and right blazed gratings are shown with red data points in Fig. 6.5, while the grey curve corresponds to a model based on the diffraction theory. For both the experiments and the model we have arbitrarily chosen to use three periods

for each grating, since the median of the selected range of gratings corresponds to $\Gamma_{\mathrm{m}} = 800\ \mu$m, which is approximately one third of the full width at half maximum of the THz beam, i.e. FWHM = 2.3mm $\sim 3\Gamma_{\mathrm{m}}$. The experimental results of Fig. 6.5 show a maximum in the intensity ratio R_{-30^o} that can be translated into an optimum beam steering for a grating period of $\Gamma = 600\ \mu$m.

The grey curve in Fig. 6.5 is calculated using diffraction theory for the different grating constants. The diffracted intensity for each grating was calculated in an interval of $\pm 8^o$ around $\pm 30^o$ and weighted by the angular response of the Winston cone [31], the frequency dependent responsivity of the pyroelectric detector [32], and the spectrum of the generated THz radiation. The simple diffraction model describes both qualitatively and quantitatively the measurements within the range of the error bars.

Therefore, based on the results of Fig. 6.4, the blazed gratings investigated in this chapter do not only selectively steer the THz waves in the desired direction, but furthermore Fig. 6.5 shows that the optimum results can only be achieved for a specific grating constant.

6.4 Conclusions

In conclusion, we have demonstrated selective THz beam steering using a blazed grating metasurface. This simple metasurface is realised by photo-exciting a grating with linearly increasing carrier density along each period. The linear increase in of the carrier density introduces a phase gradient discontinuity on the surface of the semiconductor that steers an incident THz beam on the $+1$ or -1 diffraction orders of the grating.

These results constitute a proof-of-principle for selective THz beam steering using photo-generated devices and can be generalised to more complicated configurations [16–27] that can be used in combination with THz transceivers for Tbps wireless communications.

Bibliography

[1] European Telecommunications Network Operators' Association, *Annual economic report I*, Technical report, 2014.

[2] S. Cherry, *Edholm's law of bandwidth*, Spectrum, IEEE **41**, 58 (2004).

[3] T. Kürner and S. Priebe, *Towards THz Communications - Status in Research, Standardization and Regulation*, **35**, 53 (2014).

[4] I. F. Akyildiz, J. M. Jornet, and C. Han, *Terahertz band: Next frontier for wireless communications*, Physical Communication **12**, 16 (2014).

[5] L. Columbus, *IDC: 87% Of Connected Devices Sales By 2017 Will Be Tablets And Smartphones*, 2013, [Online; posted 12-Sep-2013].

[6] I. Lunden, *6.1B Smartphone Users Globally By 2020, Overtaking Basic Fixed Phone Subscriptions*, 2015, [Online; posted 02-Jun-2015].

[7] B. Marr, *Big Data: 20 Mind-Boggling Facts Everyone Must Read*, 2015, [Online; posted 30-Sep-2015].

[8] S. Abadal, E. Alarcón, A. Cabellos-Aparicio, M. Lemme, and M. Nemirovsky, *Graphene-enabled wireless communication for massive multicore architectures*, Communications Magazine, IEEE **51**, 137 (2013).

[9] M. Rosker and H. Wallace, *Imaging Through the Atmosphere at Terahertz Frequencies*, in *Microwave Symposium, 2007. IEEE/MTT-S International*, pages 773–776, 2007.

[10] J. Jornet and I. Akyildiz, *Channel Modeling and Capacity Analysis for Electromagnetic Wireless Nanonetworks in the Terahertz Band*, Wireless Communications, IEEE Transactions on **10**, 3211 (2011).

[11] N. Yu, P. Genevet, M. A. Kats, F. Aieta, J.-P. Tetienne, F. Capasso, and Z. Gaburro, *Light Propagation with Phase Discontinuities: Generalized Laws of Reflection and Refraction*, Science **334**, 333 (2011).

[12] A. V. Kildishev, A. Boltasseva, and V. M. Shalaev, *Planar Photonics with Metasurfaces*, Science **339**, 1232009 (2013).

[13] H. J. Visser, *Array and phased array antenna basics*, John Wiley & Sons, 2006.

[14] J. Sun, E. Timurdogan, A. Yaacobi, E. S. Hosseini, and M. R. Watts, *Large-scale nanophotonic phased array*, Nature **493**, 195 (2013).

[15] S. Larouche and D. R. Smith, *Reconciliation of generalized refraction with diffraction theory*, Opt. Lett. **37**, 2391 (2012).

[16] F. Aieta, P. Genevet, N. Yu, M. A. Kats, Z. Gaburro, and F. Capasso, *Out-of-Plane Reflection and Refraction of Light by Anisotropic Optical Antenna Metasurfaces with Phase Discontinuities*, Nano Letters **12**, 1702 (2012).

[17] B. Walther, C. Helgert, C. Rockstuhl, F. Setzpfandt, F. Eilenberger, E.-B. Kley, F. Lederer, A. Tünnermann, and T. Pertsch, *Spatial and Spectral Light Shaping with Metamaterials*, Advanced Materials **24**, 6300 (2012).

[18] S. Sun, K.-Y. Yang, C.-M. Wang, T.-K. Juan, W. T. Chen, C. Y. Liao, Q. He, S. Xiao, W.-T. Kung, G.-Y. Guo, L. Zhou, and D. P. Tsai, *High-Efficiency Broadband Anomalous Reflection by Gradient Meta-Surfaces*, Nano Letters **12**, 6223 (2012).

[19] M. Farmahini-Farahani and H. Mosallaei, *Birefringent reflectarray metasurface for beam engineering in infrared*, Opt. Lett. **38**, 462 (2013).

[20] N. K. Grady, J. E. Heyes, D. R. Chowdhury, Y. Zeng, M. T. Reiten, A. K. Azad, A. J. Taylor, D. A. R. Dalvit, and H.-T. Chen, *Terahertz Metamaterials for Linear Polarization Conversion and Anomalous Refraction*, Science **340**, 1304 (2013).

[21] A. Pors and S. I. Bozhevolnyi, *Plasmonic metasurfaces for efficient phase control in reflection*, Opt. Express **21**, 27438 (2013).

[22] X. Zhang, Z. Tian, W. Yue, J. Gu, S. Zhang, J. Han, and W. Zhang, *Broadband Terahertz Wave Deflection Based on C-shape Complex Metamaterials with Phase Discontinuities*, Advanced Materials **25**, 4567 (2013).

[23] Z. Wei, Y. Cao, X. Su, Z. Gong, Y. Long, and H. Li, *Highly efficient beam steering with a transparent metasurface*, Opt. Express **21**, 10739 (2013).

[24] T. Roy, A. E. Nikolaenko, and E. T. F. Rogers, *A meta-diffraction-grating for visible light*, Journal of Optics **15**, 085101 (2013).

[25] M. D. Goldflam, T. Driscoll, D. Barnas, O. Khatib, M. Royal, N. Marie Jokerst, D. R. Smith, B.-J. Kim, G. Seo, H.-T. Kim, and D. N. Basov, *Two-dimensional reconfigurable gradient index memory metasurface*, Applied Physics Letters **102**, 224103 (2013).

[26] D. Hu, X. Wang, S. Feng, J. Ye, W. Sun, Q. Kan, P. J. Klar, and Y. Zhang, *Ultrathin Terahertz Planar Elements*, Advanced Optical Materials **1**, 186 (2013).

[27] Y. Huang, Q. Zhao, S. K. Kalyoncu, R. Torun, Y. Lu, F. Capolino, and O. Boyraz, *Phase-gradient gap-plasmon metasurface based blazed grating for real time dispersive imaging*, Applied Physics Letters **104**, 161106 (2014).

[28] P. Yeh, *Optical Waves in Layered Media*, John Wiley & Sons, 2005.

[29] M. C. Troparevsky, A. S. Sabau, A. R. Lupini, and Z. Zhang, *Transfer-matrix formalism for the calculation of optical response in multilayer systems: from coherent to incoherent interference*, Opt. Express **18**, 24715 (2010).

[30] M. Schall and P. U. Jepsen, *Photoexcited GaAs surfaces studied by transient terahertz time-domain spectroscopy*, Opt. Lett. **25**, 13 (2000).

[31] Gentec-EO, *Winston Cone Accesory (THZ-WC-13)*, Technical report, 2014.

[32] Gentec-EO, *THZ-B Detectors and T-Rad Modules*, Technical report, 2014.

Appendices

A

Calculation of TM modes for multilayered structures

In order to study the properties of propagating surface modes (SPPs, surface plasmon polaritons) on photoexcited materials we begin from Maxwell's equations for TM-polarized waves. The equations that describe the propagation of TM waves in a medium with permittivity $\tilde{\epsilon} = \epsilon_1 + i\epsilon_2$ are,

$$E_x = -\frac{i}{\omega\epsilon_0\tilde{\epsilon}}\frac{\partial H_y}{\partial z}, \tag{A.1a}$$

$$E_z = -\frac{\beta}{\omega\epsilon_0\tilde{\epsilon}}H_y \tag{A.1b}$$

$$\frac{\partial^2 H_y}{\partial z^2} = -\left(k_0^2\tilde{\epsilon} + \beta^2\right)H_y, \tag{A.1c}$$

where ϵ_0 is the free space permittivity, ω is the angular frequency of the wave, β is the in-plane propagation wavevector, which is assumed for simplicity to be along the x-direction and $k_0 = \omega/c$ is the free space wavevector.
One of the main requirements for a system to support a SPP is the existence of an interface between a material with dielectric nature ($\epsilon_1 > 0$) and a material with metallic nature ($\epsilon_1 < 0$). In such a system, solution of the above wave equation (Eq. (A.1c)) subjected to the continuity equations for the $H_y(z)$ field can lead to a propagating surface mode with an evanescent decay profile along the direction perpendicular to the interface (z-direction).

For phototoexcited materials the permittivity of the metallic region is not anymore homogeneous but it varies along the direction perpendicular to the propagation of the surface wave, i.e. $\tilde{\epsilon} = \tilde{\epsilon}(z)$. To account for this variation we divide the photoexcited region into infinitesimally small segments for which the permittivity of consecutive segments is to a first approximation constant,

$$\tilde{\epsilon}_i(z) \simeq \tilde{\epsilon}_{i+1}(z + dz) \text{ with dz} \to 0,$$

To calculate the SPP modes for a photoexcited material we solve the wave equation (Eq. (A.1c)) for a multilayer structure composed out of N+1 materials (including substrate and upperstrate) with permittivities $\tilde{\epsilon}^i$ and N interfaces, namely at $z = (d_1, d_2 \dots d_N)$. The solution to the wave equation is a superposition of two periodic waves with opposite propagation wavevectors,

$$H_y^i = A_i e^{i\beta x} e^{k_i z} + B_i e^{i\beta x} e^{-k_i z}, \tag{A.2}$$

where $k_i^2 = \beta^2 - k_0^2 \tilde{\epsilon}^i$ is the wavevector along the propagation direction. The coefficients A_i and B_i are constants determined by requiring that the $H_y(z)$ and $E_x(z)$ fields are continuous at the interfaces,

$$H_y^i\big|_{z=d_i} = H_y^{i+1}\big|_{z=d_i}, \tag{A.3a}$$

$$\frac{1}{\tilde{\epsilon}^i} \left.\frac{\partial H_y^i}{\partial z}\right|_{z=d_i} = \frac{1}{\tilde{\epsilon}^{i+1}} \left.\frac{\partial H_y^{i+1}}{\partial z}\right|_{z=d_i}. \tag{A.3b}$$

The conditions for continuity of the fields will result into a set of 2N equations with 2N+2 unknowns (A_i and B_i coefficients). To have a physical solution of the wave equation the fields at the two extremes should vanish i.e. $H_y(z \to \pm\infty) = 0$, which implies that $A_{N+1} = 0$ and $B_1 = 0$. In a matrix notation the above system of equations is simplified to,

$$M\mathbf{x} = \mathbf{0}, \tag{A.4}$$

where the matrix M is,

$$\begin{pmatrix}
e^{k_1 d_1} & 0 & -e^{k_2 d_1} & -e^{-k_2 d_1} & \dots & 0 & 0 & 0 & 0 \\
\frac{k_1}{\tilde{\epsilon}_1} e^{k_1 d_1} & 0 & -\frac{k_2}{\tilde{\epsilon}_2} e^{k_2 d_1} & \frac{k_2}{\tilde{\epsilon}_2} e^{-k_2 d_1} & \dots & 0 & 0 & 0 & 0 \\
\vdots & \vdots & \vdots & \vdots & \ddots & \vdots & \vdots & \vdots & \vdots \\
0 & 0 & 0 & 0 & \dots & e^{k_N d_N} & e^{-k_N d_N} & 0 & -e^{-k_{N+1} d_N} \\
0 & 0 & 0 & 0 & \dots & \frac{k_N}{\tilde{\epsilon}_N} e^{k_N d_N} & -\frac{k_N}{\tilde{\epsilon}_N} e^{-k_N d_N} & 0 & \frac{k_{N+1}}{\tilde{\epsilon}_{N+1}} e^{-k_{N+1} d_N}
\end{pmatrix}, \tag{A.5}$$

and $\mathbf{x} = \begin{pmatrix} A_1 & B_1 & A_2 & B_2 & \dots & A_{N+1} & B_{N+1} \end{pmatrix}$. The wavevector of the propagating SPP wave is given by minimizing the determinant of the above matrix in the complex plane, namely $\min_\beta(|M|)$. By substituting the wavevector β that minimizes the determinant of matrix M into Eq. (A.4) we can calculate the coefficients A_i and B_i by solving the linear system.

B

Diffusion of free carriers in photo-excited semiconductors

B.1 General solution of the diffusion equation with fixed boundaries

To investigate spatially and temporally the dynamics of photoexcited free carriers we solve the 1D diffusion equation for a system with finite length L and Robin boundary conditions at both interfaces. The general non-homogeneous diffusion equation is given by,

$$\frac{\partial N(z,t)}{\partial t} = D\frac{\partial^2 N(z,t)}{\partial z^2} + \Phi(z,t), \tag{B.1}$$

where $N(z,t)$ is the number of free carriers as a function of the pump-probe time and position, D is the diffusion coefficient with units m^2/s and $\Phi(z,t)$ is a continuous, non-singular function. The initial and boundary conditions are given by,

$$N(z,0) = f(z), \tag{B.2a}$$

$$s_1 N(0,t) + D_1 \left.\frac{\partial N(z,t)}{\partial z}\right|_{z=0} = h_1(t), \tag{B.2b}$$

$$s_2 N(0,t) + D_2 \left.\frac{\partial N(z,t)}{\partial z}\right|_{z=L} = h_2(t). \tag{B.2c}$$

The initial condition (Eq. (B.2a)) specifies the spatial distribution of free carriers at $t = 0$ as a function of the depth, which is usually an exponential function. Equations

(B.2b) and (B.2c) form a combination of Dirichlet and Neumann boundary conditions known as Robin boundary conditions. The constants $s_1 < 0$ and $s_2 > 0$, measured in m/s, indicate the rate for which the free carriers recombine at the front and back surface of the semiconductor respectively, hence providing a loss mechanism to the system. The rate for which the free carriers are reflected from the two surfaces and return back to the system is given by the constants D_1 and D_2 measured in units m^2/s. Finally, the continuous functions $h_1(t)$ and $h_2(t)$ provide a mechanism of free carrier generation at both the surfaces of the semiconductor.

The linear non-homogeneous diffusion equation with Robin boundary conditions can be solved analytically using a Green's function $\mathcal{G} \equiv \mathcal{G}(z,t;\xi,\tau)$. The integral form of the solution is,[1]

$$N(z,t) = \int_0^L \int_0^t \mathcal{G}\ \Phi(\xi,\tau)d\tau d\xi + \int_0^L \mathcal{G}\ f(\xi)d\xi + \int_0^t \left[\frac{D}{D_2}\mathcal{G}\ h_2(\tau)\right]\Big|_{\xi=L} d\tau - \int_0^t \left[\frac{D}{D_1}\mathcal{G}\ h_1(\tau)\right]\Big|_{\xi=0} d\tau, \quad \text{(B.3)}$$

where the Green's function for a finite length system is given by the following sum [2],

$$\mathcal{G}(z,t;\xi,\tau) = \sum_{n=1}^{\infty} H(t-\tau)\varphi_n(\xi)\varphi_n(z)e^{-k\,D(t-\tau)}, \quad \text{(B.4)}$$

where $H(t-\tau)$ is the Heaviside step function and φ_n is given from the solution to the 1D Sturm-Liouville problem,

$$\varphi''(z) + \lambda\varphi(z) = 0 \qquad 0 \le z \le L, \quad \text{(B.5)}$$

with boundary conditions

$$s_1\varphi(0) + D_1\varphi'(0) = 0,$$
$$s_2\varphi(L) + D_2\varphi'(L) = 0.$$

The solution to the Sturm-Liouville problem will result into a superposition of periodic functions ($\lambda = \kappa^2 > 0$) and a linear function ($\lambda = 0$). The solution for $\lambda = \kappa^2$ is,

$$\varphi_n(z) = A_n\left(\cos(\kappa_n z) - \frac{s_1}{D_1\kappa_n}\sin(\kappa_n z)\right), \quad \text{(B.7)}$$

where κ_n are the eigenvalues of the equation that can be numerically calculated from,

$$\tan(\kappa_n z) = \kappa_n \frac{\frac{s}{D} - \frac{s}{D}}{\kappa_n^2 + \frac{s\,s}{D\,D}} \equiv \kappa_n\Omega_n,$$

and A_n is an integration constant that can be calculated using the orthogonality property of the Sturm-Liouville eigenfunctions,

$$A_n^{-2} = \frac{L}{2}\left[1 + \left(\frac{s_1}{D_1\kappa_n}\right)^2\right] + \frac{1}{2}\left[1 - \left(\frac{s_1}{D_1\kappa_n}\right)^2\right]\frac{\Omega_n}{1+\kappa_n^2\Omega_n^2} - \frac{s_1}{D_1}\frac{\Omega_n^2}{1+\kappa_n^2\Omega_n^2}. \quad \text{(B.8)}$$

For the case where $\lambda = 0$ the solution to Eq. (B.5) is linear,

$$\varphi(z) = C\left(1 - \frac{s_1}{D_1}z\right), \tag{B.9}$$

where the integration constant C is given by,

$$C^{-2} = L - \frac{s_1}{D_1}L^2 + \frac{s_1^2}{3D_1^2}L^3.$$

The above solution exists only when the following condition is fulfilled,

$$1 - \frac{s_1}{\alpha_1}L = \frac{s_1}{s_2}\frac{D_2}{D_1}.$$

The profile of the free carriers as a function of time, which can be directly related to pump-probe carrier dynamics measurements is given by integrating the number of free carriers inside the region $0 \leq z \leq L$ for all the times, namely,

$$N(t) = \int_0^L N(z,t)\ dz. \tag{B.10}$$

In the case of a non-linear non-homogeneous diffusion equation that contains quadratic and cubic carrier concentration terms an analytical solution cannot be found using Green's functions. In that case the solution can be calculated numerically.

Bibliography

[1] A. D. Polyanin, *Handbook of Linear Partial Differential Equations for Engineers and Scientists*, Chapman and Hall/CRC, 2001.

[2] D. G. Duffy, *Green's functions with applications*, Chapman and Hall/CRC, 2001.

C

Phase of travelling waves passing through absorbing interfaces

In order to illustrate the phase acquired by travelling waves passing through absorbing interfaces, we consider a plane wave E_1 with an amplitude A_1 in a non-absorbing medium 1 ($n_1 > 0$, $\kappa_1 = 0$) travelling in the z direction. The field in an absorbing medium 2 ($n_2 > 0$, $\kappa_2 > 0$) upon transmission at normal incidence can be written as

$$E_2 = \tilde{t}_{1,2} E_1 = \tilde{t}_{1,2} A_1 e^{i(k z - \omega t)}, \tag{C.1}$$

where $k_1 = 2\pi/\lambda$ denotes the wave number, ω_1 is the angular frequency of the wave in medium 1, and $\tilde{t}_{1,2}$ is the complex Fresnel coefficient given by

$$\tilde{t}_{1,2} = |t_{1,2}|\, e^{i\varphi} = \frac{n_1}{n_1 + n_2 + i\kappa_2}. \tag{C.2}$$

The phase shift upon transmission at the interface is given by

$$\Delta\varphi_{1,2} = -\tan^{-1}\left(\frac{\kappa_2}{\mathrm{n}_1 + \mathrm{n}_2}\right), \tag{C.3}$$

and the phase shift of the EM wave transmitted into the second layer is always negative if the medium 2 has a non-zero extinction coefficient κ_2. The above derivation can be extended to a system that contains a layer with refractive index $n_2, \kappa_2 > 0$ in

between two layers with $n_1 > 1$ and $\kappa_1 = 0$ by taking the product of the complex transmission coefficients at the two interfaces $\tilde{t}_{1,2}$ and $\tilde{t}_{2,3}$. The total phase shift due to the transmission though the interfaces in such system is,

$$\Delta\varphi_{1,3} = \Delta\varphi_{1,2} + \Delta\varphi_{2,3} = -\tan^{-1}\left(\frac{\kappa_2(\mathrm{n}_2 - \mathrm{n}_1 + \kappa_2^2)}{(\mathrm{n}_1 + \mathrm{n}_2)(\mathrm{n}_2^2 + \mathrm{n}_1\mathrm{n}_2 + \kappa_2^2) + \mathrm{n}_1\kappa_2^2}\right). \quad \text{(C.4)}$$

Although the above equation (Eq. (C.4)) is an approximation that ignores multiple reflections at the interfaces of the thin GaAs sample, it illustrates that the phase shift due to the interfaces is negative if the central layer is absorptive, $\kappa_2 > 0$ and $n_2 > n_1$, as in the case for multilayered sample investigated in this thesis.

Photo-generated Terahertz devices: Summary

Modifying the properties of light, such as dispersion, polarization as well as directionality is essential in many fields of science and technology, including among others optical and IR spectroscopy, imaging, opto-electronics, telecommunications etc. The development of devices made out of plasmonic and metamaterial structures has led to a remarkable control of the properties of light. The advances in these fields of science are particularly interesting, especially for the technologically important terahertz (THz) frequency regime. A great emphasis has been given over the last ten years on studying and developing active plasmonic and metamaterial devices that can tune the properties of THz waves in a continuous way. These studies have been mainly dominated by the use of metallic structures on semiconducting substrates that are electrically tuneable using a bias voltage through the semiconductor. Although electrically tuning the properties of metallic structures is well established, the potential of optically changing the properties of these structures and the way they interact with THz waves has not been fully explored.

In this thesis we have studied the physical and technical foundations of optically photo-generating plasmonic and metamaterial THz devices on semiconducting substrates. Using a technique that has been developed during the PhD thesis we have studied both experimentally and theoretically the interaction of these photo-generated devices with THz waves. The principle of this technique is based on the optical excitation of a semiconductor with a structured beam that contains the THz devices. The photo-excited electrons in the illuminated regions will locally render the behaviour of the semiconductor metallic allowing the THz waves to resonantly interact with the free electrons.

For the purposes of this project we have designed and assembled a time-resolved THz time domain spectrometer (THz-TDS) that has a THz beam and an optical beam used for excitation of free carriers in semiconductors (Chapter 2). The spectrometer

has been modified to include a spatial light modulator along with a projection system, which is used for spatially shaping the excitation beam with plasmonic and metamaterial structures. Furthermore, for studying the optical properties and temporal dynamics of a photo-excited semiconductor we have developed a transfer matrix algorithm that is combined with the temporal evolution of the free carriers due to diffusion mechanisms.

To fully understand the interaction of THz waves with the free electrons of a photo-excited semiconductor, in Chapter 3 we have studied theoretically the photo-excitation of THz surface waves, known as surface plasmon polatitons (SPPs). In this study we investigate the possibilities of actively tuning the properties of SPPs by varying the free electron concentration, excitation depth, substrate and diffusion parameters.

Following the above theoretical study, in Chapter 4 we have experimentally demonstrated the excitation of localized surface plasmon polaritons (LSPPs) in plasmonic dipole antennas at THz frequencies. The tunability of these antennas is elucidated by optically varying the dimensions as well as the free electron concentration of the antennas.

A more extensive study presented in Chapter 5 investigates experimentally the interaction of THz waves with two coupled photo-excited linear antennas separated by a sub-wavelength gap (dimer configuration). In this study we optically tune the load of the gap that connects the two antennas and we observe that the LSPPs can be either capacitively or inductively coupled. Our results demonstrate that for particular loads of the gap, the coupling can be at the same time both capacitive and inductive. These results are supported theoretically by a phenomenological model that considers a dimer antenna coupled with a LC circuit.

Finally, in Chapter 6 we show the valorization potential of photo-exciting plasmonic and metamaterial structures on semiconductor surfaces. To demonstrate this we use optically excited blazed gratings by spatially varying the concentration of free electrons along the surface of the semiconductor, which therefore changes the refractive index. By doing this we introduce a linear phase gradient along the surface of the semiconductor that results into steering of THz waves.

List of Publications

This thesis is based on the following publications:

1. G. Georgiou, H.K. Tyagi, P. Mulder, G.J. Bauhuis, J.J. Schermer and J. Gómez Rivas, *Photo-generated THz antennas*, Scientific Reports **4**, 3584 (2014) **(Chapter 4)**.

2. T.P. Steinbusch, H.K. Tyagi, M.C. Schaafsma, G. Georgiou and J. Gómez Rivas, *Active terahertz beam steering by photo-generated graded index gratings in thin semiconductor films*, Optics Express **22**, 26559 (2014) **(Chapter 6)**.

3. G. Georgiou, C. Tserkezis, M.C. Schaafsma, J. Aizpurua and J. Gómez Rivas, *Active loaded plasmonic antennas at THz frequencies: Optical control of their capacitive - inductive coupling*, Physical Review B **91**, 125443 (2015) **(Chapter 5)**.

4. G. Georgiou and J. Gómez Rivas, *Photo-generated surface plasmon polaritons at terahertz frequencies*, To be submitted in Physical Review B (2015) **(Chapter 3)**.

Other publications by the author:

1. M.C. Schaafsma, G. Georgiou and J. Gómez Rivas, *Enhanced THz extinction in arrays of resonant semiconductor particles*, Optics Express **23**, 24440 (2015).

2. A. Bhattacharya, G. Georgiou, S. Sawallich, C. Matheisen, M. Nagel and J. Gómez Rivas, *Anomalous Spectral Shifts between Near- and Far-field Resonances in Terahertz Antennas*, (Submitted in Applied Physics Letters) (2015).

3. G. Georgiou, N. Shen, T. Koschny, C. Soukoulis and J. Gómez Rivas, *Electronamgnetically incuced transparency in photo-imprinted metamaterials*, (in preparation - to be submitted in Nature Communications) (2015).

4. G. Georgiou and J. Gómez Rivas, *Dynamic control of surface plasmon modes in photo-generated plasmonic antennas*, (in preparation - to be submitted in Applied Physics Letters) (2015).

Conference proceedings:

1. G. Georgiou, M.C. Schaafsma and J. Gómez Rivas, *Ultrafast Active Control of Plasmonic Resonances at THz Frequencies* in Nano-Structures for Optics and Photonics, Edited by B. Di Bartolo, J. Collins and L. Silvestri, Ch. 43, pp. 499-500, Springer - Netherlands (2015)

2. G. Georgiou, M.C. Schaafsma, H.K. Tyagi, T.P. Steinbusch and J. Gómez Rivas, *Photo-generation of resonant structures at THz frequencies*, 39th International Conference on Infrared Millimeter and Terahertz waves (IRMMW-THz), 2014, pp.1-1, 14-19 Sept. 2014

Patents:

1. J. Gómez Rivas, G. Georgiou, H. Tyagi, M.C. Schaafsma, *Photo-generated THz circuits and resonators*, EP Application No. 13176199

Acknowledgements

Looking back on all the work of this four-year project, I feel glad that this thesis is the outcome of a collective and fruitful work supported by many people. Therefore, I would like to dedicate this last chapter to the people that were close to me all these years and have contributed to this work.

A very special thanks to my supervisor Jaime, who has been a great inspiration throughout my research, for motivating and supporting this work and for trusting me, especially in the lab. Jaime, you have taught me how to perform high quality experimental research, by having a critical, yet constructive eye to my results. You have taught me to value what is important and how to look from different perspectives into my results in order to get the most interesting physics out of them. Furthermore, one of the things that I really appreciated during the last years are the high ethical standards that you have in your group. I have honestly really enjoyed every conversation we had on ethics and research quality and I am sure that this will be my greatest inheritance from your group.

The experiments of this thesis would not have been possible without samples. I had the luck to collaborate with Gerard and Peter from the group of Prof. John Schermer at the Radboud University in Nijmegen. With their vast knowledge on semiconductor fabrication they have provided us with high quality samples in a very short time. These samples have been used extensively throughout this four year project.

Thanks also to my collaborators from San Sebastian, Spain, Javier Aizpurua and Christos Tserkezis with whom I had the pleasure to work closely for the interpretation of the results in Chapter 5. Moreover, thanks to my collaborators from AMES laboratory in the US, Costas Soukoulis, Thomas Koschny and Nianhai Shen who have provided a valuable insight on photo-generated metamaterials. I would also like to thank Michael Nagel and Christopher Matheisen from Protemics, Germany, for contributing with their expertise in our THz near field spectroscopy measurements and also Luis Martin Moreno for his input on our graphene projects.

As a member of the Surface Photonics group I had the pleasure of working close to a number of talented people, Hemant Tyagi, Martijn Schaafsma, Arko Bhattacharya, Audrey Berrier, Alexei Halpin, Cristiaan Mennes, Tom Steinbush, Mark Aarts, Gabriel Lozano, Giuseppe Pirruccio, Said Rodriguez, Grzegorz Grzela, Tommy Barten, Mo-

hammed Ramezani, Niels van Hoof and Dick van Dam. To my very good colleague and friend Hemant with whom I shared an office for two and a half years: Thanks a lot for all your guidance especially during the first months of my PhD, for the great discussions we had on politics, ethics and life in general as well as for your generous hospitality. Special thanks also to Arko for working close to me during the last three years and for his input to my work. Martijn, thanks for all the motivating science discussions we had and for being patient with me all these years. Gabriel thanks a lot for all the useful advice, for not humiliating me too much in tennis and for your hospitality in Andalusia. Said, I am so grateful that I have worked with you, for all the interesting discussions we had on exciton polaritons and on designing new experiments. Giuseppe, thanks a lot for your very important contribution to the graphene project and for sharing some of your analysis code. Also I would like to acknowledge the contribution of Tom, who performed the measurements and analysis for the last chapter in my thesis.

The fruitful and motivating discussions I had with my AMOLF colleagues has been the highlight of my PhD. Special thanks to Nir, Lutz, Oleg, Clara and Kobus for their valuable comments on my results and for their useful suggestions on my experiments. More generally, I would also like to thank my colleagues and the group leaders at the Center for Nanophotonics for their constructive remarks on my results and my presentation skills during the colloquiums and the poster sessions.

Moreover, I want to thank the group of Prof. Huib Bakker for providing us space in their lab during early 2012 for our initial experiments and Stefan for lending me optics. Thanks also to the group of Prof. Mischa Bonn and especially to Ronald Ulbricht and Soeren Jensen for their valuable input on THz spectroscopy.

I am also very thankful to the Ultrafast Science group of Prof. Andreas Othonos in Cyprus for all the knowledge and training I got on ultrafast optics and spectroscopy in solid state systems and nanowires. Special thanks to Demerta Tsokkou for the enlightening discussions on ultrafast dynamics in semiconductors and to Constantinos Papartyphonos for his instructive information on semiconductor fabrication.

Working in a research institute, like AMOLF, I have always had many people around me to support my research and experiments. The support of Niels, Rob and Hinko has been valuable. With your support, during the early stage of my PhD, we managed in just a few months to turn an empty room into a state of the art laboratory. I am also really grateful for all the assistance I received from our laser and non linear optics specialist. Jan thank you for being there whenever I needed you and for all the priceless knowledge you taught me during these four years.

Furthermore, the help and support from the various departments of AMOLF has been very important for the results of this thesis. More specifically I would like to thank Duncan and Ronald from the electrical engineering department for building the balance photodiodes of my experiments and for their help on lock-in amplifiers as well as Luc and Marco from the software engineering department for writing the "Hermes" and "Diana" data acquisition software. Also from the mechanical engineering department I would like to thank Ilya and Henk-Jan for designing critical components of my experimental setup as well as Dirk-Jan and Ricardo for the design of some

of my thesis figures. From the ICT department I would like to thank Wiebe for his support on Lumerical and Jan for his help on the Unix servers. I will never forget the professionalism of the secretarial and HR office at AMOLF who helped me and supported me, especially when I moved to Netherlands. Thanks to Juanita, Anouk, Wouter, Lenny, Valeska and Sabine.

Several aspects of the content of this thesis have been improved due to the valuable comments of the committee members, whose names are listed in the first page of this book. In particular I would like to thank Prof. Javier Aizpurua and Prof. Thomas Dekorsy who are coming to The Netherlands from Spain and Germany and also Prof. Andrea Fiore who is the second promotor for this thesis.

Some of the contents of this thesis would not have been clear and easy to read without the contribution of Suzanne. Thanks a lot for all your comments and for proof-reading parts of this work. Thanks also to Iliana for designing the cover of this thesis, capturing in her design an artistic illustration of what is presented in this book.

The people that I would like to thank the most are my two paranymphs, Alessandro and Nicola. Thank you for being close to me for all these years, and for standing by my side during the defence of this thesis.

Last but not least, I want to recognise all the efforts and support from my family. To my parents Eleni and Mamas: The book that you were waiting for long time is finally finished. Thank you very much for supporting my studies for all this time, for motivating me to pursue physics and for your endless belief in my self and my skills.

Thank you,
Giorgos

About the Author

Giorgos Georgiou was born on the 17th of September 1985 in Nicosia, Cyprus. During his high school studies, Giorgos showed a great interest for natural sciences and he was motivated by his teachers to participate in national Olympiads for physics and to experimental contests for young scientists. After finishing his high school studies in 2003 at Acropolis high school in Nicosia, Cyprus, he joined the army for a two years service in the airforce. In 2005 Giorgos started a four year curriculum in physics at the University of Cyprus, where he focussed on high energy physics and cosmology under the supervision of Prof. Nicolaos Toumbas. After his graduation in 2009 he got an internship position at the European Organization for Nuclear Research (CERN) in Geneva, Switzerland, where he worked in the CMS collaboration.

In September 2009 he begun a Master's degree in physics at the University of Cyprus under the supervision of Prof. Andreas Othonos in the laboratory for ultrafast optics. His Master's research project was focussed on ultrafast dynamics in solid state systems. Giorgos graduated first of his class in 2011.

Soon after his Master's graduation he started his PhD research in the group of Jaime Gómez Rivas at the Institute for Atomic and Molecular Physics (AMOLF) in The Netherlands. His PhD research has lead to several peer reviewed publications of which some of them are presented in this dissertation. Based on his research a patent has been submitted, he has given 12 talks in international conferences, awarded a student price at the IRMMW-THz conference and serves regularly as a reviewer for several scientific journals.

During his studies at the University of Cyprus, Giorgos was an active member of the student association and he was elected as a member of the faculty board where he served as a student representative for a period of one year.

In his free time, he enjoys travelling, discussing about politics and of course spending time with his friends.

Invitation

to the defense of
the doctoral thesis

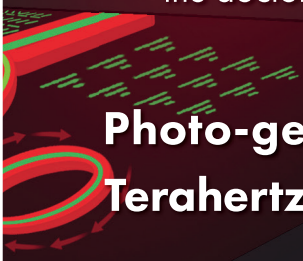

Photo-generated Terahertz devices

on Tuesday,
02 February, 2016
at 14.00

in Collegezaal 4 of the
Auditorium in the Technical
University of Eindhoven

A reception
will follow the ceremony

Giorgos Georgiou
georgiougeor@gmail.com

Paranymphs
Alessandro Antoncecchi
Nicola Gritti